



HAL
open science

Optical processes in α -ZnAl₂S₄ spinel-type single crystals doped by transition metals ions: ti, Co et V

Sergiu Anghel

► **To cite this version:**

Sergiu Anghel. Optical processes in α -ZnAl₂S₄ spinel-type single crystals doped by transition metals ions: ti, Co et V. Other [cond-mat.other]. Université Claude Bernard - Lyon I; Academia de științe a Moldovei (Chișinău, Moldavie), 2011. English. NNT: 2011LYO10224 . tel-00740578

HAL Id: tel-00740578

<https://theses.hal.science/tel-00740578>

Submitted on 10 Oct 2012

HAL is a multi-disciplinary open access archive for the deposit and dissemination of scientific research documents, whether they are published or not. The documents may come from teaching and research institutions in France or abroad, or from public or private research centers.

L'archive ouverte pluridisciplinaire **HAL**, est destinée au dépôt et à la diffusion de documents scientifiques de niveau recherche, publiés ou non, émanant des établissements d'enseignement et de recherche français ou étrangers, des laboratoires publics ou privés.

**THESE EN CO-TUTELLE DE L'UNIVERSITE DE LYON ET
DE L'ACADEMIE DES SCIENCES DE MOLDAVIE**

Délivrée par

**L'UNIVERSITE CLAUDE BERNARD LYON 1 ET
L'ACADEMIE DES SCIENCES DE MOLDAVIE**

ECOLE DOCTORALE : PHAST

DIPLOME DE DOCTORAT

(arrêté du 7 août 2006)

soutenue publiquement le 11 novembre 2011

par

M. ANGHEL Sergiu

**Optical processes in α -ZnAl₂S₄ spinel-type single crystals doped with transition
metals ions**

JURY

M. VIANA Bruno	Directeur de recherche	Rapporteur
M. BOULON Georges	Professeur	Directeur de thèse
M. GUYOT Yannick	Maitre de conférences	
M. CULIUC Leonid	Professeur	Directeur de thèse
M. SIMAȘCHEVICI Alexei	Professeur	
M. CASIAN Anatolie	Professeur	Rapporteur
M. URSACHI Veaceslav	Docteur Habilité	

UNIVERSITE CLAUDE BERNARD - LYON 1

Président de l'Université

Vice-président du Conseil Scientifique

Vice-président du Conseil d'Administration

Vice-président du Conseil des Etudes et de la Vie Universitaire

Secrétaire Général

M. le Professeur L. Collet

M. le Professeur J-F. Mornex

M. le Professeur G. Annat

M. le Professeur D. Simon

M. G. Gay

COMPOSANTES SANTE

Faculté de Médecine Lyon Est – Claude Bernard

Faculté de Médecine Lyon Sud – Charles Mérieux

UFR d'Odontologie

Institut des Sciences Pharmaceutiques et Biologiques

Institut des Sciences et Techniques de Réadaptation

Département de Biologie Humaine

Directeur : M. le Professeur J. Etienne

Directeur : M. le Professeur F-N. Gilly

Directeur : M. le Professeur D. Bourgeois

Directeur : M. le Professeur F. Locher

Directeur : M. le Professeur Y. Matillon

Directeur : M. le Professeur P. Farge

COMPOSANTES ET DEPARTEMENTS DE SCIENCES ET TECHNOLOGIE

Faculté des Sciences et Technologies

Département Biologie

Département Chimie Biochimie

Département GEP

Département Informatique

Département Mathématiques

Département Mécanique

Département Physique

Département Sciences de la Terre

UFR Sciences et Techniques des Activités Physiques et Sportives

Observatoire de Lyon

Ecole Polytechnique Universitaire de Lyon 1

Institut Universitaire de Technologie de Lyon 1

Institut de Science Financière et d'Assurance

Institut Universitaire de Formation des Maîtres

Directeur : M. le Professeur F. Gieres

Directeur : M. le Professeur C. Gautier

Directeur : Mme le Professeur H. Parrot

Directeur : M. N. Siauve

Directeur : M. le Professeur S. Akkouche

Directeur : M. le Professeur A. Goldman

Directeur : M. le Professeur H. Ben Hadid

Directeur : Mme S. Fleck

Directeur : M. le Professeur P. Hantzpergue

Directeur : M. C. Collignon

Directeur : M. B. Guiderdoni

Directeur : M. le Professeur J. Lieto

Directeur : M. le Professeur C. Coulet

Directeur : M. le Professeur J-C. Augros

Directeur : M R. Bernard

REMERCIEMENTS

Ce travail en cotutelle a été effectué dans le cadre de L'Institut de Physique Appliqué de l'Académie des Sciences (République de Moldavie) et au Laboratoire de Physico-Chimie des Matériaux Luminescents de L'Université Claude Bernard Lyon1 (France).

Mes travaux sur la thèse, déroulés pendant trois années, je les ai passés avec alternance en Moldavie et en France et ont été codirigés par les codirecteurs de thèse, M. Leonid Kulyuk et M. Georges Boulon. J'ai eu le privilège de travailler avec deux grands hommes auxquels je serais reconnaissant pour leurs qualités pendant tout ma vie; en particulièrement pour leur haut niveau professionnel, l'approche au travail, l'expérience de la vie et pour leur honnêteté personnelle. J'ai appris d'avoir une attitude professionnelle et surtout d'être homme – c'était un grand honneur de travailler sous ses directions. Merci infiniment pour leur rééducation et l'apprentissage pendant toutes ces années.

Les travaux n'auraient jamais eu un début sans la participation de M. Sushchevici qui m'a initié dans la technologie de la croissance cristalline et m'a beaucoup aidé avec la croissance des cristaux ; un grand Merci et toute ma reconnaissance. Je voudrais aussi remercier Mme. Klokishner pour son aide à l'interprétation théorique des données expérimentales et pour son soutien moral pendant la durée de la thèse. Je suis très reconnaissant à Mme. Iliasenco pour son implication à la rédaction technique du manuscrit et pour son optimisme qu'elle m'a transmis.

Je veux montrer toute ma considération à ceux qui m'ont aidé et m'ont accordé leur soutien morale ; spécialement pour mes collègues et pour tous ceux qui ont eu une contribution à la formation du chercheur Sergiu Anghel. Pour tous mes amis qui ont crû en moi.

Je suis très reconnaissant aux parents qui mon donné la possibilité d'être ici – mais considérations distinguées et tout mon respect pour vous.

Ces travaux ne seraient jamais faits sans le soutien de ma famille qui a été toujours près de moi et qui m'a encouragé pendant la durée du procès entier. Je vous remercie.

Pour vous Anna et Dana – je vous aime beaucoup !

RESUME en français

Les propriétés spectroscopiques des monocristaux de α -ZnAl₂S₄, semi-conducteurs de type spinelle avec une large bande interdite, dopées par les ions des métaux de transition sont investigués et leur interprétation est donnée. Les monocristaux, obtenus par la méthode de transport chimique en phase vapeur avec la concentration des impuretés dopantes compris entre 0.01 – 0.1% at., représentent des octaèdres homogènes optique avec des faces orientent (111). Les analyses par les rayons X ont confirmée que tous les échantillons ont cristallisés dans une structure normale de type spinelle avec la symétrie cubique Fd3m (O_h⁷). Les monocristaux de α -ZnAl₂S₄:Ti manifestent des propriétés radiatives dans le domaine spectral du proche infrarouge 0.8–1.4 μ m. Les résultats spectroscopiques obtenus dans l'intervalle des températures 10-300K (les spectres de la photoluminescence stationnaire et résolue en temps, de l'absorption et de l'excitation de la photoluminescence) sont interprétés dans les termes d'un cluster composé par un ion de Ti⁴⁺ dans une configuration octaédrique des six ions de soufre. Les bandes spectrales observées sont attribuées à des transitions électroniques survenues d'un transfère de charge ligand Ti⁴⁺ pour les sites octaédriques de titane, qui est en concordance avec la évidence expérimentale de l'absence du RPE signale des ions de Ti. Les constantes vibroniques des niveaux excités et l'hauteur de la barrière potentielle entre eux ont été calculés. La structure des spectres d'absorption et de la luminescence des monocristaux de α -ZnAl₂S₄:Co est déterminé par les transitions électroniques des ions de Co²⁺ localisés dans des sites tétraédriques. Quatre composantes spectrales radiatifs sont révélés en utilisant la spectroscopie résolue en temps sous différentes longueur d'onde d'excitation et il est montré que la photoluminescence des monocristaux de α -ZnAl₂S₄:Co est dû aux transitions électroniques entre les niveaux excités des ions de Co²⁺. Les valeurs calculées des constantes de l'interaction spin – orbite des niveaux excités indiquent une faible influence du part de champ cristallin et une forte interaction spin – orbite. L'absorption optique et la photoluminescence des monocristaux de α -ZnAl₂S₄:V sont déterminées des transitions électroniques du vanadium trivalent situé dans des sites octaédriques. L'augmentation de la température est accompagnée par l'amplification de la luminescence intégrale et l'élargissement du spectre centré à $\lambda = 1.4\mu$ m. Trois composantes spectrales radiatifs de α -ZnAl₂S₄:V révélés aux basses températures sont dû aux transitions électroniques des ions de V³⁺. D'après l'analyse comparative des propriétés spectroscopiques des monocristaux de type spinelle de α -ZnAl₂S₄ dopés par les ions des métaux de transition Ti, Co, et V, le plus favorable comme milieux actifs laser, est le composée α -ZnAl₂S₄:V³⁺, qui pourrais assurer l'émission dans le domaine des longueurs d'ondes 1.2-1.6 μ m, ce qui correspondent à la région spectrale utilisée par les systèmes des communications sur fibre optique.

TITRE en anglais “Optical processes in α -ZnAl₂S₄ spinel-type single crystals doped by transition metals ions”

RESUME en anglais : Spectroscopic properties of α -ZnAl₂S₄ spinel-type single crystals of the wide band gap semiconductor doped by the transition metals Ti, Co and V are investigated and their interpretation is presented. The crystals, grown by the chemical vapour transport method, with activator impurities concentrations 0.01 – 0.1% at., correspond to optically homogeneous octahedrons with (111) - oriented mirror-like faces. The x-ray analyses confirm that all samples crystallised into the normal spinel type structure with Fd3m (O_h⁷) cubic symmetry. It is found out that α -ZnAl₂S₄:Ti single crystals exhibit luminescence in the IR spectral range 0.8–1.4 μ m. The spectroscopic results obtained in the temperature range 10-300K (steady-state and time resolved photoluminescence, optical absorption and excitation luminescence spectra) are interpreted in terms of a cluster composed of the central Ti⁴⁺ ion in an octahedral coordination of six sulphur ions. The observed spectral bands are assigned to the electronic transitions arising from the ligand – Ti⁴⁺ charge transfer for octahedral sites of titanium that is in agreement with the experimental evidence for the absence of the EPR signal from Ti ions. The vibronic coupling constant for the excited levels and the barrier height between them are calculated. The structure of the absorption and luminescence spectra of α -ZnAl₂S₄:Co crystals is determined by the electronic transitions of Co²⁺ ions located in tetrahedral sites. Four radiative spectral components are revealed using the time-resolved spectroscopy at different excitation wavelengths and it is shown that the luminescence of α -ZnAl₂S₄:Co crystals is due to the electronic transitions between the excited levels of Co²⁺ ions. The calculated values of the spin-orbit coupling constants of the excited levels indicate a weak crystal field influence and a strong spin-orbit coupling. It is determined that the absorption and luminescent properties of α -ZnAl₂S₄:V spinel type crystals are the result of electronic transitions of trivalent vanadium ions located in octahedral sites. The rise of temperature leads to the enhancement of the integral luminescence intensity and to the broadening of the spectrum centered at $\lambda = 1.4\mu$ m. Three main spectral components of the α -ZnAl₂S₄:V IR spectra revealed at low temperatures are caused by electronic transitions of V³⁺ ions. The coexistence of a broad band with the narrow lines at low temperatures, when the thermal energy $k_B T$ is much less than the height of the potential barrier between the excited states, is explained assuming that there is a phonon assisted tunnelling between these states. On the base of the comparative analysis of spectroscopic properties of α -ZnAl₂S₄ spinel type crystals doped with transition metals Ti, Co, and V it is established that α -ZnAl₂S₄:V³⁺ compounds are the most appropriate for applications as active media for solid state IR-lasers tunable in the 1.2-1.6 μ m wavelength range, which corresponds to the spectral region used in the fibre-optics communication systems.

DISCIPLINE Physique

MOTS-CLES : optical spectroscopy, luminescent properties, spinel type crystals, transition metal ions

INTITULE ET ADRESSE DE L'U.F.R. OU DU LABORATOIRE :

LPCML - UMR CNRS 5620 – Université Claude Bernard, 10 rue Ada Byron, 69622 Villeurbanne Cedex (FRANCE)

CONTENTS

LISTE OF FIGURES.....	9
LISTE OF TABLES.....	12
LIST OF ABBREVIATIONS.....	13
INTRODUCTION.....	14
1. OPTICALLY ACTIVE TRANSITION METAL IONS IN SPINEL TYPE	
CRYSTALS.....	18
<i>1.1. Literature analysis.....</i>	<i>18</i>
1.1.1. A brief description of the literature dealing with Spinel structures.....	18
1.1.2. Titanium ions as transition metal dopant in different matrices	21
1.1.3. Cobalt ions as transition metal dopants in different matrices.....	25
1.1.4. Vanadium ions as transition metal dopants in different matrices.....	29
<i>1.2. Theory of the optically active centres with d-electronic shell.....</i>	<i>35</i>
1.2.1. Introduction: static interaction, Schrödinger equation and theory of crystalline field	35
1.2.2. The crystalline field on d^1 optical ions	38
1.2.3. Group theory and spectroscopy	43
1.2.4. Splitting of energy levels in crystal field.....	48
1.2.5. Several d electrons in crystalline field of ligands. Case of weak field.....	49
1.2.6. Strong crystalline field and low- and high-spin complexes	51
1.2.7. Arbitrary ligand fields and Tanabe–Sugano diagrams	54
1.2.8. Qualitative interpretation of vibrational broadening: the configurational coordinate diagram	55
<i>1.3 Conclusions</i>	<i>60</i>
2. CRYSTAL GROWTH, STRUCTURAL CHARACTERISATION AND	
EQUIPMENT FOR MEASUREMENT OF OPTICAL PROPERTIES.....	61
<i>2.1. Introduction.....</i>	<i>61</i>
<i>2.2. Theoretical and Experimental Aspects of the Chemical Vapour Transport (CVT) Reactions</i>	<i>62</i>
<i>2.3. Synthesis and structural characterization of $\alpha - ZnAl_2S_4$ by the CVT method..</i>	<i>66</i>

2.4. Measurements of absorption spectra.....	71
2.5. Measurements of radiative properties.....	74
2.6 Conclusions	81
3. SPECTROSCOPIC CHARACTERIZATION OF CO AND V-DOPED α-ZnAl₂S₄ SPINEL TYPE SINGLE CRYSTALS.....	82
3.1. Introduction.....	82
3.2. Spectroscopic characterization of Co -doped α -ZnAl ₂ S ₄ spinel type single crystals.....	83
3.3. Spectroscopic characterization of V-doped α -ZnAl ₂ S ₄ spinel type single crystals	90
3.4 Conclusions	103
4. SPECTROSCOPIC CHARACTERIZATION OF Ti-DOPED α-ZnAl₂S₄ SPINEL TYPE SINGLE CRYSTALS	104
4.1. Introduction.....	104
4.2. Experimental results.....	105
4.3. Theory and interpretation of the experimental data.....	112
4.4 Conclusions	120
GENERAL CONCLUSIONS.....	121
BIBLIOGRAPHY	123
PUBLICATIONS DURING THE PhD	131
CONFERENCE PARTICIPATIONS DURING THE PhD.....	131
CURRICULUM VITAE	133

LISTE OF FIGURES

- Fig.1.1 A scheme of an illustrative optical centre, AB_6 . This particular centre consists of a dopant optical ion A in an octahedral environment of B ions _____ 35
- Fig. 1.2 Five d orbitals in an octahedral field: (a) an octahedral array of negative charges approaching a metal ion; (b) – (f): The orientation of d orbitals relative to the negative charges. Notice that the lobes of the d_{z^2} and the $d_{x^2-y^2}$ orbitals (b) and (c) point toward the charges, whereas the lobes of the d_{xy} , d_{yz} and d_{xz} orbitals; _____ 39
- Fig. 1.3 Destabilization E_0 and splitting Δ of the atomic D term in the field of six ligands in an octahedral complex: _____ 40
- Fig. 1.4 The arrangement of B ligand ions (black dots) around central ion A (located in the cube centre, but not displayed in the figure): (a) octahedral, (b) tetrahedral, and (c) cubic. 41
- Fig. 1.5 Splitting of D term in cubic (a), tetrahedral (b), and octahedral (c) fields of the ligands [72]. _____ 42
- Fig. 1.6 Splitting of d orbital energy levels in ligand fields of different symmetries[72]. ____ 42
- Fig. 1.7 Effect of a 90° rotation around an axis of the AB_6 centre. After the transformation the coordinates (x, y, z) became (y, -x, z) _____ 44
- Fig. 1.8 The effect on p orbitals of a $C_4(001)$ operation (clockwise sense). _____ 45
- Fig. 1.9 Splitting of the terms of the electronic d^2 configuration in octahedral ligand fields in the weak-field limit [72]: (a) d-electron energy level; (b) interelectron interaction (spherical averaged part); (c) interelectron interaction—formation of atomic terms ; (d) ligand field destabilization; (e) ligand field splitting as a function of Δ . _____ 50
- Fig. 1.10 Splitting of the terms of the d^2 configuration in strong fields of octahedral symmetry [72]: (a) d-electron energy level; (b) ligand field destabilization; (c) ligand field splitting as a function of Δ ; (d) electron interaction destabilization; (e) electron interaction splitting. _ 52
- Fig. 1.11 Correlation of energy terms of electronic d^2 configuration in weak, strong, and intermediate ligand fields of octahedral symmetry[71]: (a) d levels; (b) weak field; (c) intermediary field (d) strong field and weak interelectron repulsion (e) strong field. _____ 54
- Fig. 1.12 Configurational coordinate diagram for the AB_6 centre oscillating as a breathing mode [72]. Broken curves are parabolas within the approximation of the harmonic oscillator. Horizontal full lines are phonon states. _____ 57
- Fig. 1.13 The shape of the $|\chi_0(Q)|^2$ and $|\chi_{20}(Q)|^2$ functions for a quantum harmonic oscillator [72]. _____ 58
- Fig. 1.14 A configurational coordinate diagram that describes the transitions between two electronic states [72]. Harmonic oscillators at the same frequency Ω are assumed for both states. The absorption and emission band profiles are sketched based on the $0 \rightarrow m$

(absorption) and $n \leftarrow 0$ (emission) relative transition probabilities (see the text). For simplicity, the minima of these parabolas, Q_1 and Q_2 , are not represented.	59
Fig. 2.1 Sulphur structure with eight face-centered cubic (dense-packed) sublattices per elementary cell	66
Fig. 2.2 Scheme of a dual-zone tube furnace. Inside the temperature is adjusted by the proportional–integral–derivative controller with the aid of thermocouples 1 and 2.	68
Fig. 2.3 Temperature distribution diagram in the tube furnace for growing the $ZnAl_2S_4$ spinel type single crystals	69
Fig. 2.4 α - $ZnAl_2S_4$ spinel type single crystals doped by vanadium – 0.05% at., grown by the chemical vapour transport method.	69
Fig. 2.5 XRD patterns of α - $ZnAl_2S_4$ spinel type single crystals	71
Fig. 2.6 Schematic diagrams of (a) a single-beam spectrophotometer and (b) a double beam spectrophotometer.	72
Fig. 2.7 Experimental set-up for spectroscopic investigations.	75
Fig. 2.8 Schematic temporal decay of luminescence, showing a gate of width Δt at delay time t_i .	78
Fig. 3.1 Optical absorption spectra for undoped and Co-doped α - $ZnAl_2S_4$ single crystals. Energy level splitting for Co ions in T_d symmetry and transitions corresponding to the absorption bands doped material.	83
Fig. 3.2 E_{A_2} absorption component for Co-doped α - $ZnAl_2S_4$ single crystals and the transitions from the ground state $^4A_2(^4F)$ to the three sublevels of the excited $^4T_1(^4P)$ level splitted by spin-orbit coupling	84
Fig. 3.3 E_{A_1} IR absorption component for Co-doped α - $ZnAl_2S_4$ single crystals and transitions from the ground state $^4A_2(^4F)$ to the four sublevels of the $^4T_1(^4F)$ excited level.	85
Fig. 3.4 Tanabe – Sugano diagram for Co^{2+} ions in tetrahedral coordination taken from [32]	87
Fig. 3.5 Steady-state luminescence spectra of α - $ZnAl_2S_4:Co^{2+}$ at low temperatures.	88
Fig. 3.6 Time-resolved luminescence spectra of Co-doped $ZnAl_2S_4$ at low temperature:	89
Fig. 3.7 Optical absorption spectra for undoped and V-doped α - $ZnAl_2S_4$ single crystals;	90
Fig. 3.8 Steady-state PL spectra of α - $ZnAl_2S_4:V^{3+}$ at different temperatures	91
Fig. 3.9 Temperature dependence of the integral PL intensity of α - $ZnAl_2S_4:V$.	92
ig. 3.10 Low temperature PL spectra at three excitation wavelengths: 410nm, 532nm and 633 nm.	93
Fig. 3.11 a) Tanabe-Sugano diagram for d^2 octahedral configuration;	95

Fig. 3.12 Configuration coordinates diagram for the 2E and 4T_2 excited states for Cr^{3+} GSGG [91]	97
Fig. 3.13 Life-times of E_{PL2a} spectral component at two temperatures	98
Fig. 3.14 Life-times of E_{PL2a} spectral component under different excitations at room temperature	99
Fig. 3.15 Lifetimes of the E_{PL2a} spectral component under $\lambda_{ex3}=532nm$ at different temperature (star point). The solid line represents the least square fits to the (3.10) equation.	101
Fig. 3.16 Temperature dependence of the integral PL intensity of $\alpha-ZnAl_2S_4:V$.	102
Fig. 4.1 Absorption spectrum at room temperature for three thickness of $\alpha-ZnAl_2S_4:Ti - 0.1$ at.% single crystal	106
Fig. 4.2 Absorption spectrum at room temperature of $\alpha-ZnAl_2S_4:Ti - 0.1$ at.% single crystal for $d1$ thickness.	107
Fig. 4.3 The absorption coefficient spectrum of $\alpha-ZnAl_2S_4:Ti - 0.1$ at.% single crystal	107
Fig. 4.4 Emission spectra under "green" excitation at different temperatures.	108
Fig. 4.5 PL spectra under "green" and "red" excitations at low and room temperatures.	109
Fig. 4.6 Time resolved PL spectra under "green" pulsed excitation	109
Fig. 4.7 Luminescence kinetics under $\lambda_{ex}= 532$ nm and $\lambda_{ex}= 633$ nm excitation at different temperatures.	110
Fig. 4.8 Excitation spectra for $\alpha-ZnAl_2S_4:Ti - 0.1$ at.% single crystal at two temperatures	111
Fig. 4.9 Absorption and PLE spectra of $\alpha-ZnAl_2S_4:Ti$ single crystal.	111
Fig. 4.10 A schematic energy-level diagram for an octahedral AB_6 centre in the frame of MO theory. This diagram is constructed from the atomic levels of A and B[95]	113
Fig. 4.11 Single configuration-coordinate diagram for TiS_6 complex in $\alpha-ZnAl_2S_4$.	116
Fig. 4.12 Time-resolved luminescence spectra of $ZnAl_2S_4:Co^{2+}$ and $ZnAl_2S_4:Ti^{4+}$ under "green" excitation at low temperature	118

LISTE OF TABLES

<i>Table 1.1 A character table for the O_h point group</i>	47
<i>Table 1.2 Correlations of irreducible representations of O_h and D_{4h} symmetry groups with their subgroups indicating the corresponding symmetry transformations and splitting.</i>	50
<i>Table 1.3 Electronic configuration and ground-state terms of octahedral and tetrahedral complexes in the case of strong ligand fields</i>	53
<i>Table 1.4 Some numerical values for the Racah parameters B and C (in cm^{-1}) and $\gamma = C/B$ for transition metal ions M^{2+} and M^{3+}.</i>	55
<i>Table 2.1 X-ray diffraction data of the undoped α - ZnAl_2S_4</i>	70
<i>Table 3.1 Energies of the spectral components of the absorption and emission spectra of Co^{2+} ions in α-ZnAl_2S_4 spinel and their assignments</i>	86

LIST OF ABBREVIATIONS

<i>TM</i>	Transition metal
<i>EPR</i>	Electronic paramagnetic resonance
<i>IR</i>	Infrared
<i>T_d</i>	Tetrahedral symmetry
<i>O_h</i>	Octahedral symmetry
<i>UV</i>	Ultraviolet
<i>PL</i>	Photoluminescence
<i>PLE</i>	Excitation of the photoluminescence
<i>CI</i>	Central ion
<i>A</i>	Dopant ion
<i>B</i>	Lattice ion
<i>CFT</i>	Crystal field theory
<i>MOT</i>	Molecular orbital theory
<i>CF</i>	Crystal field
<i>FI</i>	Free ion
<i>H_{SO}</i>	Hamiltonian of the spin-orbit interaction
<i>H_{ee}</i>	Hamiltonian of the electron - electron interaction
<i>Dq</i>	Intensity of the crystalline field
<i>g</i>	Group order
<i>R</i>	Symmetry operation
<i>M</i>	Matrix
<i>Γ</i>	Components of the matrix
<i>χ</i>	Character of the matrix
<i>C, B</i>	Racah parameters
<i>Q</i>	Configurational coordinate
<i>FWHM</i>	Full width at half maximum
<i>m</i>	Amount of material transported per unit time
<i>L</i>	“Conductance” of the system
<i>ΔH</i>	Heat of the reaction
<i>S</i>	Entropy
<i>ΔG</i>	Change in free energy
<i>m</i>	Amount of transported material
<i>c_T</i>	Concentration of the transporter
<i>PID</i>	Proportional-integral -derivate
<i>VIS</i>	Visible
<i>TRL</i>	Time-resolved luminescence
<i>C_d</i>	Degeneracy of the energy level

INTRODUCTION

Apart from the use of lodestone or magnetite by the ancient navigators, it is almost certain, in the opinion of many specialists, that the earliest use of spinel materials was for decorative purposes. Many of the oxide spinels, especially MgAl_2O_4 and ZnAl_2O_4 , occur naturally as transparent materials with high refractive index (approximately 1.7) and with a hardness, which is exceeded only by diamond and corundum. They are in fact natural gemstones and were used as such. Spinel is considered to be a good candidate for the “History’s Most Under-Appreciated Gem”. Some ancient mines that supplied gems for royal courts from Rome to China produced spinels, but they were usually confused with better-known stones like ruby and sapphire. Some of the world’s most illustrious “rubies” are actually spinels.

Oxide spinels are natural industrial refractory materials because of their cheapness, cubic structure (i.e. uniform thermal expansion) and high melting points. Indeed, their commercial importance has probably been predominantly in this field during the past 100 years or so, although current developments suggest that applications in the electronics industry are now more important. Chrome-magnesite bricks for example, made from a mixture of chrome ore and MgO , have been the essential lining material for much of the structure of industrial furnaces like the open hearth type, because of their good strength at high temperatures and resistance to wear by metalliferous slag. The latter valuable property arises from the low solubility of chromite spinels in liquid silicates. Many of the transition oxide spinels are important chemical catalysts, a fact which curiously has been a nuisance from the industrial ceramic point of view in limiting the ultimate practical temperatures for chrome-magnesite brick in certain applications (because of a catalytic reaction with magnetite). On the other hand, NiAl_2O_4 spinel proved useful as a catalyst in the old-fashioned production of town gas.

The most remarkable growth in commercial exploitation of spinel materials has undoubtedly taken place in the field of electronics. In this industry, the increasing importance of eddy current losses incurred in transformer and load coils of telecommunication equipment, as higher and higher frequencies were utilized, had created the need for materials which were simultaneously both ferromagnetic and electrically insulating. The importance of the spinel ferrites in this context was recognized very early and high-resistivity materials soon became available. The first such materials were not ideal because they suffered quite badly from magnetic after effects such as deterioration in initial permeability and dielectric losses. But gradual improvements were nevertheless good enough to result in the widespread use of the spinel ferrites in radio and television, while magnetite and $\gamma\text{-Fe}_2\text{O}_3$ became the staple

materials used in the manufacture of magnetic recording tape. At about the same time, spinels also assumed importance for electronic computers following the discovery that some polycrystalline ferrites exhibit a rectangular hysteresis loop and consequently that they could be used as memory elements.

The prevailing trend in electronics, which seems likely to continue for some years yet, has been towards increasing miniaturization. The spinel ferrites have played an important part through their effectiveness for concentrating magnetic flux, as this provided the opportunity to reduce the size of inductive loads and filters. Further reduction in size now, which leads to considerable commercial advantage in both computer and telecommunications applications, can only be achieved by exploiting the precision available in single crystal technology, where whole circuits are constructed either from thin films grown on insulating substrates or within a monolithic single crystal chip. In this case, the active constituent of such circuitry is chiefly semiconducting silicon so that the requirements of a good substrate material may be very simply stated: a chemically inert crystal, which is electrically insulating with a cubic crystal structure compatible with the epitaxial growth of silicon. Ideally, this substrate should have good thermal conductivity for thermal stability and if possible, have transparency over a wide range of optical wavelengths so that there should be no constraints to the use of optical switching or photoconductive effects. Up to the present time, MgAl_2O_4 spinel has been by far the most successful substrate material. It is transparent over the whole of the visible spectrum and, being cubic, is optically isotropic as well. It is relatively chemically inert, and so compatible with the silicon lattice, thus silicon may be grown with equal facility in [100], [110] or [111] - orientation simply by choosing the orientation of the spinel.

In a different direction, and in contrast to the wide range of applications which have developed for the oxide spinels, much less has been done to utilize the properties of the analogous sulphide and selenide materials. This was partly due to the greater technical problems associated with their preparation. It seems now that this situation may change dramatically over the next few years following a series of scientific investigations which have uncovered an almost unique range of physical behaviour.

A variety of interesting optical properties and applications of the oxide and sulphide spinels depend on the presence of *optically active centres*. These centres consist of dopant ions, usually transition or rare earth metal ions that are intentionally introduced into the crystal during the growth process. The localized centres provide energy levels within the energy gap of the material, so that they can give rise to the appearance of optical transitions at frequencies lower than that of the fundamental absorption edge. The optical properties of the oxide spinels doped by transition or rare earth metal ions have been mainly investigated due

to their advantages over ruby in that its cubic crystal structure provided optical isotropy (see de literature analyses below). Unlike the crystals containing trivalent chromium, systems based on other transition metal ions and/or other oxidation states are not easy to deal with; ions like Ti, V, and Co have a strong tendency to form mixed valence systems. It is almost certain that at least some of the theoretical difficulties which have arisen are connected with assumptions about the crystal structure of the spinels, described by general formula $A^{2+}B_2^{3+}X_4^{2-}$. Due to the presence of the two possible sites for the cations, the octahedral and tetrahedral sites for A and B cations respectively, it turns out that a wide range of divalent ions may be substituted for A^{2+} , and almost any trivalent ions for B_2^{3+} . One of the problems associated with crystal structure determination concerns the distribution of metal ions between the interstitial A and B sites. Although an enormous amount of research has been devoted in the last decade to the study of the magnetic properties of sulphide spinels so that it is really known quite a lot now about their properties, it is surprising to find that there are practically no papers (to the best of the knowledge of the author of the present thesis) investigating the spectroscopic properties of sulphide spinels, in particular α - $ZnAl_2S_4$ single crystals, that were the main object in the present thesis. In spite of a few spectroscopic studies of the optical properties of the undoped and chromium doped α - $ZnAl_2S_4$, still the understanding of many optical phenomena in α - $ZnAl_2S_4$ doped by transition metal ions is rather poor. On the other hand, the crystal field strength of the sulphide spinels, according to the spectrochemical series, is weaker compared to that of the oxide spinels, which should lead to the shift of the radiative spectra to the near infrared, a region of interest that is used in the fibre-optics communication systems.

The present thesis, consisting of *Introduction*, four *Chapters*, *Conclusions* and *References*, is focused on the study and interpretation of the spectroscopic properties of α - $ZnAl_2S_4$ spinel type single crystals doped by three transition metal ions: Titanium (Ti), Vanadium (V), and Cobalt (Co). In the first part of *Chapter I* an overview is presented of the most relevant publications describing the studies of the growth techniques and spectroscopic properties of different oxide spinels and sulphide structures. In the second part of the same Chapter, an account is given of the basic concepts of the crystal field theory of the activator in crystals. In *Chapter II* the techniques and methods used for the Ti, Co and V doped α - $ZnAl_2S_4$ single crystals growth are described. In addition, there is presentation of the obtained crystals and their structural characterisation by x-ray diffraction, as well as a brief description of each technique used for the measurements of spectroscopic properties of the samples. *Chapter III* expounds the ways to and the outcomes of the investigations of spectroscopic properties of Ti-doped α - $ZnAl_2S_4$, in particular, of the absorption, steady-state and time-resolved

photoluminescence and excitation spectra. This Chapter also examines the issue of the charge transfer process between the sulphur ligand and Ti^{4+} ions localised in the octahedral sites and the interpretation of the obtain spectroscopic results in terms of a cluster composed of the central Ti^{4+} ion in a octahedral coordination of six sulphur ions. *Chapter IV* brings into discussion the analysis of optical properties of the same host material but doped with Co and V. The difference from the data in Chapter III is that here the doping ions have the electrons in the *d*-shell of their electron configuration, which allows using of the crystal field theory and Tanabe – Sugano diagram for interpretation of their spectroscopic properties.

Next come *Conclusions* inferred from the research and experiments performed.

The literary information is listed in *Bibliography*.

1. OPTICALLY ACTIVE TRANSITION METAL IONS IN SPINEL TYPE CRYSTALS.

1.1. Literature analysis

1.1.1. A brief description of the literature dealing with Spinel structures

The mineral MgAl_2O_4 , known as spinel, is not the only naturally occurring member of the family. There are at least a dozen commercially important metalliferous ores and this gives us an immediate indication of one of the important attributes of these compounds, namely the facility with which they can be formed. This means that the spinels are one of the most extensive series of related chemical compounds known: indeed, there are more than 200 of them altogether. This thesis will give just a little more limelight to a remarkable group of compounds with a quite astonishing record of usefulness.

Fe-, Cr- and Al-spinels were synthesized and their unit cell sizes determined by means of x-rays[1]. A correlation can be made between ionic radii of cations and unit cell dimensions provided the effect of covalent forces in the lattice is taken into account. A shrinkage of 0.01 \AA in the unit cell size per 0.01 \AA decrease in the ionic radius of the divalent cations was determined when spinels with the same cation arrangement in the same group were compared. A shrinkage of 0.027 \AA in the unit cell size per 0.01 \AA decrease in the ionic radius of the trivalent cations was determined in spinels having the same divalent cation and cation arrangement when the trivalent cations form the same type of bonds. The divalent transition element ions are Fe^{2+} , Co^{2+} and Ni^{2+} ; the B-Sub-group element ions are Cd^{2+} and Zn^{2+} ; Fe^{3+} in tetrahedral co-ordination.

A new technique that has been useful in growing single crystals of a number of the chalcogenide spinels is described in [2]. Crystals $A\text{Cr}_2X_4$, where $A = \text{Zn}$ or Cd , $X = \text{S}$ or Se , are grown by reacting compound AX and CrCl_3 in a sealed and evacuated silica vial. The authors of that work were the first to grow antiferromagnetic ZnCr_2Se_4 and ZnCr_2S_4 crystals. The compounds, which are separated to suppress an interface reaction, are heated to $800^\circ\text{--}1000^\circ\text{C}$ maintaining about a 50°C gradient along the vial. Spinel crystals are formed at the low-temperature end of the vial embedded in a liquid phase which consists mostly of $A\text{Cl}_2$. The growth mode is mainly octahedral with well-developed (111) faces, although the larger crystals tend to be flat, truncated along [100] and [110]. Microscopic examination shows the crystals to be sound, containing few internal voids. The complex growth mechanism is discussed in general terms involving an initial vapour transport of the system components and

the resultant liquid-vapour environment required for crystal formation. The effect of some substitutional (*A*-site) doping experiments in CdCr₂S₄ crystals is reviewed.

The crystal growth and crystallographic and chemical characterization of spinels of the type ACr₂S₄, where A = Cu, Zn, Cd, Hg, Mn, Fe, or Co and ACr₂Se₄ where A = Cu, Zn, Cd, or Hg which exhibit interesting magnetic (ferro-, ferri-, antiferro-), electrical (metallic, semiconducting, insulating), and optical properties have been studied in[3].

The paper[4] presents the results of a study of the thermal stability and thermochemical, thermodynamic, and crystallochemical properties of the chalcocromites MeCr₂X₄ (*Me* = Cd, Co, Zn, Fe, Cu; *X* = S, Se, Te), thiocobaltites MeCo₂S₄ (*Me* = Cu, Co), thiorhodites Me_xRh_{3-x}S₄ (*Me* = Cu, Co, Fe), thioaluminates MeAl₂S₄ (*Me* = Zn, Cr), and solid solutions based on these. An attempt is made to show how much the investigated properties influence the magnetic and electrical properties of the chalcogenide spinels.

Phase relationships between 720 and 1110°C were determined in [5] including the system ZnS–Al₂S₃: (a) the location of a eutectoid at 740°C and 15 mole% Al₂S₃, (b) the solubility limits of Al₂S₃ in the zinc blend and wurtzite forms of ZnS and the spinel and wurtzite forms of ZnAl₂S₄, and (c) the probable relationships at the liquidus. The system ZnAl₂S₄–ZnIn₂S₄ at 800 to 1050°C was found to be a simple eutectic type with the following features: (a) a eutectic point at 930–950°C and approximately 20 mole% ZnIn₂S₄, (b) a large region of ZnIn₂S₄ solid solutions, and (c) little solubility of ZnIn₂S₄ in ZnAl₂S₄.

Systematic trends in the geometry of 149 oxide and 80 sulphide binary and ternary spinels have been examined from the standpoint of ionic radius and electronegativity in [6]. The mean ionic radii of the octahedral and tetrahedral cations, taken together, account for 96.9 and 90.5% of the variation in the unit cell parameter *a* in the oxides and sulphides, respectively, with the octahedral cation exerting by far the dominant influence in sulphides. The mean electronegativity of the octahedral cation exerts an additional, but small, influence on the cell edge of the sulphides. The equation $a = (8/3\sqrt{d})d_{\text{tet}} + (8/3)d_{\text{oct}}$, where *d*_{tet} and *d*_{oct} are the tetrahedral and octahedral bond lengths obtained from the sum of the ionic radii, accounts for 96.7 and 83.2% of the variation in *a* in the oxides and sulphides, respectively, again testifying to the applicability of the hard-sphere ionic model in the case of the spinel structure. Comparison of observed and calculated *u* values for 94 spinels indicates that up to 40% of the experimentally measured anion coordinates may be significantly in error. In addition to these compounds, *u* values are given for 52 spinels for which no data have been previously determined. Diagrams are presented for the rapid interpretation of the internal consistency of the published data and the prediction of the structural parameters of hypothetical or partially studied spinels.

The crystal structure of ZnAl_2S_4 has been refined using three-dimensional x-ray diffraction data in [7]. The lattice constant of single crystals obtained by chemical transport reaction at 740°C is $1000.9(1)$ pm. The authors have carried out refinements in space groups $\text{Fd}\bar{3}\text{m}$ and $\text{F}\bar{4}3\text{m}$, due to the presence of a number of $h\ k\ 0$ reflections with $h + k = 4n + 2$, which are forbidden for the space group $\text{Fd}\bar{3}\text{m}$ usually assigned to the spinel structure. The results show that there is no reason to reject the space group $\text{Fd}\bar{3}\text{m}$. The forbidden reflections can be satisfactorily explained by double diffraction. The positional parameter of the sulphur atom has been determined to $x = 0.38463(2)$. The cation distribution corresponds to the normal spinel structure, the inversion parameter i (fraction of tetrahedral sites occupied by aluminium) is smaller than 0.02.

A chapter in [8] is focused on spinels, influence of various cations on their properties, namely the distribution of cations between the tetrahedral and octahedral position, a macroscopic Jahn-Teller distortion, formation of clusters and ordering of cations. Destabilization of the spinel structure due to the deviations from the ideal stoichiometry and the influence of the cation properties is discussed as well.

The structure and cation distribution of different types of the zinc aluminium sulphide ZnAl_2S_4 , are investigated in [9]. Samples prepared at $800\text{--}900^\circ\text{C}$ with the atomic composition $\text{Al}/\text{Zn} = 2$ or 3 contained α , β and W phases, as identified by x-ray diffraction. Pure yellow α phase material was sometimes formed or could be hand-picked from some samples. Samples prepared at 1070°C with $\text{Al}/\text{Zn} = 1.1$ contained only the β phase. Crystals of a phase designated γ' were grown by iodine transport of α zinc aluminium sulphide powder ($\text{Al}/\text{Zn} = 3$) from 800 to 740°C . The infrared transmittance of a stack of γ' crystals (<1 mm thick) was $66\text{--}68^\circ$ from 2.5 to $9\mu\text{m}$, at which wavelength the transmittance began to decrease. A characteristic EPR spectrum of a Mn^{2+} impurity at tetrahedral sites of α zinc aluminium sulphide [$g = 2.002$, $A = -64.6 \times 10^{-4}\text{cm}^{-1}$, $|D| = 50 (\pm 20) \times 10^{-4}\text{cm}^{-1}$] was identified. A second Mn^{2+} spectrum was characteristic of samples that were mixtures of α , W and (sometimes) β phases. A symmetric 21 line EPR signal at $g = 1.991$ with $A = 2.86 \times 10^{-4}\text{cm}^{-1}$ was attributed to an extra electron trapped at a site containing a sulphide ion surrounded by four aluminium ions in W-phase zinc aluminium sulphide.

Infrared reflectivity spectra and Raman scattering of ZnAl_2S_4 and CdIn_2S_4 crystals were investigated in [10]. In this work, IR reflectivity spectra in the range from 50 to 4000cm^{-1} and the Raman scattering in ZnAl_2S_4 and CdIn_2S_4 crystals were studied. The calculations of the reflectivity spectra were performed, and phonon parameters, dielectric constants and the ion charges of Zn, Cd, In and S in ZnAl_2S_4 and CdIn_2S_4 compounds were determined. Effective charges for the Zn, Cd, In and S ions of these materials were also defined.

1.1.2. Titanium ions as transition metal dopant in different matrices

The problem of discrete levels in resonance with a continuum has received a good deal of attention in solid state physics. Especially, there has been a considerable interest in transition metals ions doped crystals as the active media for solid-state lasers. A well known example is Ti-sapphire ($\text{Al}_2\text{O}_3:\text{Ti}$), firstly investigated by Moulton in [11], where the author showed that the $\text{Ti}:\text{Al}_2\text{O}_3$ laser is characterized by a simple energy-level structure, a broad tuning range, and a relatively large gain cross section. Laser operation spanning the entire expected gain linewidth and efficient, nearly quantum-limited, conversion of the pump energy have been observed. Such behaviour is possible because the simple energy-level structure of the Ti^{3+} ion does not permit excited-state absorption of either the pump or the $\text{Ti}:\text{Al}_2\text{O}_3$ laser radiation, provided that any charge-transfer transitions are sufficiently high in energy; this condition appears to be met in $\text{Ti}:\text{Al}_2\text{O}_3$. Certain difficulties connected with the simultaneous presence in the host of Ti^{3+} and Ti^{4+} ions are faced. In [12] it was revealed that the absorption spectrum of $\text{Ti}^{3+}:\text{Al}_2\text{O}_3$ crystals consists of the main blue-green absorption band and a weak infrared band. This infrared absorption decreases in intensity on annealing in a reducing atmosphere. Combined optical and EPR studies allowed to assume that the center associated with the red band is a cluster involving Ti^{3+} and Ti^{4+} with a neighbouring, charge compensating Al^{3+} vacancy. Two types of Ti^{4+} in Al_2O_3 (locally and non-locally charge compensated) were optically identified in [13]. The photoionization of Ti^{3+} in sapphire $\alpha\text{-Al}_2\text{O}_3$ was studied by means of one-step and two-step photoconductivity measurements. An absorption band of Ti^{3+} at 2700\AA was shown to be due to a Ti^{3+} localized exciton. One-photon photoconductivity began at the high-energy side of this band and thus the photoionization threshold could be located at $4.71\pm 0.07\text{eV}$. The two-photon photoconductivity spectrum was nearly coincident with the excited state absorption and was shifted 0.6eV to higher energy than the one-photon spectrum, due to the effect of the Jahn-Teller distortion of the 2E initial state. The origin of the transition due to the valence band electron capture by Ti^{4+} was located at 4.17eV . These electron and hole ionization energies were compared to values obtained by the Born-Haber cycle calculations. Their sum is 0.5eV less than the band gap of Al_2O_3 . The lifetimes of the charge-transfer emission as a function of temperature were well explained by a three-level scheme with a lower triplet and a higher singlet excited states.

A similar problem to that observed in $\text{Ti}^{3+}:\text{Al}_2\text{O}_3$ has been reported for $\text{Ti}^{3+}:\text{YAlO}_3$ for which spectroscopic properties and excited-state absorption (ESA) of Ti^{3+} ions are investigated in detail in [14]. A broad absorption is observed around 950 nm in addition to the normal visible absorption bands at 434 and 492 nm . The fluorescence band is centred at 623 nm with a room temperature lifetime of $11.4\mu\text{s}$ and the quantum efficiency nearly one. The

laser action could not be detected because of strong excited-state absorption into a charge transfer band located 45500cm^{-1} above the Ti^{3+} ground state. At the Ar-laser pump wavelength the ESA cross-section was determined to be $\sigma_e=1\times 10^{-18}\text{cm}^2$. This value is by the factor of 44 higher than the ground-state absorption cross-section. Consequently, the pumping efficiency is decreased by one or two orders of magnitude.

In the vein to obtain room-temperature IR sources of radiation the spectral properties of titanium doped chalcogenides, along with titanium doped oxide compounds, have been also intensively studied by many authors. In earlier publications absorption, photoconductivity and the Hall measurements were reported on CdS [15-18] and CdSe [17, 19-20]. In particular, strong Ti^{2+} absorption bands determine the energies of the two prominent transitions from ${}^3\text{A}_2({}^3\text{F})$ to ${}^3\text{T}_1({}^3\text{F})$ and ${}^3\text{T}_1({}^3\text{P})$ levels. A very weak absorption is detected also in both materials with maxima at about 3100cm^{-1} in CdSe [20] and 3320cm^{-1} in CdS [16]. This absorption has been assigned to the transition ${}^3\text{A}_2({}^3\text{F})\text{--}{}^3\text{T}_2({}^3\text{F})$ which is forbidden in T_d symmetry. The absorption spectrum of Ti^{2+} centres in CdS between 0.3 and 1.5eV is measured in the temperature range 10 to 295K[16]. The spectrum is explained on the basis of the crystal-field theory. A detailed analysis of the temperature dependence of the ${}^3\text{A}_2, \rightarrow {}^3\text{T}_1({}^3\text{F})$ band shows that the triplet structure of this band is due to strong interaction with τ_2 type vibrational modes of phonon energy 3.3meV. The authors in [17] study the electron-phonon interaction at Ti^{2+} centres in CdS and CdSe by analyzing the temperature dependence of the ${}^3\text{A}_2 \rightarrow {}^3\text{T}_1({}^3\text{F})$ and ${}^3\text{A}_2 \rightarrow {}^3\text{T}_1({}^3\text{P})$ absorption bands of these systems. They the triplet structure in the ${}^3\text{T}_1({}^3\text{F})$ band due to coupling with τ_2 -type vibrations is found for CdSe, just as had been earlier reported for CdS, while the ${}^3\text{T}_1({}^3\text{P})$ bands did not exhibit a pronounced structure for both host substances. This behaviour was discussed on the basis of a cluster model involving coupling only to the displacements of the impurity and ligand ions. A point-charge estimate showed that for both ${}^3\text{T}_1({}^3\text{F})$ and ${}^3\text{T}_1({}^3\text{P})$ excited states the overall coupling to τ_2 -type vibrations should be rather strong. The interpretation of different shapes of the two bands was the following: ${}^3\text{T}_1({}^3\text{F})$ states are especially sensitive to a group of τ_2 vibrations having very low frequency, whereas the ${}^3\text{T}_1({}^3\text{P})$ states are mainly coupled to higher frequency τ_2 vibrations. In [21-22] an EPR investigation of the hyperfine interactions with ligand nuclei of the Ti^{2+} centre in single crystals of hexagonal CdS and CdSe on sites with trigonal C_{3v} symmetry has been undertaken. The experimental data obtained in [21] show that under irradiation of CdS: Ti^{2+} with light in the spectral region 400 to 800 nm no change of the EPR spectra could be observed. An irradiation with light of longer wavelengths results in a strong quenching and a line broadening of the EPR signal. The maximum quenching of the EPR spectrum was found to correspond to the maximum of photoconductivity. The observed effect

was explained by the depopulation of the 3A_2 term through the transitions to the excited levels that are in the conduction band of CdS. In [23], the ground states of Ti^{2+} and Ti^{3+} were detected by the EPR, indicating a substitutional incorporation of Ti ions into Cd-sites in CdS, CdSe and Cd(S,Se) crystals. For the first time in [23], the Jahn-Teller ion Ti^{3+} was observed by its $^2T_2 \rightarrow ^2E$ transition in photoluminescence. Optical and paramagnetic properties of titanium centres in ZnS were examined in [24]. In that paper it was shown that the Ti^{2+} ion on a cubic site presented an isotropic EPR signal with $g=1.928$ observable up to 80 K. Signals of Ti^{2+} ions on axial sites were detected in the same temperature range. In that paper it was also demonstrated that in emission the Ti^{2+} ion exhibited the $^3T_2(^3F) \rightarrow ^3A_2(^3F)$ transition, structured by no-phonon lines of centres in various environments. The prominent line at 3613 cm^{-1} in the emission spectrum was assigned to the centre with the T_d symmetry, while the lines at 3636 , 3634 and 3632 cm^{-1} were assumed to originate from the impurity centres in various trigonally distorted environments as corroborated by the EPR data.

In [25] there are several crystalline hosts where titanium ions manifest broad band luminescence in the near IR and visible regions. Single crystals of GdScAl garnet were successfully doped with Ti^{3+} ions using a reducing atmosphere. Two broadband absorption peaks, typical of the Ti^{3+} Jahn–Teller splitting, were observed at 520 and 620 nm. Fluorescence was observed in the 720–1050 nm region peaked at 840 nm. Fluorescence lifetime was $5.5 \mu\text{s}$ at 12–50 K but decreased rapidly at higher temperatures. CaGdAlO₄ crystals doped with Ti ions were grown using the Czochralski technique in a reducing atmosphere in order to convert the valence of Ti to trivalence. The fluorescence of the $^2E^2T_2$ transition of Ti^{3+} in the crystals shows a broad band with a peak at 535 nm excited with the light of 410 nm in the optical absorption band at room temperature because of a strong electron-phonon coupling of the 2E excited state. The intensity of Ti^{3+} fluorescence is influenced by O^{2-} vacancies at the ligands of the Ti^{3+} octahedra along the c axis, which are easily produced in a reducing atmosphere. The x-ray crystal analyses and the polarization of the optical absorption and fluorescence spectra deduce the energy levels and wave functions of the ground and excited states of Ti^{3+} in CaGdAlO₄. The peak energy of the fluorescence band shifts to a higher energy when increasing the excitation energy in the absorption band. In [26] the linear dependence of the fluorescence-peak energy on the excitation energy shows that the fluorescence is inhomogeneously broadened by a random distribution of Ca^{2+} and Gd^{3+} ions in the disordered lattice.

The spectroscopic properties of Ti impurity in the spinel host crystal MgAl₂O₄ were investigated in [27–29], and blue emission with strong intensity was detected. Meanwhile, the interpretation of spectroscopic properties of different oxides doped by titanium is not

straightforward. The photoluminescence (excitation, emission, and fluorescence decay time) spectra of spinel (Ti:MgAl₂O₄) excited by pulsed Nd:YAG and dye lasers were systematically investigated in [27]. Excitation into the $T_{2g} \rightarrow E_g$ crystal-field transition of Ti³⁺ produced a broad infrared emission band at 805 nm which could, in principle, be used for tunable laser applications. Two different Ti³⁺ centres with lifetimes of 4.2 μs and 41 μs contributed to that emission. At the same time this IR band was also observed under high-intensity excitation in the ultraviolet region (266 nm) via a two-photon process.

The spectroscopic properties of the same oxide spinel, successfully grown by the micro-pulling-down method, were investigated in view of their potential use as a short-wavelength tunable solid-state laser [29]. Strong blue emission was observed from Ti-doped MgAl₂O₄. The optimum conditions to obtain the strongest emission were studied by changing the doping concentration. The broad emission bands around 455 nm for Ti (decay time of 5.7 μs) were obtained by pumping in the UV region at 266 nm. The presence of this band originated from Ti⁴⁺ occupying the Al³⁺ site in the spinel host was confirmed in [30]. As in [12-14], the mechanism proposed in [30] is based on the assumption of a charge-transfer excitation from O²⁻ ($2p\sigma$) into the empty (3d)-orbital of Ti⁴⁺, resulting in Ti³⁺ in the electronic excited state with a subsequent emission of a photon from this titanium 3d-state stabilized by the interaction with lattice vibrations.

Thus, the titanium doped systems demonstrate interesting peculiarities of spectroscopic properties due to the possibility to embed Ti ions with different oxidation degrees into the host crystal. However, it is necessary to mention here that all cited papers deal with titanium doped chalcogenides or oxides.

The scientific research of α -ZnAl₂S₄ spinel type semiconductors, the host material object in this dissertation, has been done only by doping with ions of chromium. Optical properties of the chromium doped α -ZnAl₂S₄ have been examined in [31] in the temperature range 2–540 K. The intrinsic photoluminescence (PL) showed an intense ultraviolet peak at 381 nm at 296 K. From extrinsic absorption and emission spectra the transitions between the ground state $4A_{2g}$ and the excited levels $2E_g, 2T_{1g}, 2T_{2g}, 4T_{2g}$, and $4T_{1g}$ of Cr³⁺ ions were observed. A fit of the measured temperature dependence of the PL decay, using a four level model, yielded the lifetimes of the $2E_g, 2T_{1g}$, and $4T_{2g}$ levels and the energy gaps between the $2E_g-2T_{1g}$ and $2E_g-4T_{2g}$ states which were found to be very close to the values obtained from steady-state measurements. Optical gain measurements at 198, 298, and 380 K displayed two separate spectral regions associated to the Cr³⁺ ions and possibly Cr⁴⁺ impurity centres. Gain values of up to 25 cm⁻¹ at 198 K were obtained.

1.1.3. Cobalt ions as transition metal dopants in different matrices

The polarized absorption spectra of Co^{2+} in crystals of ZnO, ZnS, were measured at 4°K, 77°K, and room temperature in [32]. The spectra were interpreted by crystal field theory for the states of the $(3d)^n$ configuration acted on by a potential of predominately T_d symmetry. Certain details of the spectra were accounted for by smaller contributions from fields of a lower symmetry, notably a C_{3v} potential contribution for the transition metal ions in ZnO. The crystal field, electrostatic repulsion, and spin-orbit parameters were obtained for all those cases. An empirical correlation between the electrostatic repulsion parameter, B , for the ions in the crystals and the ligand polarizability was also obtained. Although the configuration mixing between the states of the configurations $(3d)^n$ and $(3d)^{n-1}(4p)$ was found to give a negligible contribution to the calculated relative energies of the levels, it does partially explain the large values of the observed intensities of the transitions. The relative intensities of transitions between the spin-orbit components were calculated by using models for both p – d mixing and σ bonding with the ligands.

Absorption and fluorescence spectra of Co^{2+} in the tetrahedral (T_d) site of ZnAl_2O_4 spinel (gahnite) at low temperatures were observed and analyzed in [33]. The resulting energy-level diagram included four quartet states and nine doublets, and was interpreted first in terms of weak field formalism without spin–orbit coupling. In that analysis the “free-ion” levels for $D_q=0$ were deduced and compared with those for a free ion outside the influence of the crystalline environment. The reduction in the electrostatic interaction parameters F_2 and F_4 in the crystal was due to the effect of covalence. Then another approach was used to analyze the fine structure of the energy levels in terms of the strong field spin–orbit formalism. The fine structure was explained for all the bands on the basis of simple spin–orbit splitting, but the possibility of a Jahn–Teller distortion of the $4T_{1g}$ state could not be entirely eliminated.

LiAl_6O_8 , ZnAl_2O_4 , and MgAl_2O_4 spinels, in pure form, as solid solutions with each other, or with sodium ion added, were used as host lattices for Co^{2+} ions[34]. The diffuse optical reflectance spectra and lattice constants of those solutions were measured and compared with predictions based on crystal field theory. The authors came to the conclusion that optical transition energies for cobalt ions in spinels indicate that crystal field parameters cannot be correlated to lattice constants by the predictions of crystal field theory. For Co^{2+} containing spinels, there is very little change in transition energies with composition of lattice constants, and small changes that do occur are nowhere nearer than required by the inverse fifth power law of the point charge approximation.

In [35] the absorption and luminescence of $\text{LiGa}_5\text{O}_8:\text{Co}$ were studied at various temperatures between liquid helium temperature and 500K. The spectra were assigned to transitions on Co^{2+} ions in tetrahedral sites. The luminescence transition was spin-allowed and was characterized by a very fast radiative decay rate. In [36] The $d-d$ spectra of $\text{Co}_x\text{Zn}_{1-x}\text{In}_2\text{S}_4$ solid solution at 300 and 77 K were interpreted on the assumption that a tetrahedral coordinated Co^{2+} ion predominated. The analysis of the absorption edge region allowed to make some comments on the cationic disorder within this solid solution.

The optical-absorption spectra of ZnGa_2S_4 and $\text{ZnGa}_2\text{S}_4:\text{Co}^{2+}$ polycrystalline powders were measured in the wavelength region 300–3000 nm in[37]. The optical energy gap was found to be 3.18eV for ZnGa_2S_4 crystal and 2.60eV for $\text{ZnGa}_2\text{S}_4:\text{Co}^{2+}$ crystal. The optical-absorption peaks in the measurement of $\text{ZnGa}_2\text{S}_4:\text{Co}^{2+}$ crystal absorption spectrum at 3790, 6049, 13725, 20704, and 22 79 cm^{-1} were found to be the electron transition of Co^{2+} ion with T_d symmetry from the ground state $^4A_2(^4F)$ to the excited states $^4T_2(^4F)$, $^4T_1(^4F)$, $^4T_1(^4P)$, $^2T_2(^2G)$, and $^2E(^2G)$. The crystal-field parameter and the Racah parameter, which were obtained from the optical-absorption peaks, were found to be $Dq=379 \text{ cm}^{-1}$ and $B=560 \text{ cm}^{-1}$, respectively. The $^4T_1(^4P)$ state of Co^{2+} ion splitted into three state of Γ_6 , Γ_8 , and $\Gamma_8+\Gamma_7$ by first-order spin-orbit coupling effects at 298 K. The value of the spin-orbit coupling parameter was $\lambda=-436\text{cm}^{-1}$.

The excitation, emission and decay time measurements in [38] also of Co-doped ZnGa_2O_4 indicated that the dopant was doubly charged and occupied the tetrahedral sites in the material. The observed visible and near infrared luminescent bands were assigned to the spin-allowed $^4T_1(^4P)\rightarrow^4A_2(^4F)$ and $^4T_1(^4P)\rightarrow^4T_2(^4F)$ transitions for a crystal field parameter Dq of 403cm^{-1} and the Racah parameter B of 766 cm^{-1} , respectively.

Optical absorption, luminescence, saturation of absorption and lifetime measurements have been carried out on Co-doped MgAl_2O_4 [39]. The authors estimated the crystal field parameter Dq of 400 cm^{-1} and the Racah parameters B of 730cm^{-1} and C of 3500cm^{-1} for the tetrahedral Co^{2+} ion. The luminescence bands observed in the visible range at 660 nm and in the near infrared one at 880 and 1270nm were assigned to transitions from the $^4T_1(^4P)$ level to the lower levels $^4A_2(^4F)$, $^4T_2(^4F)$, and $^4T_1(^4F)$, respectively. Strong luminescence quenching due to nonradiative decay processes was observed. Saturation of Co^{2+} absorption at 540 nm was measured and the absorption cross section was estimated to be $(2.1 \pm 0.2) \times 10^{-19} \text{ cm}^2$.

Optical absorption peaks and emission peaks of MnAl_2S_4 and MnAl_2Se_4 single crystals described as appearing due to Mn^{2+} ion sited in T_d symmetry were observed at 414,

450, 482, and 527nm in MnAl_2S_4 single crystal and at 416, 455, 488, and 532nm in MnAl_2Se_4 single crystal by authors in [40].

The impurity optical absorption peaks were observed in $\text{MgAl}_2\text{S}_4:\text{Co}^{2+}$ and $\text{CaAl}_2\text{S}_4:\text{Co}^{2+}$ single crystals[41]. The impurity absorption peaks in single crystals appeared in the two wavelength regions 700–900 nm and 1400–1800nm, and each group of the peaks consists of three peaks. The authors thought them to originate in electron transitions between energy levels of Co^{2+} ions sited in T_d symmetry in $\text{MgAl}_2\text{S}_4:\text{Co}^{2+}$ and $\text{CaAl}_2\text{S}_4:\text{Co}^{2+}$ single crystals.

The next paper [42] reported the application of ligand-field electronic absorption spectroscopy to probe Co^{2+} dopant ions in diluted magnetic semiconductor quantum dots. The authors found that standard inverted micelle coprecipitation methods for preparing Co^{2+} -doped CdS ($\text{Co}^{2+}:\text{CdS}$) quantum dots yielded dopant ions predominantly bound to nanocrystal surfaces. Those $\text{Co}^{2+}:\text{CdS}$ nanocrystals were unstable with respect to solvation of surface-bound Co^{2+} ; time-dependent absorption measurements allowed identification of two transient surface-bound intermediates involving solvent–cobalt coordination. Comparison with $\text{Co}^{2+}:\text{ZnS}$ quantum dots prepared by the same methods, which showed nearly isotropic dopant distribution, indicated that a large mismatch between the ionic radii of Co^{2+} (0.74 Å) and Cd^{2+} (0.97 Å) was responsible for exclusion of Co^{2+} ions during CdS nanocrystal growth. An isocrystalline core/shell preparative method was developed by the authors that allowed them to synthesize internally doped $\text{Co}^{2+}:\text{CdS}$ quantum dots through encapsulation of surface-bound ions beneath additional layers of CdS. The same authors in [43]reported the preparation and electronic absorption spectroscopy of Co-doped colloidal ZnO DMS-QDs. They used ligand-field electronic absorption spectroscopy as a dopant-specific optical probe to monitor dopant incorporation during nanocrystal growth and to verify internal substitutional doping in $\text{Co}^{2+}:\text{ZnO}$ and $\text{Ni}^{2+}:\text{ZnO}$ DMS-QDs. They concluded that the synthesis of colloidal oxide DMS-QDs introduced a new category of magnetic semiconductor materials available for detailed physical study and application in nanotechnology.

The optical energy gap and impurity optical absorption of Ga_2Se_3 and $\text{Ga}_2\text{Se}_3:\text{Co}^{2+}$ single crystals, which crystallize into cubic structures with a lattice constant of $a=5.442$ Å for Ga_2Se_3 and $a=5.672$ Å for $\text{Ga}_2\text{Se}_3:\text{Co}^{2+}$, were investigated in [44]. The optical energy gap of single crystals was found to be 2.070eV for Ga_2Se_3 and 1.931eV for $\text{Ga}_2\text{Se}_3:\text{Co}^{2+}$ at 298 K. The temperature dependence of the optical energy gap fitted well with the Varshni equation. Impurity optical absorption appeared in $\text{Ga}_2\text{Se}_3:\text{Co}^{2+}$ and was described in the framework of crystal field theory, as appearing due to an electron transition between the energy levels of Co^{2+} ion sited in T_d symmetry.

The spectroscopic investigations of Co^{2+} in $\text{SrLaGa}_3\text{O}_7$ single crystals were reported in [45]. The absorption spectra were taken at various temperatures from 15 to 300 K in the spectral range 190–2500 nm. It was found that Co^{2+} ions substituted octahedrally coordinated Sr^{2+} in the material. To consider the absorption line shape, the authors took into account the coupling of localised electrons to the symmetrical a_1 mode and the Jahn–Teller coupling of the $T \otimes \varepsilon$ and $T \otimes \tau$ types. An absorption line shape was reproduced considering the Fano anti-resonance of the broad band related to the ${}^4T_1 \rightarrow {}^4T_1$ transitions with sharp 2T_1 , 2T_2 , and 2T_1 states.

Transparent glass–ceramics containing zinc–aluminium spinel (ZnAl_2O_4) nanocrystals doped with tetrahedrally coordinated Co^{2+} ions grown by the sol–gel method were analysed for the first time in [46]. The dependence of the absorption and emission spectra of the samples on heat-treatment temperature were presented. The difference in the luminescence between Co^{2+} doped glass–ceramic and Co^{2+} doped bulk crystal was analysed. The crystal field parameter D_q of 423cm^{-1} and the Racah parameters B of 773cm^{-1} and C of 3478.5cm^{-1} were calculated for tetrahedral Co^{2+} ions.

Transparent glass-ceramics containing Co^{2+} : MgAl_2O_4 nanocrystals were obtained also by the sol–gel process. The structural evolution of the samples was studied with x-ray diffraction (XRD) and infrared spectra. Optical absorption spectra showed that Co^{2+} ions were located in tetrahedral sites replacing Mg^{2+} ions in MgAl_2O_4 nanocrystals. TEM revealed spherical nanocrystals of the size of about 5–15 nm, depending on the heat-treatment temperature. Co^{2+} : MgAl_2O_4 nanocrystals in the amorphous silica matrix proved to be very stable - up to 1100C without any decomposition.

Q switching of a diode-pumped Nd^{3+} : $\text{KGd}(\text{WO}_4)_2$ laser at $1.35\mu\text{m}$ by use of cobalt-doped magnesium- and zinc-aluminosilicate glass ceramics as saturable absorbers was demonstrated in [47]. Q -switching efficiency up to 40% was been obtained. Ground-state absorption cross sections for Co^{2+} ions at the wavelengths of 1.35 and $1.54\mu\text{m}$ were estimated to be $(3.5\text{--}4.0) \times 10^{-19}\text{cm}^2$. Bleaching relaxation times under the excitation of the ${}^4A_2 \rightarrow {}^4T_1({}^4F)$ transition of tetrahedrally coordinated Co^{2+} ions were of $280 \pm 50\text{ns}$ and $700 \pm 80\text{ns}$ for magnesium- and zinc-aluminosilicate glass ceramics, respectively.

Strong emission bands in the visible region observed in MgAl_2O_4 crystals doped with transition-metal ions under excitation at the band-to-band transitions were reported in [48]. The authors studied optical responses of Co doped MgAl_2O_4 and presented optical models to describe charge-transfer transitions and transitions between multiplet levels of $3d$ electrons, which are observed competitively or coexisting. The two kinds of transitions coexist in Co-

doped MgAl_2O_4 . Those behaviours are well understood based on the numerical results of the unrestricted Hartree-Fock approximation.

Anisotropy of the nonlinear absorption of Co^{2+} ions in MgAl_2O_4 single crystals at the wavelengths of 1.35 and 1.54 μm was experimentally demonstrated in[49]. The data obtained were analyzed in the framework of a phenomenological model, with Co^{2+} ions described as three sets of linear dipoles oriented along the crystallographic axes. Ground-state and excited-state absorption cross-sections at 1.35 and 1.54 μm were evaluated to be $\sigma_{\text{gsa}}=(4.0\pm 0.3)\times 10^{-19}$, $\sigma_{\text{esa}}=(3.6\pm 0.4)\times 10^{-20}\text{cm}^2$ and $\sigma_{\text{gsa}}=(5.1\pm 0.3)\times 10^{-19}$, $\sigma_{\text{esa}}=(4.6\pm 0.4)\times 10^{-20}\text{cm}^2$, respectively.

1.1.4. Vanadium ions as transition metal dopants in different matrices

One of the first attestations of the investigation of spectroscopic properties of vanadium ions was made in[50]. The generalized crystal field theory of Finkelstein and Van Vleck was augmented in that paper by the introduction of spin-orbit coupling; and an attempt was made to thus account for both the spin-allowed and the spin-forbidden d^2 spectral transitions of V(III) complexes. Secular equations were derived by the use of functions which span, in both the weak and strong crystalline field pictures, the proper spin-coordinate cubic symmetry classification of Bethe. The authors predicted spin-allowed infrared transitions at ~ 1.6 , ~ 168 , and $\sim 250\text{ cm}^{-1}$ for octahedral V(III) complexes. They also gave a rigorous theoretical interpretation of Low's spectral data on trivalent vanadium dissolved in aluminium oxide.

The polarized optical spectra of V^{3+} ions in corundum single crystals were studied at temperatures from 4.2° to 1200°K in [51]. A theory of the band strength based on the point-charge model and p - d mixing was developed by those authors and applied to the data with results that were in fair agreement with experiment. The effects of temperature showed that the vibrational-electronic contribution to band strength was quite small at low temperature but could be appreciable at high temperatures. The crystal-field parameters were calculated as convergent lattice sums. The observed trigonal-field parameter had the opposite sign from that calculated by the point-charge model if the impurity ion was assumed to occupy an Al^{3+} ion position in the lattice, but had the same sign as calculated for an ion 0.1 Å displaced along the c_3 axis towards the empty octahedral site. The authors interpreted the details of the spectra showing that the surroundings of an ion were distorted in some electronic states.

In order to study experimentally the properties of outer electrons as a function of inter-atomic separation through the transition region from narrow-band to localized properties, the spinels MV_2O_4 and M_2VO_4 , where $\text{M} = \text{Mn}, \text{Fe}, \text{Mg}, \text{Zn}$ and Co and $\text{M} = \text{Fe}$

and Co, were prepared and characterized by XRD and chemical analysis in [52]. The authors were of the opinion that conductivity measurements could all be represented by the localized-electron relationship $\rho = \rho_0 \exp(q/kT)$, but the measured q was sensitive to room-temperature cation-cation separation R , decreasing in the stoichiometric MV_2O_4 spinels from $0.37 \pm 0.01\text{eV}$ for $R = 3.013\text{\AA}$ in MnV_2O_4 to $0.07 \pm 0.005\text{eV}$ for $R = 2.972\text{\AA}$ in CoV_2O_4 . Attempts to prepare NiV_2O_4 were unsuccessful. Reduction of R by substitution of Al for V in $CoAl_xV_{2-x}O_4$ introduced a “foreign” ion into the vanadium sublattice, and q increased. Similarly Co_2VO_4 , with $R = 2.965\text{\AA}$ and a $Co^{2+} + V^{4+}$ B-site sublattice had a $q = 0.37 \pm 0.01\text{eV}$. Further evidence that a small energy is required to create a separated hole-electron pair within the vanadium sublattice came from the maxima at $x \sim 0.11$ in the q vs. x and θ vs. x curves for the system $Fe_{1+x}V_{2-x}O_4$, where $0 < x < 1$ and θ is the Seebeck voltage. Magnetization measurements indicated noncollinear spin configurations that indicate strong antiferromagnetic B - B interactions between vanadium cations. The data are compatible with the predicted V^{3+} - V^{3+} separation in oxides of $R_c \sim 2.97\text{\AA}$ for the transition from collective-electron to localized-electron behaviour.

Sharp-line fluorescence of the V^{2+} ion in magnesium oxide and corundum was studied in [53] at low temperatures, with and without a magnetic field. The results were analyzed in terms of crystal field theory, and the vibrational structure was briefly discussed. The variation of the crystal field parameters through the d^3 sequence V^{2+} , Cr^{3+} , Mn^{4+} was considered in terms of a point-charge model. The fluorescence spectrum of the V^{3+} ion the $Al_2O_3:V^{3+}$ system was discussed in [54].

Spinels in the system CuV_2S_4 - $CuCr_2S_4$ ($CuV_xCr_{2-x}S_4$) were prepared and studied in [55]. CuV_2S_4 is a superconductor and $CuCr_2S_4$ is metallic conducting and ferromagnetic ($T_c = 398\text{K}$). Magnetic measurements indicated that initially, from $x = 0$ to $x = 0.375$, the substituted vanadium ions exhibited essentially localized d -levels and magnetic moments magnetically polarized antiparallel to the carriers in the Cu d -band and parallel to the localized Cr^{3+} moments. The change from local to band behaviour for vanadium occurred over a rather small compositional range ($\Delta x = 0.125$). Magnetic properties of V-doped $MnCr_{2-x}V_xS_4$ were investigated in [56]. The authors demonstrated that compounds $MnCr_{2-x}V_xS_4$ existed in the spinel phase up to $x = 0.6$; that V substituted Cr in B sites; that V^{3+} coupled antiferromagnetically to Cr^{3+} ; and the transition temperature from the Yafet-Kittel to the Néel ferrimagnet decreased with x .

In CdS, vanadium on a cadmium site of C_{3v} symmetry represents a centre at which various luminescence processes take place at low temperatures, as was defined in [57]. Two emission bands with zero-phonon structures at $\nu = 8681\text{cm}^{-1}$ and $\nu = 4921\text{cm}^{-1}$ were ascribed to

internal transitions within V^{3+} ion, i.e., to transitions between levels produced in the crystal field by splitting the degenerate 3F term of the free ion: ${}^3T_1(F) \rightarrow {}^3A_2(F)$ and ${}^3T_2(F) \rightarrow {}^3A_2(F)$, respectively. A further broad emission band at $\nu = 14500 \text{ cm}^{-1}$ seemed to involve a vanadium donor which was a part of an associated centre. The calculated Tanabe-Sugano diagrams allowed an interpretation of the measured excitation spectra and yielded the fitted Racah and crystal-field parameters. Charge-transfer processes for vanadium and copper ions were discussed in the band model.

A high-resolution study of the vanadium-induced *A* and *B* luminescence zero-phonon lines in GaP:V and GaAs:V is presented in [58]. The analysis of the data definitely indicated that earlier assignments of lines *A* and *B* to $V^{2+} (3d^3)$ had to be revised and that *A*, *B* lines had to be assigned to the ${}^3T_2 \rightarrow {}^3A_2$ crystal-field transition of $V^{3+} (3d^2)$. The *A*-*B* splittings in a zero field were accounted for in terms of Ham's theory of the dynamic Jahn-Teller effect. The strength of the vibronic coupling was found to be moderate, $E_{JT/h\nu_0} \approx 3.7$, thus suggesting that a Jahn-Teller-induced static distortion did not occur. The dynamic Jahn-Teller model also provided a satisfactory description for the Zeeman splittings of lines *A* and *B*.

V^{2+} -doped $KMgF_3$, $KMnF_3$, $RbMnF_3$, $CsCaF_3$, $CsCdCl_3$, and $NaCl$ single crystals were analyzed with respect to their electronic properties and their suitability as laser material for vibronic-laser operation in [59]. All systems showed broadband emission and together covered the spectral range between 1.9 and $0.9 \mu\text{m}$. With $KMgF_3$, $KMnF_3$, $RbMnF_3$, and $CsCaF_3$ having the potential for tunable pulsed- or cw-laser operation at room temperature, laser emission with $NaCl:V^{2+}$ was to be expected below 200 K. The $CsCaF_3:V^{2+}$ material was successfully operated between 1.24 and $1.33 \mu\text{m}$.

At low temperatures, $ZnS:V$ crystals display three structured photoluminescence bands, as considered in [60]. Their individual fine structures, their behaviour under various conditions of preparation and excitation and their different excitation spectra demonstrated the presence of the charge states $V^{3+}(d^2)$, represented by the ${}^3T_2(F)$ to ${}^3A_2(F)$ emission band centred around 5600 cm^{-1} , $V^{2+}(d^3)$, represented by the ${}^4T_2(F)$ to ${}^4T_1(F)$ emission band around 4800 cm^{-1} ; and possibly $V^+(d^4)$, tentatively connected with an emission near 3800 cm^{-1} . A model of one-electron states was presented by the authors in which donor-type as well as acceptor-type changes of the vanadium oxidation states become comprehensible, commencing from V^{2+} , the state with a neutral effective charge. The excitation spectra for the V^{3+} and V^{2+} emission bands were interpreted based on both conventional and modified Tanabe-Sugano schemes. Modifications considered concerned mainly the inclusion of (i) a fit to the free-ion terms and of (ii) different radial extensions of t_2 - and e -type wavefunctions. Values were derived for the crystal-field splitting parameter Dq and the Racah parameters B and C . Also,

the authors presented evidence is for a Jahn-Teller splitting of the ${}^3T_1(P)$ V^{3+} and ${}^4T_1(P)$ V^{2+} levels.

At low temperatures, the photoluminescence of intentionally vanadium-doped ZnSe crystals displays (T approximately=4 K) the emission of V^{3+} (d^2), V^{2+} (d^3) and V^+ (d^4) ions with different no-phonon structures at 5440, 4740 and 3640 cm^{-1} , respectively[61]. The excitation spectra of the V^{3+} and V^{2+} luminescence bands were investigated separately. They exhibited structures of the respective spin-allowed as well as spin-forbidden internal transitions, which were largely in accordance with those of ZnS: V. The corresponding energy levels were approximated in a computation following the Tanabe-Sugano scheme. Furthermore, charge transfer processes at the luminescent centres were manifested in excitation, stimulation and transmission spectra. A vanadium ion proved to be an amphoteric impurity. Commencing from V^{2+} , the state with a neutral effective charge, light-induced transitions of donor and acceptor type were disclosed: V^{2+} to or from $V^{3+}+e_{CB}^-$ and V^{2+} to or from $V^++e_{VB}^+$.

The spectroscopic data of the authors in [62] concerning vanadium-doped YAG, YAl_2O_3 and Al_2O_3 showed that vanadium was incorporated in the trivalent and tetravalent states — despite the divalent codopant. The basic spectroscopy of V^{4+} is very similar to the corresponding Ti^{3+} doped crystals. In YAG, V^{4+} ions occupy not only the octahedral but also the tetrahedral site, which causes reabsorption losses of the V^{4+} fluorescence. The emission is further reabsorbed by a strong IR absorption band that extends into the fluorescence region. On the other hand, it is possible to grow $V^{4+}: Al_2O_3$ without the infrared band using a surplus of Mg^{2+} and oxidizing growth conditions, but in the latter case transient colour centres are produced by the pump light. The strong absorption of these colour centres covers the whole visible spectral region thus preventing laser action. Additionally, absorption from the excited state of V^{4+} occurs at the pumping wavelength of all investigated crystals. However, in $Al_2O_3: V, Mg$ this was a minor effect that furthermore reduced the pumping efficiency only by about 24%. No gain was observed in any crystal.

Electronic states of the normal vanadium spinels MV_2O_4 ($M=Mg$ and Zn) and the $Mg(V_{1-x}Al_x)_2O_4$ system were studied through the measurements of XRD, electrical resistivity, magnetic susceptibility and NMR of the ${}^{51}V$ and ${}^{27}Al$ nuclei[63]. According to the authors in the work mentioned, large Curie constants and Weiss temperatures in MV_2O_4 were found to be attributed to the spin frustration on the characteristic network of V ions.

Optical absorption peaks in absorption spectrum of the vanadium doped $ZnGa_2Se_4$ single crystals, grown by the chemical vapour transport method, at 6020, 9319, 12716, and 15290 cm^{-1} bands were found to be the electron transitions of V^{3+} ion with T_d symmetry from

the ground state ${}^3A_2({}^3F)$ to the excited states ${}^3T_2({}^3F)$, ${}^3T_1({}^3F)$, ${}^3T_1({}^3P)$, and ${}^1E({}^1G)$ [64]. Crystal-field parameter and the Racah parameters, obtained from the optical-absorption peaks, were found to be $Dq=602\text{ cm}^{-1}$, $B = 265\text{ cm}^{-1}$, and $C = 5294\text{ cm}^{-1}$, respectively. The authors also found out that the value of B was reduced by 70% compared to the V^{3+} free ion. The V^{3+} ion splits into three states: $\Gamma_3+\Gamma_5$, Γ_4 , Γ_1 by the first-order spin-orbit coupling effect. Hence, the spin-orbit coupling constant is $\lambda = -312\text{cm}^{-1}$.

In [65] luminescence from trivalent vanadium in tetrahedral oxo-coordination was observed in LiGaO_2 , LiAlO_2 , and SrAl_2O_4 . In LiGaO_2 , V^{3+} ion exhibited the most intense broad-band emission between 1400 and 2000nm with lifetimes of 89 and 11 μs at 12 and 300K, respectively. The decrease in the lifetime was mainly caused by non-radiative decay processes; the quantum efficiency at room temperature being about 2.5%. In LiAlO_2 and SrAl_2O_4 , the non-radiative quenching process was even stronger because of a smaller energy gap between the participating levels and the larger electron–phonon coupling. In all crystals, even at low temperature, significant non-radiative decay occurred.

Crystals of lanthanum orthogallate containing vanadium were grown by the Czochralski method and their optical spectra were measured at room and 5K temperature by the researchers in [66]. Absorption spectra of V-doped LaGaO_3 were attributed to V^{4+} and V^{3+} ions coexistent in the matrix whereas a short-lived and broadband luminescence recorded in the 12000–15000 cm^{-1} region was attributed to the ${}^2E-{}^2T_2$ transition of V^{4+} ions. The temperature has a weak influence on the luminescence spectrum. Overall intensity at 5 K was higher by roughly a factor of four, and the spectral position of the band maximum shifted to a higher energy by about 250 cm^{-1} with respect to luminescence spectra recorded at 300 K.

Theoretical results on the mechanism of two transitions in vanadium spinel oxides AV_2O_4 (A=Zn, Mg, or Cd) in which magnetic V cations constitute a geometrically frustrated pyrochlore structure were presented in[67]. The authors derived an effective spin-orbital-lattice coupled model in the strong correlation limit of the multiorbital Hubbard model, and applied Monte Carlo simulation to that model. The results revealed that the higher-temperature transition was a layered antiferro-type orbital ordering accompanied by a tetragonal Jahn–Teller distortion, and the lower-temperature transition was an antiferromagnetic spin ordering. The orbital order partially lifts the magnetic frustration and induces spatial anisotropy in magnetic exchange interactions. In the intermediate phase, the system can be considered to consist of weakly coupled antiferromagnetic chains lying in the perpendicular planes to the tetragonal distortion, the authors of the paper conclude.

Vanadium-doped gallium lanthanum sulphide glass (V:GLS) displays three absorption bands at 580, 730, and 1155nm identified by photoluminescence excitation

measurements, as demonstrated in [68]. Broad photoluminescence, with a full width at a half maximum of $\sim 500\text{nm}$, was observed peaking at 1500nm when excited at 514 , 808 , and 1064nm . The fluorescence lifetime and quantum efficiency at 300K were measured to be $33.4\mu\text{s}$ and 4% , respectively. From the available spectroscopic data, the authors admitted the vanadium ions' valence to be equal to $3+$ and be in tetrahedral coordination. Their results indicate a potential for the development of a laser or optical amplifier based on V:GLS.

Optical responses of V:MgAl₂O₄ are closer to those of Ti:MgAl₂O₄ as observed in [69]. The authors of the cited paper also described a white emission spectrum. Besides, the microscopic process of the white emission was proposed. Taking into account the fact that the relative intensity of 505 and 580nm emission of V: MgAl₂O₄ depends on the crystal growth condition; these two emissions were speculated to come from vanadium ions located at the B- and A-sites, respectively.

According to [70], vanadium-doped chalcogenide glass can be used as an active gain medium, particularly at telecommunications wavelengths. This dopant has three spin-allowed absorption transitions at 1100 , 737 and 578nm , and a spin-forbidden absorption transition at 1000 nm . X-ray photoelectron spectroscopy indicated the presence of vanadium in a range of oxidation states from V^+ to V^{5+} . Excitation of each absorption band resulted in the same characteristic emission spectrum and lifetime, indicating that only one oxidation state is optically active. Arguments based on the Tanabe–Sugano analysis indicated that the configuration of the optically active vanadium ion was octahedral V^{2+} . The calculated crystal field parameters (Dq/B , B and C/B) were 1.85 , 485.1 and 4.55 , respectively.

1.2. Theory of the optically active centres with *d*-electronic shell

1.2.1. Introduction: static interaction, Schrödinger equation and theory of crystalline field

A variety of interesting optical properties and applications of inorganic materials depend on the presence of so-called *optically active centres*. These centres consist of dopant ions that are intentionally introduced into a crystal during the growth process, or lattice defects (colour centres) that are created by various methods. Both types of localized centres provide energy levels within the energy gap of the material, so that they can result in the appearance of optical transitions at frequencies lower than that of the fundamental absorption edge.

Instead of considering how the incorporation of a dopant ion perturbs the electronic

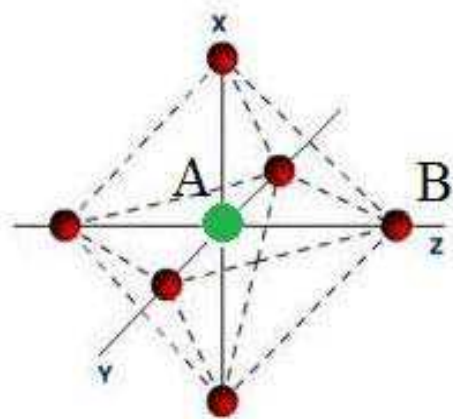


Fig.1.1 A scheme of an illustrative optical centre, AB_6 . This particular centre consists of a dopant optical ion A in an octahedral environment of B ions

structure of the crystal, the problem will be considered of understanding optical features of a centre by considering the energy levels of the dopant free ion (i.e., out of the crystal) and its local environment. In particular, first the energy levels of the dopant free ion will be considered in order to understand how these levels are affected by the presence of the next nearest neighbours in the lattice (the environment). In such a way, it became possible to practically reduce the system under discussion here to a one-body problem. In 1929

Bethe published a remarkable paper “Term splitting in crystals” that deals with atomic levels in crystals. It is assumed that an atom or ion with an unfilled electron shell is surrounded by point charges. A point-ion model of crystal field does not take into account the real electronic structure of ligands, the effect of covalent chemical bonding, and other factors. Let us consider a dopant ion A (the *CI - central ion*) placed at a lattice site, surrounded by an array of six regular lattice ions B (*ligand ions*), separated by a distance r from the ion A . The ligand ions B are located at the corners of an octahedron, as shown in Fig.1.1. The set comprised of ion A and six ligand ions B constitutes a pseudo molecule, AB_6 , which we call a *centre*. This is a common arrangement (centre) for optical ions in solids, called an octahedral arrangement, and we will use it in the text as our reference centre. Of course, many other arrangements around ion A are possible, but the strategy for solving each particular case is quite similar to the one for our selected octahedral centre. Those centres that bring about the appearance of optical bands are called

optically active centres. The qualitative discussion of the energy levels in the crystal field has revealed the relationship between the wave functions, the energy levels of quantum system, and the irreducible representations of its point group. Let us assume the ideal situation of a rigid (nonvibrating) lattice, so that the A – B distance a (Fig.1.1) remains fixed and corresponds to the time-average positions in the vibrating case. The energy levels of A are modified (shifted and split) by the influence of the ligand ions B through the electric field that they produce at the site of A – it is the well known in quantum mechanics Stark effect. This static electric field is commonly called the *crystalline field*.

In order to account for the optical absorption and emission bands of the AB_6 centre, we must first determine its energy levels E_i by solving the Schrödinger equation:

$$H\psi_i = E_i\psi_i \quad (1.1)$$

where H is a Hamiltonian that includes different interactions of the valence electrons in the AB_6 centre and ψ_i are eigenfunctions of the centre. Depending on the particular type of a centre, two main methodologies are commonly used to solve the Schrödinger equation(1.1): *Crystalline Field Theory (CFT)* and *Molecular Orbital Theory (MOT)*. They will be discussed separately.

In CFT, the valence electrons belong to ion A and the effect of the lattice is considered through the electrostatic field created by the surrounding B ions at the A position. It is then assumed that the valence electrons are localized in ion A and that the charge of B ions does not penetrate into the region occupied by these valence electrons. The exact numerical solution of the Schrödinger equation (1.1) for large molecular systems is at present, in general, an irrational task. The problem of electronic structure can be solved by introducing approximate methods of solution of Eq. (1.1) that allow us to obtain energies E_i and wave functions ψ_i in a convenient form and to evaluate the physical and chemical quantities with the required accuracy. Most approximations used in modern quantum physics are aimed at the separation of variables in Eq. (1.1). These approximations can be divided into two groups:

- The *adiabatic approximation* - it considers the ions that move very slowly in comparison to the valence electrons, so that the electronic motion takes place at a given nuclear coordinate (electrons move without perceiving changes in the nuclear positions). This approximation is reasonable as nuclei are much heavier than electrons, and therefore move on a much slower timescale. Within the adiabatic approximation, the nuclear and electronic motions can be solved independently and so the electronic energy can be drawn as a function of the distances A – B .

- The one-electron approximation – for a multielectron system – is based on the assumption that each electron moves independently in an averaged field created by all other

electrons and nuclei. This assumption allows us to perform a complete separation of the variables, that is, to describe the motion of the electron by its own coordinates, independent of the coordinates of other electrons. The one-electron approximation, although widely used, is, strictly speaking, not valid in many-electron systems because it neglects *electron correlation effects* but it is the most convenient starting approximation.

Thus the Hamiltonian can be written as

$$H = H_{\text{FI}} + H_{\text{CF}} \quad (1.2)$$

where H_{FI} is the Hamiltonian related to the free ion A (an ideal situation in which A ions are isolated, similar to a gas phase of these ions) and H_{CF} is the crystal field Hamiltonian that accounts for the interaction of the valence electrons of A with the electrostatic crystal field created by the B ions. The crystal field Hamiltonian can be written as:

$$H_{\text{CF}} = V(r_i, \theta_i, \phi_i) + W \quad (1.3)$$

where $V(r_i, \theta_i, \phi_i)$ is the potential energy created by the six B ions at the position (r_i, θ_i, ϕ_i) (given in spherical coordinates) of the i th valence electron of ion, and W is the electrostatic interaction of the positive charge Ze of the CI nucleus with the ligand charges (Z is the order number of the element in the periodic table and e is the absolute value of the electronic charge). In the particular case of point ligands, the interaction with crystals field is expressed as:

$$V(r_i, \theta_i, \phi_i) = - \sum_{i=1}^N \sum_{k=1}^{N^*} \frac{eq_k}{|r_i - R_k|} \quad (1.4)$$

and

$$W = \sum_{k=1}^{N^*} \frac{Ze q_k}{R_k} \quad (1.5)$$

where the indices i and k run over the N electrons and N^* nuclei respectively, and $|r_i - R_k|$ is the distance between the i th electron and k th nucleus with charge q_k . The summation is extended over the full number of valence electrons (N). If $q_k < 0$, then the term (1.5) provides the required CI -ligand negative interaction energy due to which the complex is stable. In this case the term V after (1.4) is positive, and hence the electron-ligand interaction destabilizes the complex. This situation is quite usual in real systems; the CI is electropositive and the ligands are electronegative. The term W is seldom considered in CFT explicitly because calculation of the absolute values of stabilization (bonding) energies is beyond the possibilities of this theory. On the other hand, W is independent of the electron coordinates, and therefore it is constant with respect to the electronic properties, considered in CFT .

In order to apply quantum mechanical perturbation theory, the free ion term is usually written as

$$H_{\text{FI}} = H_0 + H_{\text{ee}} + H_{\text{SO}} \quad (1.6)$$

where H_0 is the central field Hamiltonian (a term that reflects the electric field acting on the valence electrons due to the nucleus and the inner- and outer-shell electrons), H_{ee} is a term that takes into account any perturbation due to the Coulomb interactions among the outer (valence) electrons, and H_{SO} represents the spin–orbit interaction summed over these electrons. Depending upon the size of the crystal field term H_{CF} in comparison to these three free ion terms, different approaches can be considered to the solution of Equation (1.3) by perturbation methods:

- *Weak crystalline field:* $H_{\text{CF}} \ll H_{\text{SO}}, H_{\text{ee}}, H_0$. In this case, the energy levels of the free ion A are only slightly perturbed (shifted and split) by the crystalline field. The free ion wave functions are then used as basis functions to apply perturbation theory, H_{CF} being the perturbation Hamiltonian over the $^{2S+1}L_J$ states (where S and L are the spin and orbital angular momenta and $J=L+S$).

- *Intermediate crystalline field:* $H_{\text{SO}} \ll H_{\text{CF}} < H_{\text{ee}}$. In this case, the crystalline field is stronger than the spin–orbit interaction, but it is still less important than the interaction between the valence electrons. Here, the crystalline field is considered a perturbation on the ^{2S+1}L terms.

- *Strong crystalline field:* $H_{\text{SO}} < H_{\text{ee}} < H_{\text{CF}}$. In this approach, the crystalline field term dominates over both the spin–orbit and the electron–electron interactions.

To illustrate how the perturbation problem can be solved, we now describe one of the simplest cases, corresponding to an octahedral crystalline field acting on a single d^1 valence electron.

1.2.2. The crystalline field on d^1 optical ions

One of the simplest descriptions of the crystalline field is available for the d^1 outer electronic configuration (i.e., for a single d^1 valence electron). This means that $H_{\text{ee}}=0$ and, consequently, there is no distinction between intermediate and strong crystalline fields. Let us assume this outer electronic configuration for ion A of our AB_6 centre (Fig.1.1); that is, a d^1 electron in an octahedral crystalline field. For a free ion with an outer d^1 electron the 2D term is the fundamental energy state; with the total angular momentum $L=2$ and the total spin $S=1/2$, which leads to a fivefold degeneracy ($\chi=2L+1$) of the 2D term. To determine the splitting of the energy levels of a d^1 ion in an octahedral environment, the perturbation method has to be used. However, in order to understand the effect of the crystalline field over d^1 ions, it is very illustrative to consider another set of basis functions, the d orbitals displayed

in Fig. 1.2. These orbitals are real functions that are derived from the following linear combinations of the spherical harmonics:

$$\begin{aligned} d_{z^2} \propto Y_2^0, & \quad d_{x^2-y^2} \propto (Y_2^2 + Y_2^{-2}), \\ d_{xy} \propto i(Y_2^2 - Y_2^{-2}), & \quad d_{xz} \propto (Y_2^1 - Y_2^{-1}), \\ d_{yz} \propto i(Y_2^1 + Y_2^{-1}) \end{aligned} \quad (1.7)$$

Fig. 1.2 shows, due to its similar symmetry, that three d^1 orbitals (d_{xy} , d_{xz} , and d_{yz}) of the central ion are affected in the same way by the octahedral environment of the ligand ions; these orbitals will have the same energy. Although it is not so intuitive, it can also be shown that orbitals d_{z^2} and $d_{x^2-y^2}$ are affected in a similar way by the octahedral environment of the ligand ions, thus having equal energy. This means that the d fivefold degenerate energy state splits into two energy levels in an octahedral environment: a triply degenerate one, associated with the d_{xy} , d_{xz} , and d_{yz} orbitals (called t_{2g}), and another, doubly degenerate one, associated with the d_{z^2} and $d_{x^2-y^2}$ orbitals (called e_g). The nomenclature used for labelling the crystalline field split levels is based on group theory considerations, which are treated in specialized textbooks [71]. By further inspection of Fig. 1.2, we can clearly see that the lobes of the d_{xy} , d_{xz} , and d_{yz} orbitals are accommodated between oxygen ions.

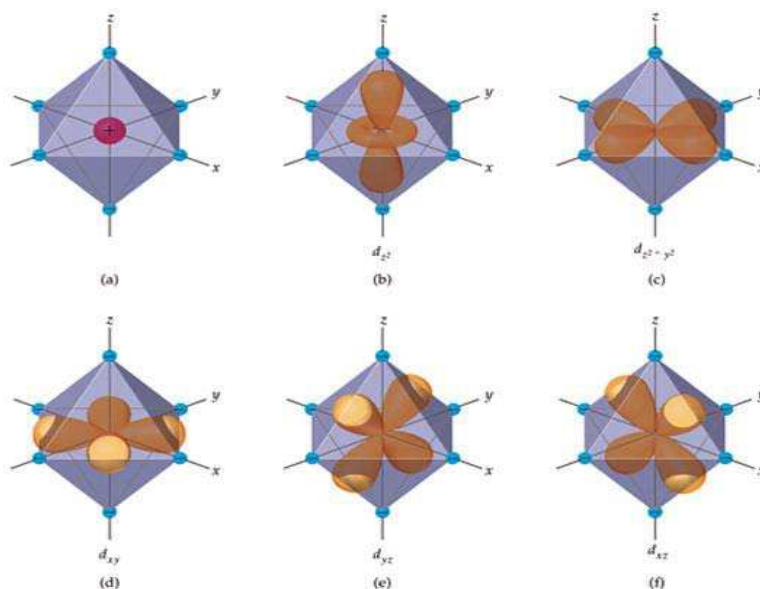


Fig. 1.2 Five d orbitals in an octahedral field: (a) an octahedral array of negative charges approaching a metal ion; (b) – (f): The orientation of d orbitals relative to the negative charges. Notice that the lobes of the d_{z^2} and the $d_{x^2-y^2}$ orbitals (b) and (c) point toward the charges, whereas the lobes of the d_{xy} , d_{yz} and d_{xz} orbitals; (d) – (f) point between the charges.

This produces a more stable situation (lower energy) than that for the d_{z^2} and $d_{x^2-y^2}$ orbitals, for which the lobes always point toward oxygen ions. This aspect suggests that the t_{2g}

energy level must lie below the e_g energy level, as shown in Fig. 1.3. The degenerated d terms of the ion in the octahedral ligand field are destabilised by the value:

$$E_0 = 6eqF(R) \quad (1.8)$$

where the E_0 is the average repulsion energy for all d electrons from the spherical field of the six negative ligands charges q placed at distance R from the central ion, F is the Slater – Condon parameter.

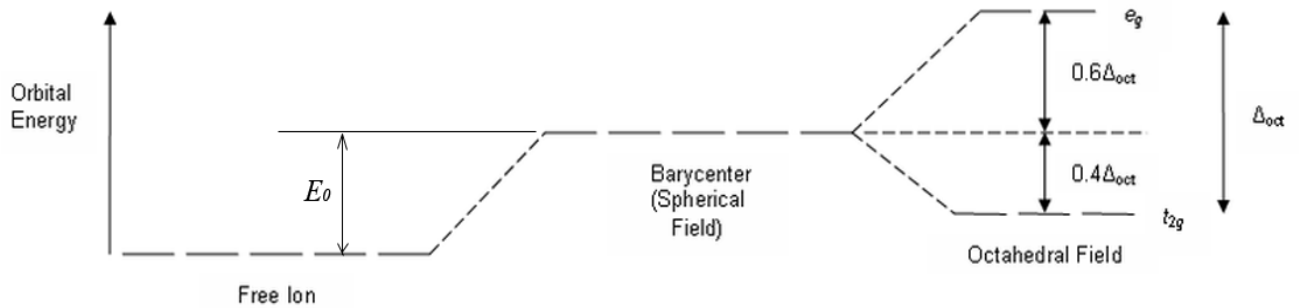


Fig. 1.3 Destabilization E_0 and splitting Δ of the atomic D term in the field of six ligands in an octahedral complex:

(a) free atom; (b) spherical averaged ligand field; (c) octahedral field.

Obviously the destabilization must be compensated for by the attraction term W between the CI core and ligands in (1.5); otherwise the complex is not stable. The energy separation between the t_{2g} and e_g energy levels is equal to the amount $\Delta = 10Dq$, where $D = 35Ze^2/4a^5$ is a factor that depends on the ligand B ions (here Ze being the charge of each ligand ion) and $q = (2/105) \langle r^4 \rangle$ (r being the radial position of the electron) reflects the properties of the d^1 valence electron. Therefore, we can write (in CGS units):

$$E_{e_g} - E_{t_{2g}} = 10Dq = \frac{10}{6} \frac{Ze^2 \langle r^4 \rangle}{a^5} \quad (1.9)$$

The Dq value is usually obtained from experimental measurements, and this value is considered to be an empirical parameter.

In many optically ion activated crystals the local symmetry of the active ion A is slightly distorted from the perfect octahedral symmetry (O_h symmetry). This distortion can be considered as a perturbation of the main octahedral field. In general, this perturbation lifts the orbital degeneracy of the t_{2g} and e_g levels and then produces additional structure in the $t_{2g} \leftrightarrow e_g$ absorption/emission bands. On the other hand, the crystalline field due to main symmetries other than O_h symmetry can be also related to the same case. For this purpose, it is useful to represent the octahedral structure of our reference AB_6 centre as in Fig. 1.4a. In this representation, the B ions lie in the centre of the six faces of a regular cube of side $2a$ and ion A (not displayed in the figure) is in the cube centre; the distance $A-B$ is equal to a . The advantage of this representation is that other typical arrangements can also be displayed using

this regular cube, as shown in Fig. 1.4b and Fig. 1.4c. The arrangement in Fig. 1.4 corresponds to an AB_4 centre with a tetrahedral structure. This arrangement (T_d symmetry) consists of four ligand B ions located at the alternate vertices of a regular cube – that is, at the vertices of a regular tetrahedron – while ion A lies at the cube centre. If the cube side is preserved as $2a$, then the distance A–B is $a\sqrt{3}$. The arrangement of Fig. 1.4c corresponds to an AB_8 centre with cubic symmetry (O_h symmetry).

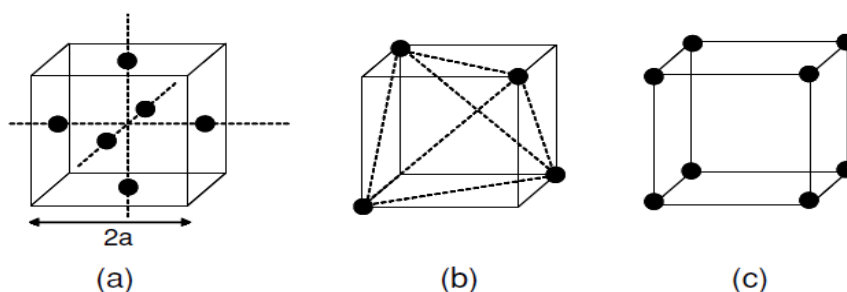


Fig. 1.4 The arrangement of B ligand ions (black dots) around central ion A (located in the cube centre, but not displayed in the figure): (a) octahedral, (b) tetrahedral, and (c) cubic.

This centre can be visualized by locating eight B ligands at the cube corners, with the central ion A at the cube centre. Again, the distance A–B is $a\sqrt{3}$. The regular cube used in Fig. 1.4 to represent different symmetry centres suggests that these symmetries can be easily interrelated. It can be shown that the crystal field strengths, $10Dq$, of the tetrahedral and cubic symmetries are related to that of the octahedral symmetry. Assuming the same distance A–B for all three symmetries, the relationships between the crystalline field strengths are as follows [71]:

$$Dq(\text{octahedral}) = -\frac{9}{4}Dq(\text{tetrahedral}) = -\frac{9}{8}Dq(\text{cubic}) \quad (1.10)$$

The crystalline field splitting in octahedral symmetry is larger by a factor of 9/4 than in tetrahedral symmetry, and larger by a factor of 9/8 than in cubic symmetry. The minus sign indicates an inversion of the e_g and t_{2g} levels with respect to the octahedral field, as shown in Fig. 1.5. For a tetrahedral complex the qualitative picture of the term splitting is inverse to that of the octahedral case. Indeed, in the tetrahedral environment of four ligands the t_{2g} orbitals are oriented with their lobes much closer to the ligands than are the e_g orbitals, and hence the former are subject to stronger repulsion than the latter. Therefore the energy levels of the t_{2g} orbitals are higher than those of e_g . However, in contrast to the octahedral case the splitting magnitude, as well as the destabilization energy, is smaller.

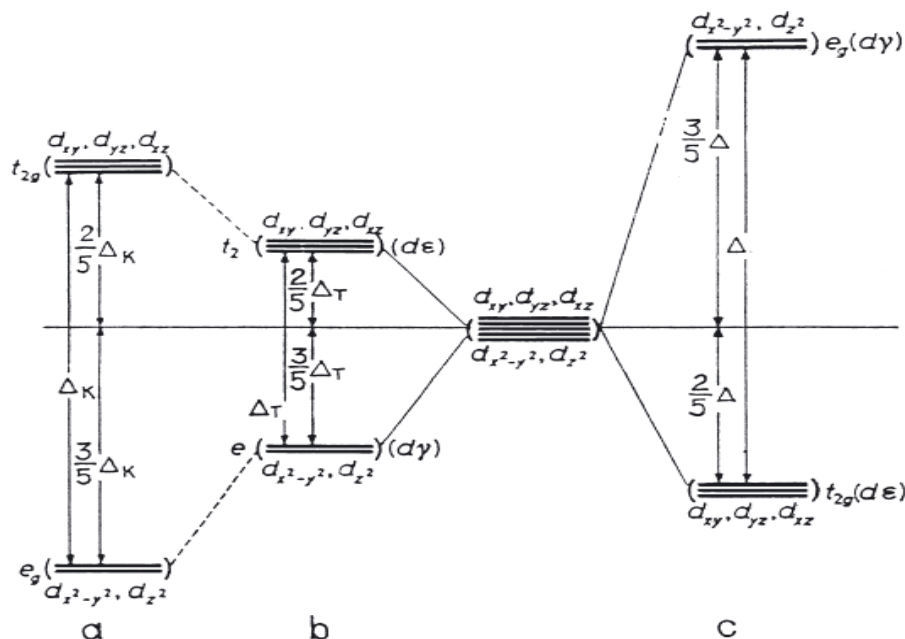


Fig. 1.5 Splitting of D term in cubic (a), tetrahedral (b), and octahedral (c) fields of the ligands [72].

If the symmetry of the ligand field is lowered, the terms t_{2g} and e_g may be subject to further splitting. Consider the case of a tetragonally distorted octahedron formed by the elongation of the regular octahedron along one of its diagonals, say, z . In this case the energies of the two e_g orbitals, $d_{x^2-y^2}$ and d_{z^2} , are no longer equal, since the repulsion is lower in the latter.

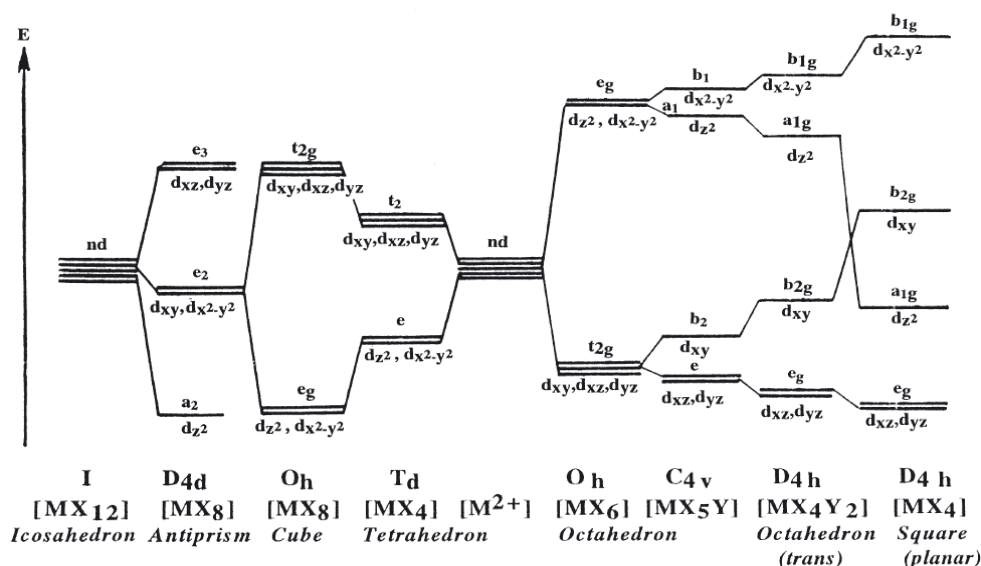


Fig. 1.6 Splitting of d orbital energy levels in ligand fields of different symmetries[72].

The three t_{2g} states do not remain equivalent, either; two of them, d_{xz} and d_{yz} , experience (equally) less repulsion from the ligands than does d_{xy} . Therefore, in the tetragonally distorted octahedron the atomic D term splits into four terms, from which only e_g (d_{xz}, d_{yz}) remains twofold-degenerate (Fig. 1.6). If the symmetry of the ligand field is further

lowered (e.g., if the two axes, x and y , are non-equivalent), the twofold-degenerate term splits as well.

For a CI with more than one d electron, the visual interpretation of splitting becomes more complicated but the main idea remains the same; in the CFT model the energies of the states that are degenerate in the free atom (ion) may differ because of the variation in repulsion from the ligands.

1.2.3. Group theory and spectroscopy

The calculation of electronic energy levels and eigenfunctions is far from a simple task for the majority of centres. The calculation of transition rates and band intensities is even more complicated. Thus, in order to interpret the optical spectra of ions in crystals, a simple strategy becomes necessary. This strategy consists of analysis of the symmetry properties for the active centre (i.e., the ion and its local environment) and it is extremely useful for interpreting optical spectra without tedious calculations. Indeed, the symmetry properties of the active centre are also the symmetry properties of its corresponding Hamiltonian. Thus, among other applications, symmetry considerations are useful in solving some spectroscopic problems, such as:

- Determining the number of energy levels of a particular active centre.
- Labelling these electronic energy levels in a proper way (irreducible representations) and determining their degeneracy.
- Predicting the energy level splitting induced by reduction in symmetry.
- Establishing selection rules for optical transitions and determining their polarization character.
- Determining the symmetry properties of the active centre eigenfunctions.
- Analyzing the vibrations of a complex (centre).

It is not the purpose of the present work to deal with all of the aspects related to this impressive capability, but it is worth trying to give some basic considerations on how to apply group theory concepts to simple problems in optical spectroscopy. A detailed description of group theory and its applications in spectroscopy can be found in specialised textbooks, e.g.[71].

In spite of a large variety of active centres (molecules, ions in solids, colour centres, etc.), it can be demonstrated that only 32 point symmetry groups exist in nature. These 32 point symmetry groups (denoted by the so-called *Schoenflies symbols*) are listed in [73]. The 32 symmetry groups are classified into seven *crystalline systems*; each point group containing a given number of symmetry operations grouped into the classes. The number of elements

(symmetry operations) in the point group is called the group order g . For example, the point group O_h belonging to the cubic crystalline system contains 48 symmetry operations grouped into 10 classes, thus the group order g is 48. In order to use group theory in spectroscopic applications, it is necessary first of all to determine the symmetry group of the object being investigated. The $ZnAl_2S_4$ has a face centred cubic structure belonging to the O_h point symmetry group.

Each specific symmetry operation R can be associated with a matrix M acting over the basic functions x , y , and z of the vector (x, y, z) . Thus, we can represent the effect of the 48 symmetry operations of group O_h (AB_6 centre) over the functions (x, y, z) by 48 matrices. This set of 48 matrices constitutes a *representation*, and the basic functions x , y , and z are called *basis functions*. As an example, the symmetry operation (rotation) of Fig. 1.7 transforms the set of basis functions (x, y, z) into $(y, -x, z)$.

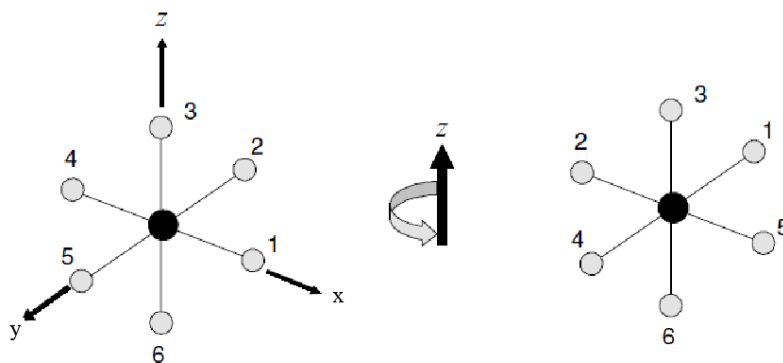


Fig. 1.7 Effect of a 90° rotation around an axis of the AB_6 centre. After the transformation the coordinates (x, y, z) became $(y, -x, z)$

This transformation can be written as a matrix equation:

$$(y, -x, z) = (x, y, z) \begin{pmatrix} 0 & -1 & 0 \\ 1 & 0 & 0 \\ 0 & 0 & 1 \end{pmatrix} \quad (1.11)$$

Obviously, there is another set of 48 matrices (another representation) which can be constructed after the effect of the O_h symmetry operations over a different set of orthonormal basis functions. It is then clear that *each set of orthonormal basis functions ϕ_i generates a representation Γ* so that, as in (1.11), we can write a transformation equation as follows:

$$R\phi_i = \sum_j \phi_j \Gamma^{ji}(R) \quad (1.12)$$

where R is a symmetry operation and the $\Gamma^{ji}(R)$ are the components of the matrix.

Now, if a suitable *space of basis functions* is used (a space of basis functions that is closed under the symmetry operations of the group), we can construct *a set of representations* (each one consisting of 48 matrices) for this space. It is especially important that the matrices

of each one of these representations can be made equivalent to matrices of lower dimensions. The representations that involve the lowest-dimension matrices are called *irreducible representations* and have a particular relevance in group theory.

Thus, any representation Γ can be expressed as a function of its irreducible representations Γ_i . This operation is written as $\Gamma = \sum a_i \Gamma_i$, where a_i indicates the number of times that Γ_i appears in the reduction. In group theory, it is said that *the reducible representation Γ is reduced into its Γ_i irreducible representations*. The reduction operation is the key point for applying group theory in spectroscopy. To perform a reduction, we need to use the so-called *character tables*.

To construct the character table for the O_h symmetry group it is necessary to apply the symmetry operations of the AB_6 centre over a particularly suitable set of basis functions: the orbital wave functions s, p, d . . . of atom (ion) A . These orbitals are real functions (linear combinations of the imaginary atomic functions) and the electron density probability can be spatially represented. In such a way, it is easy to understand the effect of symmetry transformations over these atomic functions.

For example, Fig. 1.8 shows the effect of a $C_4(001)$ symmetry operation on the p_x , p_y , and p_z orbitals. This operation converts the orbital p_x into the orbital p_y and the orbital p_y into the orbital $-p_x$, while the orbital p_z is unaffected.

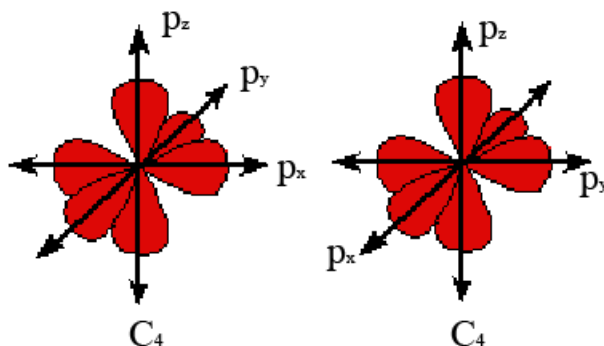


Fig. 1.8 The effect on p orbitals of a $C_4(001)$ operation (clockwise sense).

We can equate these transformations as follows:

$$(p_y, -p_x, p_z) = (p_x, p_y, p_z) \begin{pmatrix} 0 & -1 & 0 \\ 1 & 0 & 0 \\ 0 & 0 & 1 \end{pmatrix} \quad (1.13)$$

so that the $C_4(001)$ operation can be represented by the square matrix of this equation.

If to take into consideration other 47 symmetry operations of the O_h group acting on the same p orbitals, then it is possible to obtain a set of 48 square matrices: a representation of the O_h group associated with these orbitals. The traces of these matrices (the sums of their diagonal elements) are called *characters* in group theory and are denoted χ . For instance, the

character of the 3×3 matrix in(1.13) is equal to 1. If the zero elements in this 3×3 matrix are ignored and the ± 1 elements denote the initial (*I.p.*) and final (*F.p.*) positions of the orbitals, the following scheme can represent the symmetry transformation given by (1.13):

F.p. \ I.p.	p_x	p_y	p_z
p_x		-1	
p_y	+1		
p_z			+1

An inspection of this scheme shows that the character (+1) of the transformation matrix given in(1.13) has some physical sense: in this case, it indicates that only one orbital, the p_z , is unchanged by the symmetry operation $C_4(001)$ (see Fig. 1.7). In a broader sense, the character of any symmetry transformation gives an indication of the number of orbitals that are “unchanged” after this transformation. However, the *character can also be negative*, as happens with the *inversion symmetry operation i*.

An important conclusion envisaged from the previous paragraph is that *all of the information* needed for a symmetry operation *is contained in the character* of the matrix associated with this operation. This leads to the first great simplification: we do not need to write the full matrix associated with any transformation – its character is sufficient. In a similar way, we can examine the effect of other symmetry operations of the O_h group over the (p_x, p_y, p_z) orbitals and so write their associated characters. It should be noted that symmetry operations belonging to the same class have the same character, for a given basis function. Here, we obtain a second important simplification: it is necessary only to *work with classes*, instead of invoking *all of the symmetry operations* (48 in the case of the O_h group).

In fact, the full information for a given point group is given by its *character table*. This table contains the character files of a particular set of representations: the *irreducible representations*. Table 1.1 shows the *character table of the O_h point group*. A character table, such as Table 1.1, contains the irreducible representations (10 for the O_h group) and their characters, the classes (also 10 for the O_h group), and the set of basis functions. An inspection of this table is very instructive to infer some group theory properties that can be formally demonstrated:

- The number of *classes* is equal to the number of *irreducible representations*
- The set of characters (also called the *character*) of a representation is *unique*.
- The *dimension* (that is the dimension of the matrices) of each irreducible representation *is given by the character corresponding to class E*.

- The sum of the squares of the dimensions of irreducible representations is equal to the order of the group g :

$$g_1^2 + g_2^2 + g_3^2 + \dots + g_n^2 = g \quad (1.14)$$

where g_1, g_2, \dots, g_n are the dimensions of the irreducible representations, of which there are n (equal to the number of classes).

- The sum of the squared characters of each irreducible representation is equal to the order of group:

$$\sum_R [\chi^\Gamma(R)N]^2 = g \quad (1.15)$$

where the χ^Γ is the character of each operation R of the irreducible representation Γ and the summation is done over all group operations.

Table 1.1 A character table for the O_h point group

O_h	E	$8C_3$	$6C_2$	$6C_4$	$3C_2'$	I	$6S_4$	$8S_6$	$3\sigma_h$	$6\sigma_d$	
A_{1g}	1	1	1	1	1	1	1	1	1	1	s
A_{2g}	1	1	-1	-1	1	1	-1	1	1	-1	
E_g	2	-1	0	0	2	2	0	-1	2	0	$(d_{z^2}, d_{x^2-y^2})$
T_{1g}	3	0	-1	1	-1	3	1	0	-1	-1	
T_{2g}	3	0	1	-1	-1	3	-1	0	-1	1	(d_{xz}, d_{yz}, d_{xy})
A_{1u}	1	1	1	1	1	-1	-1	-1	-1	-1	
A_{2u}	1	1	-1	-1	1	-1	1	-1	-1	1	f_{xyz}
E_u	2	-1	0	0	2	-2	0	1	-2	0	
T_{1u}	3	0	-1	1	-1	-3	-1	0	1	1	$(p_x, p_y, p_z) (f_{x^3}, f_{y^3}, f_{z^3})$
T_{2u}	3	0	1	-1	-1	-3	1	0	1	-1	$(f_{x(y^2-z^2)}, f_{y(z^2-x^2)}, f_{z(x^2-y^2)})$

There are several systems of notation for the irreducible representation of the point groups. The most widely used is the following Mulliken system, which is generally accepted in spectroscopy:

- The representations A and B (which are not given in Table 1.1) are mono-dimensional, E representations are bi-dimensional, and T representations are three-dimensional. The dimension of a representation gives the degeneracy of its associated energy level.

- Subscripts 1 and 2 on the symbols A and B denote, respectively, the symmetric and antisymmetric behaviour of the basis functions relative to C_2' axes or to the vertical plane σ_v and σ_d .

- The subscripts u (*ungerade* = odd) and g (*gerade* = even) indicate whether an irreducible representation is symmetric (g) or anti-symmetric (u), in respect to the inversion operation (i).

The Bethe system of notation is also widely used. In this, the irreducible representations are denoted by the Γ_1, Γ_2 etc. Even representations are denoted by the Γ_i^+ and odd ones by the Γ_i^- .

1.2.4. Splitting of energy levels in crystal field

A very common problem in spectroscopy is to predict and label the energy levels of an active ion in a crystal from the energy levels of the free ion; that is, from the energy levels of the ion out of the crystal. This “free ion” case can be treated like that corresponding to a group that contains all rotational angles about any axis. This group has an infinite number of symmetry elements and is known as the *full rotation group*. In this group, all rotations through the same angle about any axis belong to the same class. Therefore, there is an infinite number of classes and, consequently, an infinite number of irreducible representations. Considering that the free ion energy-level scheme can be described by $^{2S+1}L_J$ states, the procedure is to construct the irreducible representations in the full rotation group corresponding to these states. These representations will be labelled as D_J and, in general, they correspond to reducible representations in the symmetry group of the ion in the crystal. Let us call this generic group G . Once the D_J representations have been constructed, the next step is to carry out the decomposition of these representations into irreducible representations Γ_i of the G group; that is, $D_J = \sum a_i \Gamma_i$. For the spherical group the characters of the matrices of the representations for a rotation by an angle α can be calculated by the following formula:

$$\chi(\alpha) = \frac{\sin(J + \frac{1}{2})\alpha}{\sin(\frac{\alpha}{2})} \quad (1.16)$$

When an atom is introduced in an external field of, for instance, O_h symmetry, the symmetry of the system as a whole (the atom plus the field) becomes O_h , and only those symmetry transformations (rotations) that comply with the O_h restrictions remain. The number of symmetry transformations is thus reduced, which means that the irreducible representations of the spherical group, to which the atomic term of $(2L+1)$ -fold degeneracy belongs, may become reducible in the O_h group. The reducible representation can be decomposed into several irreducible representations of smaller dimensionality, to which several energy terms of lower degeneracy belong — the term splits.

Group theory is very useful to unequivocally predict the number of split components and their degeneracy (of course, the amount of splitting for a given energy level cannot be predicted by group theory). To resolve this problem, it is first necessary to know how a given representation Γ is reduced to its irreducible representations Γ_i ; in other words, to determine

the coefficients a_i in the equation $\Gamma = \sum a_i \Gamma_i$. Although this is a key problem in group theory, here we only explain how to perform this reduction without entering into formal details, which can easily be found in specialized textbooks. It can be shown that the number of times a_i that the irreducible representation Γ_i appears in Γ is given by:

$$a_i(\Gamma_i) = \frac{1}{g} \sum_R \chi^\Gamma(R) \chi^{\Gamma_i}(R) \quad (1.17)$$

where $a_i(\Gamma_i)$ is the number of times Γ_i occurs in the reduction, g is the group order, $\chi^\Gamma(R)$ and $\chi^{\Gamma_i}(R)$ are, respectively, the characters of Γ and Γ_i for the operation R . In such a way it is possible to predict and label the energy terms of any one-electron or many-electrons ions.

1.2.5. Several d electrons in crystalline field of ligands. Case of weak field

If the electron configuration of the CI contains more than one d electron above the closed shell, the picture of possible energy terms and their splitting in the ligand fields is significantly complicated by the interaction between the d electrons. If the ligand field is not very strong, the atomic terms can still be classified by the quantum number of the atomic total momentum L , and the influence of the ligands can be taken as a perturbation of the atomic terms; this is *the case of weak ligand field*. Consequently, under the influence of a weak field of ligands, the LS coupling between the d electrons is not destroyed, and the term with the highest spin is the ground term. Therefore the complexes with weak ligand fields are also called *high-spin complexes*. For several d electrons the main effect of ligand fields, as for one d electron, is energy term splitting. However, unlike the d^1 case, the visual interpretation of the splitting of the terms of d^n configuration ($n > 1$) is difficult. But the cause of splitting is the same; in the ligand field, the atomic (multielectron) states that have the same energy in the free atom (ion), are subject to different repulsion from the ligands owing to their different orientation with respect to these ligands.

The method of classification of the one-electron states in crystal field is easily generalized to the case of many-electrons ions. Quantitatively, for the electronic configuration of the $CI I(nd)^2$ in the ligand field, which is weaker than the interaction between the d electrons, one can consider first the possible states of the free atom (ion) and find its terms and then determine the influence of the ligand field as a perturbation for each of these terms separately [71]. For two d equivalent electrons the possible terms, according to the Russel – Saunders coupling scheme are 3F , 3P , 1G , 1D , and 1S , with the 3F term being the ground state after the Hung rules. The many-electron wavefunctions of these terms represent the basis functions of the $(2L+1)$ – dimensional representation in the full rotational group, which split in the crystal field of the ligands according to (1.17). The splittings of the free ion terms in the

irreducible representations in the O_h crystalline field of the ligands are illustrated in Fig. 1.9; the

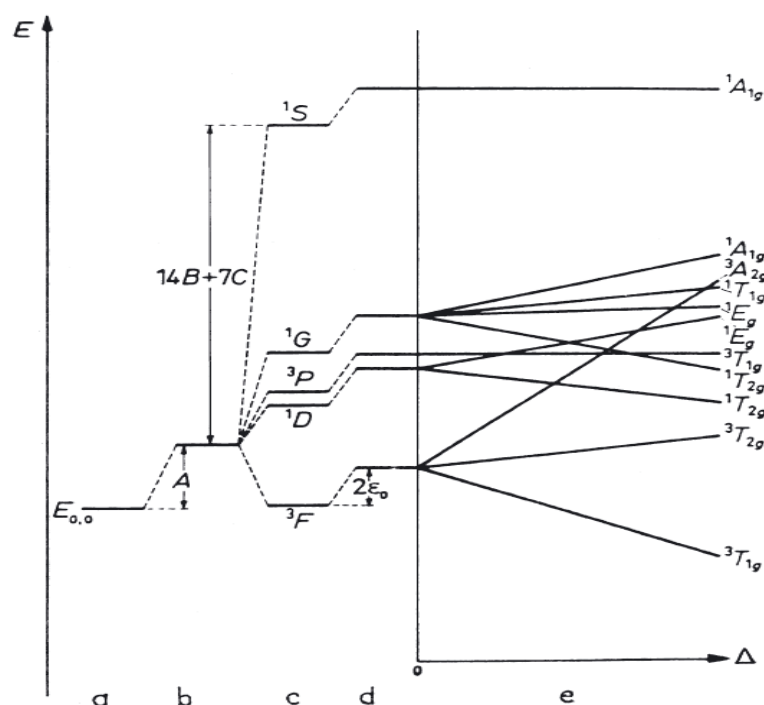


Fig. 1.9 Splitting of the terms of the electronic d^2 configuration in octahedral ligand fields in the weak-field limit [72]: (a) d -electron energy level; (b) interelectron interaction (spherical averaged part); (c) interelectron interaction—formation of atomic terms ; (d) ligand field destabilization; (e) ligand field splitting as a function of Δ .

destabilization energy—the averaged electron interaction equal to the Racah parameter A – is also shown. The calculations are carried out in the weak-field approximation, in which the perturbation theory is applied to each atomic term separately. Therefore, *the criterion of validity of the weak-field approximations is that the term splitting is much smaller than the energy gap between the terms*. As seen from Fig. 1.9, for d^2 configurations this

Table 1.2 Correlations of irreducible representations of O_h and D_{4h} symmetry groups with their subgroups indicating the corresponding symmetry transformations and splitting.

Group	Subgroup			Group	Subgroup	
	T_d	D_{4h}	D_3		D_{4h}	C_{4v}
A_{1g}	A_1	A_{1g}	A_1	A_{1g}	A_1	A_1
A_{1u}	A_2	A_{1u}	A_1	A_{1u}	A_2	A_2
A_{2g}	A_2	B_{1g}	A_2	A_{2g}	A_2	B_1
A_{2u}	A_1	B_{1u}	A_2	A_{2u}	A_1	B_2
E_g	E	$A_{1g} + B_{1g}$	E	B_{1g}	B_1	A_1
E_u	E	$A_{1u} + B_{1u}$	E	B_{1u}	B_2	A_2
T_{1g}	T_1	$A_{2g} + E_g$	$A_2 + E$	B_{2g}	B_2	B_1
T_{1u}	T_2	$A_{2u} + E_u$	$A_2 + E$	B_{2u}	B_1	B_2
T_{2g}	T_2	$B_{2g} + E_g$	$A_1 + E$	E_g	E	$A_2 + B_2$
T_{2u}	T_1	$B_{2u} + E_u$	$A_1 + E$	E_u	E	$A_1 + B_1$

criterion is fulfilled if Δ is sufficiently small. For large Δ values the components of the split terms even cross each other, rendering the approximation of weak field invalid. For complexes with symmetries lower than O_h the degenerate terms are subject to further splitting as shown in Table 1.2.

1.2.6. Strong crystalline field and low- and high-spin complexes

In the other limit case, opposite to the weak-field one, the effect of the ligand field on the states of the CI is strong; it surpasses the electrostatic interaction between the electrons. In this case the orbital coupling between the electrons is broken and the states with definitive total momentum quantum numbers L (S, P, D , etc., states), strictly speaking, cease to exist. In other words, each d electron chooses its orientation in space under the influence of the ligand field rather than the other d electrons. This is the *strong-ligand-field limit*. It follows that when the ligand field is strong, it makes no sense to speak about atomic term splitting, since the terms themselves are destroyed. To determine the states in this case, one should first find the orientations of each d state in the ligand field neglecting the electron interaction, and then evaluate the possible terms of the system taking into account the interaction of the electrons in these crystal-field-oriented electronic states.

As was shown above, for one d electron in the octahedral field of the ligands there are two non-equivalent kinds of orbital states: the more stable t_{2g} states (d_{xy}, d_{xz}, d_{yz}) in which the electrostatic repulsion from the six ligands is smaller, and the less stable (higher in energy by Δ) states e_g ($d_{z^2}, d_{x^2-y^2}$) in which the repulsion from the ligands is larger. Hence in a strong ligand field, neglecting the electron interaction, the d electrons occupy first the t_{2g} orbitals (maximum six electrons) and then the e_g orbitals (four electrons); the electron configuration is $(t_{2g})^n$ for $n \leq 6$, and $(t_{2g})^6(e_g)^{n-6}$ for $n > 6$. The energy terms can be obtained from these configurations by including the electron interaction.

Consider the atomic electron configuration $[I](nd)^2$. In strong ligand fields, as stated above, the two d electrons in the ground state of an octahedral complex occupy two t_{2g} orbitals (the state with two electrons in one orbital is higher in energy) forming the $(t_{2g})^2$ configuration. In the excited states one of the two d electrons can occupy the e_g orbital and form the $(t_{2g})^1(e_g)^1$ configuration, which is higher than $(t_{2g})^2$ by Δ , and the two electrons can occupy the e_g orbitals, resulting in the excited $(e_g)^2$ configuration, also higher by Δ than $(t_{2g})^1(e_g)^1$ [and by 2Δ than $(t_{2g})^2$]. Thus the d^2 configuration in the strong octahedral field forms three configurations, $(t_{2g})^2$, $(t_{2g})^1(e_g)^1$, and $(e_g)^2$, situated consecutively with an energy spacing Δ . In each of these configurations the electron interaction yields several terms similar

to the term formation in the free atom. The resulting terms for the $(t_{2g})^2$ configuration expressed by the Racah parameters are as follows:

$$\begin{aligned}\varepsilon(^3T_{1g}) &= A - 5B \\ \varepsilon(^1T_{2g}) &= A + B + 2C \\ \varepsilon(^1E_{1g}) &= A + B + 2C \\ \varepsilon(^1A_{1g}) &= A + 10B + 5C\end{aligned}\tag{1.18}$$

Splitting of the configurations that emerge from d^2 is shown in Fig. 1.10. In particular, the ground state of the $(t_{2g})^2$ configuration $^3T_{1g}$ is the same as in the weak-field limit. However, the sequence and spacing of the excited states are essentially different.

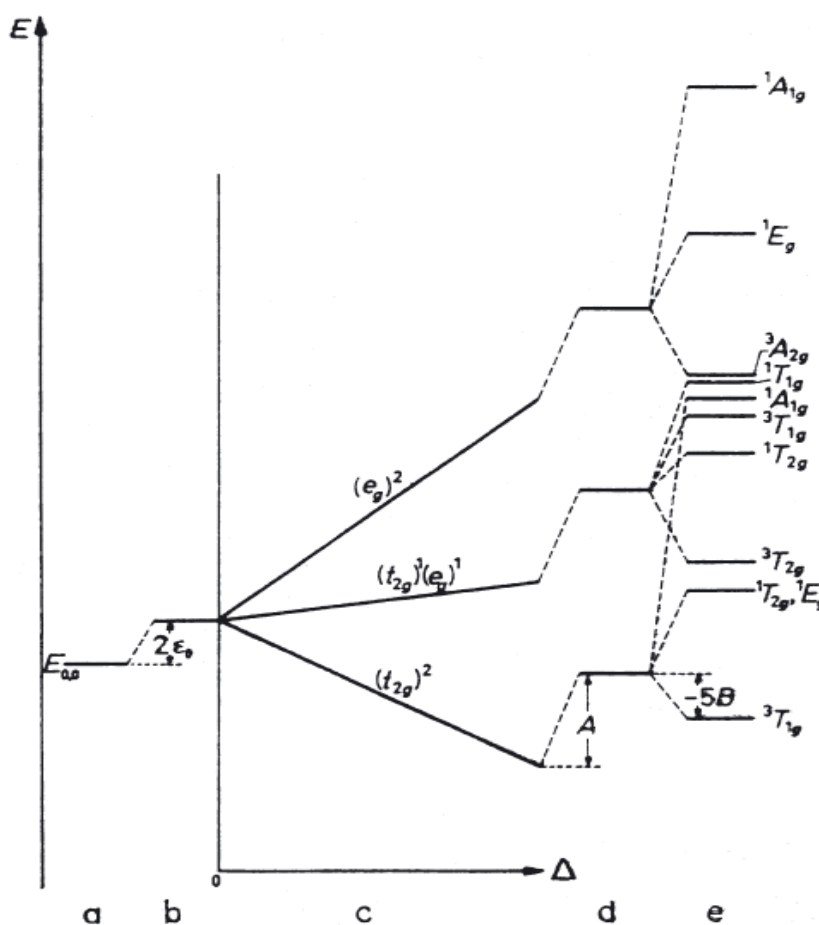


Fig. 1.10 Splitting of the terms of the d^2 configuration in strong fields of octahedral symmetry [72]: (a) d -electron energy level; (b) ligand field destabilization; (c) ligand field splitting as a function of Δ ; (d) electron interaction destabilization; (e) electron interaction splitting.

Table 1.3 gives the electronic configurations and the ground state terms for all atomic configurations d^n in strong octahedral and tetrahedral ligand fields. By comparison with the corresponding cases of weak fields, one can see that differences occur for $n = 4, 5, 6, 7$ in octahedral symmetry, and for $n = 3, 4, 5, 6$ in tetrahedral systems. It is important that in these cases the spin multiplicity of the ground state is always lower in the strong-field limit than in the weak field. Therefore, the complexes with strong ligand fields are called *low-spin*

complexes, as distinct from complexes with weak ligand fields, which are *high-spin complexes*. One consequence of this result is the statement that, depending on the ligand properties (ligand field strength), there may be complexes of the same metal in the same oxidation state with two different kinds of spin multiplicity of the ground state (and hence different magnetic properties).

Table 1.3 Electronic configuration and ground-state terms of octahedral and tetrahedral complexes in the case of strong ligand fields

Number of d Electrons	Octahedral Complex		Tetrahedral Complex	
	Electronic Configuration	Ground-State Term	Electronic Configuration	Ground-State Term
d^1	t_{2g}	${}^2T_{2g}$	e	2E
d^2	$(t_{2g})^2$	${}^3T_{1g}$	$(e)^2$	3A_2
d^3	$(t_{2g})^3$	${}^4A_{2g}$	$(e)^3$	2E
d^4	$(t_{2g})^4$	${}^3T_{1g}$	$(e)^4$	1A_1
d^5	$(t_{2g})^5$	${}^2T_{2g}$	$(e)^4 t_2$	2T_2
d^6	$(t_{2g})^6$	${}^1A_{1g}$	$(e)^4 (t_2)^2$	3T_1
d^7	$(t_{2g})^6 e_g$	2E_g	$(e)^4 (t_2)^3$	4A_2
d^8	$(t_{2g})^6 (e_g)^2$	${}^3A_{2g}$	$(e)^4 (t_2)^4$	2T_1
d^9	$(t_{2g})^6 (e_g)^3$	2E_g	$(e)^4 (t_2)^5$	2T_2
d^{10}	$(t_{2g})^6 (e_g)^4$	${}^1A_{1g}$	$(e)^4 (t_2)^6$	1A_1

The criterion of validity of the strong-field limit, similar to the weak-field case, follows from its assumptions. Since the splittings caused by the electron interactions are determined for each of the three configurations $(t_{2g})^2$, $(t_{2g})^1(e_g)^1$, and $(e_g)^2$ separately, the results are valid when the splitting is smaller than the energy gap Δ between them. For splitting of the $(t_{2g})^2$ configuration, the maximum distance between its components after (1.18) is $15B + 5C$; hence the condition of validity of the strong-field approach is $15B + 5C \ll \Delta$. Otherwise the terms of the same symmetry from different configurations become strongly mixed [e.g., ${}^1T_{2g}$ from $(t_{2g})^2$ with ${}^1T_{2g}$ from $(t_{2g})^1(e_g)^1$], and it is said that there is a *configuration interaction*.

For more than two d electrons, the criterion of validity of the strong-field approximation can be established similarly. Of special interest are the cases of d^4 , d^5 , d^6 , and d^7 in octahedral complexes and d^3 , d^4 , d^5 , and d^6 in tetrahedral systems, for which the two limit cases differ by the spin of the ground state. Let us introduce the notion of *pairing energy* Π defined as the difference between the energies of multielectron interactions in low- and high-spin complexes, respectively, divided by the number of pairings destroyed by the low-spin \rightarrow high-spin transition. It is obvious that the low-spin state is preferable if:

$$\Pi < \Delta \quad (1.19)$$

On the contrary, if

$$\Pi > \Delta \quad (1.20)$$

then the high- spin state is the ground state.

1.2.7. Arbitrary ligand fields and Tanabe–Sugano diagrams

If the ligand field is of intermediate strength for which neither the weak-field nor strong-field criterion is realized, the problem should be solved with the ligand field and electron interactions considered simultaneously. For a specific system the calculations can be carried out by numerical computation. However, a general understanding (and sometimes practical results) can be obtained when starting from one of the limit cases, for which the problem can be solved analytically, with subsequent corrections on the abovementioned term interactions, or configuration interaction.

The magnitude of the splitting of terms in an arbitrary ligand field strength can be evaluated by perturbation theory considering the electron interaction and the ligand field potential V as perturbations. Fig. 1.11 shows the correlation of the terms of the $[L](nd)^2$ configuration in octahedral fields of strong, weak, and intermediate strength.

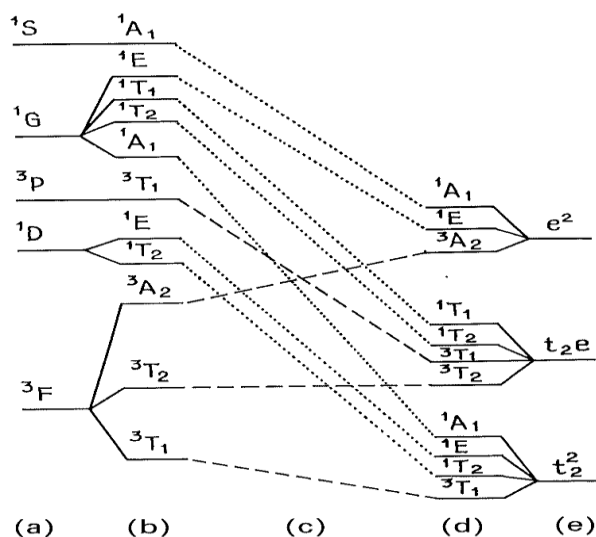


Fig. 1.11 Correlation of energy terms of electronic d^2 configuration in weak, strong, and intermediate ligand fields of octahedral symmetry[71]: (a) d levels; (b) weak field; (c) intermediary field (d) strong field and weak interelectron repulsion (e) strong field.

It follows that for an arbitrary strength of ligand fields the energy term splitting depends not only on the CFT parameter Δ but also on the initial energy spacing of the atomic terms. The latter can be defined by the three Racah parameters: A , B , and C . Parameter A determines the energy of destabilization by the average electron interaction, which is the same for all of the terms and can be excluded by an appropriate choice of the energy reference. Parameters B and C can be obtained from the empirical spectroscopic data of free atoms and

ions. Table 1.4 lists these parameters for some transition metal ions together with their ratio $\gamma = C/B$.

Table 1.4 Some numerical values for the Racah parameters B and C (in cm^{-1}) and $\gamma = C/B$ for transition metal ions M^{2+} and M^{3+} .

M^{2+}	B	C	γ	M^{3+}	B	C	γ
Ti^{2+}	695	2910	4.19	—	—	—	—
V^{2+}	755	3255	4.31	V^{3+}	862	3815	4.43
Cr^{2+}	810	3565	4.40	Cr^{3+}	918	4133	4.50
Mn^{2+}	860	3850	4.78	Mn^{3+}	965	4450	4.61
Fe^{2+}	917	4040	4.41	Fe^{3+}	1015	4800	4.73
Co^{2+}	971	449	4.63	Co^{3+}	1065	5120	4.81
Ni^{2+}	1030	4850	4.71	Ni^{3+}	1115	5450	4.89

The γ value does not differ much for different ions (for rough approximate estimations it may be assumed that $C \approx 4.5B$). Supposing that γ is known, one can reduce the number of parameters determining the relative energy-level positions to two: Δ and B . Then, by choosing the scale in B units, one obtains the energies as a function of only one parameter Δ . Energy-level diagrams as functions of the *CFT* parameter Δ for all of the d^n configurations ($n = 2,3,4,5,6,7,8$) were constructed by Tanabe and Sugano [74-75]. In those diagrams the energy read off is taken at the ground state. Therefore, for the electronic configuration d^n with $n = 4,5,6,7$ in octahedral fields ($n = 3,4,5,6$ in tetrahedral fields) at a certain value of Δ (more precisely, Δ/B), there is a term crossing, the ground state changes, and all energy levels on the diagram are subject to a break. Usually at this break the ground state multiplicity also changes, and there is a transition from the weak ligand field to the strong one. The Tanabe–Sugano diagrams give the most complete information about the electronic structure of the system in the *CFT* model. For improvements in these diagrams with respect to the spin–orbital interaction see, for instance, [50, 76].

1.2.8. Qualitative interpretation of vibrational broadening: the configurational coordinate diagram

Electronic spectra result from electronic transitions between two states of the system and carry information about these states. One important special feature relevant to coordination compounds is the strong dependence of electronic energies on interatomic distances. For this reason the stationary states of the system are not purely electronic but electron-vibrational. In our reference model centre AB_6 (see Fig.1.1), this means that the centre is a part of a vibrating lattice and so the environment of A is not static but dynamic. Moreover, ion A can participate in the possible collective modes of lattice vibrations. In order

to understand the dynamic effects on optical spectra, one has to consider that ion A is *coupled* to the vibrating lattice. This means that the neighbouring B ions can vibrate about some average positions and this affects the electronic states of ion A . Additionally, the environment can also be affected by changes in the electronic state of ion A . For example, when ion A changes its electronic state, the ligand B ions may adopt new average positions and the nature of their vibrations about these new average positions may not be the same as for the initial electronic state.

To take the above-mentioned ion–lattice coupling into account, the full ion-plus lattice system must be considered, so that the static Hamiltonian given by (1.2) must be replaced by

$$H = H_{\text{FI}} + H_{\text{CF}} + H_L \quad (1.21)$$

where H_L is the Hamiltonian describing the lattice (the kinetic and potential energies of the lattice) and $H_{\text{CF}} = H_{\text{CF}}(\mathbf{r}_i, \mathbf{R}_l)$ is the crystalline field Hamiltonian, which now depends on both \mathbf{r}_i (the coordinates of the valence electrons of ion A) and \mathbf{R}_l (the coordinates of the B ions). Consequently, at variance with the static case, the crystalline field term *couples* the electronic and ionic motions. In fact, the eigenfunctions are now functions of the electronic and ionic coordinates, $\psi = \psi(\mathbf{r}_i, \mathbf{R}_l)$ ($l = 1, 2, \dots, 6$ for the AB_6 centre). The solution of the Schrödinger equation, $H\psi = E\psi$, is now much more complicated and some approximations must be considered taking into account different coupling strengths. To explain this type of coupling, it is necessary to invoke the *configurational coordinate model*. The configurational coordinate model is based on two main approximations:

- The adiabatic approximation, the Franck – Condon principle. It states that ions move very slowly in comparison to valence electrons, so that the electronic motion takes place at a given nuclear coordinate (electrons move without perceiving changes in the nuclear positions).
- The second approximation is just to limit the attention to only one representative (ideal) mode of vibration instead of the many possible modes. It is usual to choose the so-called *breathing mode*, in which the ligand B ions pulsate radially ‘in and out’ about the A central ion. In this case, we need only one nuclear coordinate, called the *configurational coordinate* Q , which corresponds to the distance A – B . However, it is known that there is a large number of vibrational modes in a crystal. Thus, in general, the configurational coordinate can represent the average amplitude of one of these modes or perhaps a linear combination of several of them.

The solution of the Schrödinger equation of our one-coordinate dynamic centre [77] leads to potential energy curves for the ground i (initial) and excited f (final) states as diagrammatically represented in Fig. 1.12.

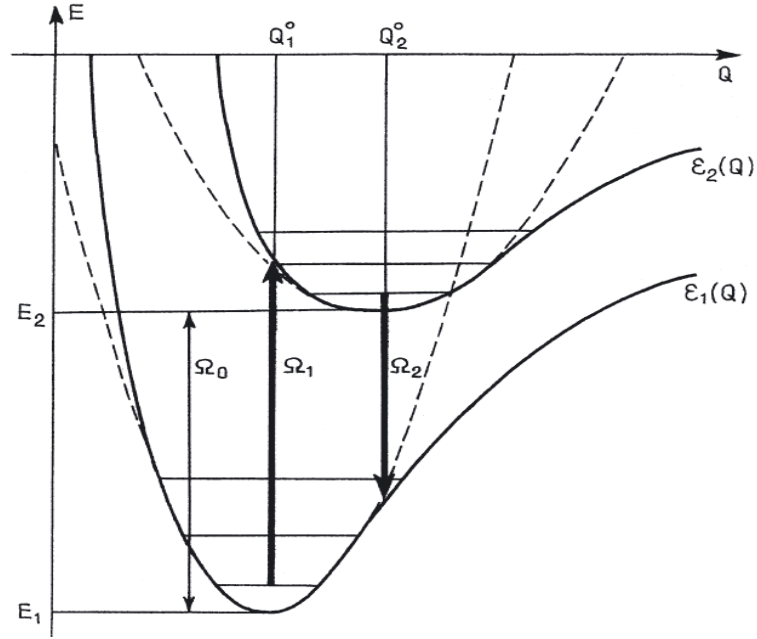


Fig. 1.12 Configurational coordinate diagram for the AB_6 centre oscillating as a breathing mode [72]. Broken curves are parabolas within the approximation of the harmonic oscillator. Horizontal full lines are phonon states.

Such a diagram is called a *configurational coordinate diagram*. The curves in the diagram represent the interionic interaction potential energy (the Morse potential), while the horizontal lines over each curve represent the set of permitted discrete energies (phonon states). It must be noted that the equilibrium position coordinates, Q_1 and Q_2 , are different for the ground and excited states; and also that, at distances close to the equilibrium coordinate, the interionic potential curves can be approximated by parabolas (broken curves) according to the harmonic oscillator approximation. In this approximation, B ions pulsate in harmonic oscillation around the equilibrium positions and, consequently, the interionic potential energies, $E_i(Q)$ and $E_f(Q)$, of the ground and excited states are given by

$$\begin{aligned}
 E_i(Q) &= E_1 + \frac{1}{2} M \Omega_i^2 (Q - Q_1)^2 \\
 E_f(Q) &= E_2 + \frac{1}{2} M \Omega_f^2 (Q - Q_2)^2
 \end{aligned}
 \tag{1.22}$$

where M is an effective oscillating mass and Ω_i and Ω_f are characteristic vibrational frequencies for the ground and excited states, respectively. These frequencies are considered to be different, as the centre can pulsate at different frequencies in the ground and excited states. The discrete energy levels sketched as horizontal lines on each potential curve of Fig. 1.12 are consistent with the quantized energy levels (phonon levels) of a harmonic

oscillator. For each harmonic oscillator at frequency Ω , the permitted phonon energies are given by

$$E_n = \left(n + \frac{1}{2}\right)\hbar\Omega \quad (1.23)$$

where $n = 0, 1, 2, \dots$ and so on. Each of these states is described by a harmonic oscillator function $\chi_n(Q)$, and the probability of finding an electron at Q in the n th vibrational state is given by $|\chi_n(Q)|^2$. As a relevant example, in Fig. 1.13 the shapes of $|\chi_n(Q)|^2$ for the states $n = 0$ and $n = 20$ have been drawn. This reveals that for the lowest energy state the maximum amplitude probability occurs at the equilibrium position, Q_0 , while for a large n value the maximum probability occurs at the configurational coordinates Q where the corresponding vibrational energy crosses with the parabola. This has a strong influence when determining the shape functions of the spectra.

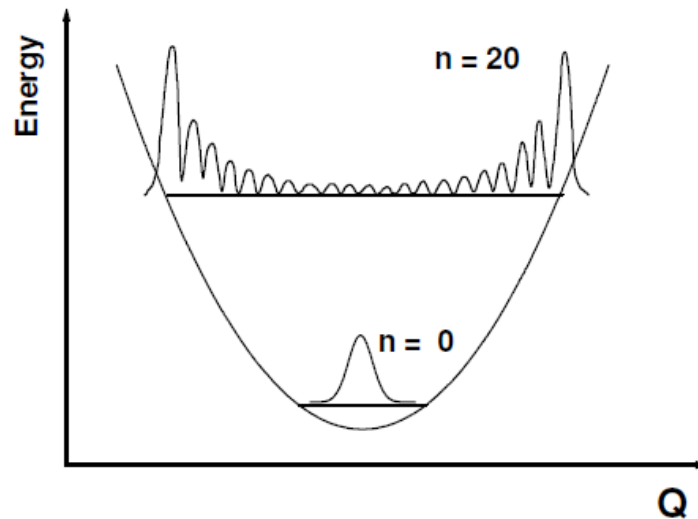


Fig. 1.13 The shape of the $|\chi_0(Q)|^2$ and $|\chi_{20}(Q)|^2$ functions for a quantum harmonic oscillator [72].

Fig. 1.14 displays the shape of the absorption (and emission) band as an envelope curve over the different $n = 0 \rightarrow m = 0, 1, 2, \dots$ ($m = 0 \rightarrow n = 0, 1, 2, \dots$) transitions. The transitions $n = 0 \leftrightarrow m = 0$ are called *zero-phonon lines*, as they occur without the participation of phonons. Thus, the zero-phonon absorption line is coincident with the zero-phonon emission line. The maximum in the absorption band occurs at the particular energy for which there is a maximum overlap factor, and it has been indicated by the arrow AB in Fig. 1.14. It corresponds to a transition from A (the equilibrium position in the ground state, $n = 0$), where the amplitude probability is maximal, to B (a cross-point in an excited level of the terminal state, f), where the amplitude probability is also a maximum. By the same reasoning, the maximum emission intensity occurs at an energy that corresponds to the arrow CD in Fig. 1.14.

As shown in this figure, the maximum in the emission peak occurs at a lower energy than the maximum in absorption, thus explaining the *Stokes shift*. The Stokes shift is an important feature, as it avoids a strong overlap between the absorption and emission bands.

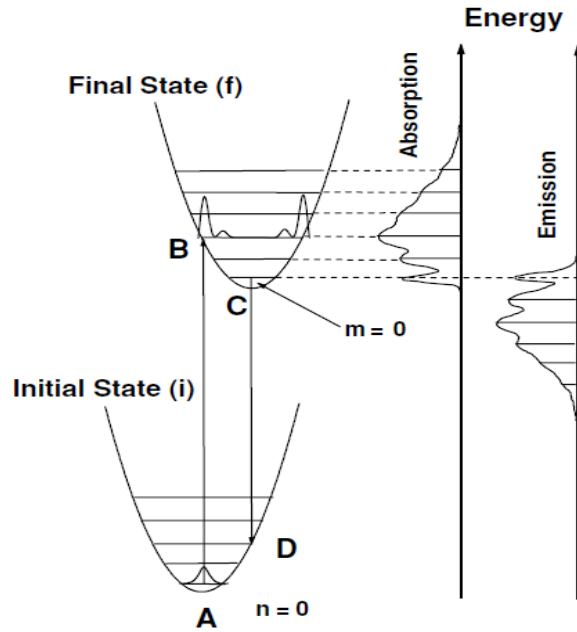


Fig. 1.14 A configurational coordinate diagram that describes the transitions between two electronic states [72]. Harmonic oscillators at the same frequency Ω are assumed for both states. The absorption and emission band profiles are sketched based on the $0 \rightarrow m$ (absorption) and $n \leftarrow 0$ (emission) relative transition probabilities (see the text). For simplicity, the minima of these parabolas, Q_1 and Q_2 , are not represented.

Otherwise, the emitted light would be reabsorbed by the emitting centre. Consequently, due to the Stokes shift the maximum of the absorption or luminescence band does not correspond to the pure electronic transition (between the $n=0$ and $m=0$) thus for according to the theory of the electronic phonons assisted transitions [72] the maximum is shifted aside the higher energies relatively to the pure electronic transition by the value

$$\Delta\hbar\omega = \frac{(\delta\Omega)^2}{16\hbar\omega_{ph} \ln 2} \quad (1.24)$$

where $\delta\Omega$ is the *full width at half maximum* (FWHM) and ω_{ph} – the phonon frequency. For the low temperature case the formula has the form

$$\Delta\hbar\omega = \frac{(\delta\Omega)^2}{\hbar\omega_{ph} \ln 2} \quad (1.25)$$

For determination of the Dq , B and C parameters with a good precision it should be taken into account this shift of the maximum of the absorption or luminescence band.

1.3 Conclusions

- Optical properties and applications of the oxide spinels and sulphide compounds depend on the presence of *optically active centres*. These centres consist of dopant ions, usually transition of rare earth metal ions that are intentionally introduced into the crystal during the growth process. The optical properties of the oxide spinels doped by transition or rare earth metal ions have been mainly investigated due to their advantages over ruby in that its cubic crystal structure provided optical isotropy.
- Unlike the crystals containing trivalent chromium, systems based on other TM ions are not easy to deal with; ions like Ti, Co and V, have a strong tendency to form mixed valence systems. Some of the theoretical difficulties concerning the interpretation of the spectroscopic data are connected with the crystal structure of the spinels, described by general formula $A^{2+}B_2^{3+}X_4^{2-}$. Due to the presence of the two possible sites for the cations, the octahedral and tetrahedral sites for A and B cations respectively, it turns out that a wide range of divalent ions may be substituted for A^{2+} , and almost any trivalent ions for B_2^{3+} . One of the problems associated with crystal structure determination concerns the random distribution of metal ions between the interstitial A and B sites.
- In contrast to the wide range of applications which have developed for the oxide spinels, much less has been done to utilize the properties of the analogous sulphide and selenide materials. Although an enormous amount of research has been devoted in the last decade to the study of the magnetic properties of sulphide spinels so that it is really known quite a lot now about their properties, it is surprising to find that there are practically no papers investigating the spectroscopic properties of sulphide spinels, in particular α -ZnAl₂S₄ single crystals, that constitutes the main object in the present thesis.
- In spite of a few spectroscopic studies of the optical properties of the undoped and chromium doped α -ZnAl₂S₄, still the understanding of many optical phenomena in α -ZnAl₂S₄ doped by transition metal ions is rather poor. Moreover, the crystal field strength of the sulphide spinels, according to the spectrochemical series, is weaker compared to that of the oxide spinels, which should lead to the shift of the radiative spectra to the near infrared, a region of interest that is used in the fibre-optics communication systems..

2. CRYSTAL GROWTH, STRUCTURAL CHARACTERISATION AND EQUIPMENT FOR MEASUREMENT OF OPTICAL PROPERTIES

2.1. Introduction

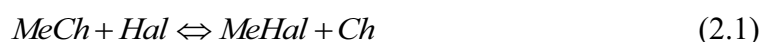
It has been known for many years that solid materials, crystalline or amorphous, may be transported by sublimation through the vapour phase under the influence of a temperature gradient. Such "direct" vapour transport has been used for the growing of crystals and, under high vacuum conditions, the deposition of films. The virtual indifference of the vapour pressure of a substance to any outside influence except temperature, however, has placed many chemical systems beyond the reach of the research worker and has rendered many others difficult to handle. Crystal growth from the melt by the classical methods of Kyropoulos and Bridgman is exceedingly difficult if applied to materials having high melting point. There may be additional difficulties if compounds are to be grown which show appreciable dissociation at the melting point or only under elevated pressure. To obtain single crystals of such materials usually phase methods are used. The polycrystalline volatile starting material is sublimed either in vacuum or in a stream of a carrier gas or the vapours of its constituents are reacted in a crystallization chamber. The temperatures required for these processes are high – in the vicinity of the sublimation point - and they have to be closely controlled in order to avoid polynucleation by surpassing a small super saturation range. This can be achieved by utilizing the concept of chemical transport reaction, the term first introduced by Schäfer [78]. Instead of vaporizing a solid directly at high temperatures it may be vaporized at much lower temperatures by forming highly volatile chemical intermediates and reacting back resulting gas mixture at a different temperature utilizing the temperature dependence of the equilibrium involved.

A chemical vapour transport reaction describes a process for purification and crystallization of non-volatile solids. The technique entails the reversible conversion of non-volatile elements and chemical compounds into volatile derivatives. The volatile derivative migrates throughout a sealed reactor, typically a sealed, evacuated glass tube heated in a tube furnace. Elsewhere in the tube where the temperature is held at different values, the volatile derivative reverts to the parent solid and the transport agent is released. The transport agent is thus catalytic. The technique requires that the two ends of the tube containing the sample to be crystallized, be maintained at different temperatures. For this purpose two-zone tube furnaces are employed. Transport reactions are classified according to the thermodynamics of the reaction between the solid and the transporting agent. When the reaction is exothermic, then the solid of interest is transported from the cooler end which can be quite hot of the reactor to

a hot end, where the equilibrium constant is less favourable and the crystals grow. Alternatively, when the reaction of the solid and the transport agent is endothermic, the solid is transported from a hot zone to a cooler one.

2.2. Theoretical and Experimental Aspects of the Chemical Vapour Transport (CVT) Reactions

Let us consider a closed system containing $n+1$ components all of which are in chemical equilibrium with each other. The temperature is chosen such that only one component is solid, the other n components are gaseous. If there is a local perturbation of the chemical equilibrium such that the solid component will have a smaller free energy at the perturbed area, it would migrate via the gas phase to this area until equilibrium is established again. The simplest way to bring about such a perturbation is a local change in temperature, that is, imposing a temperature gradient on the system. For $n = 1$ the trivial case of sublimation of a solid via its gaseous atoms or molecules results. In the following, the case $n = 3$ is considered which applies to the transport of metal chalcogenides by halogens. The equilibria involved are:



a specific example is $ZnS + I_2 \rightleftharpoons ZnI_2 + 1/2S_2$. The simplest experimental arrangement for a transport experiment is a closed horizontal tube. One end, the vaporization chamber, contains some polycrystalline feed material and a small amount of iodine, the transporter. If the vaporization chamber is held at higher temperature and the other end, the crystallization chamber, at lower temperature, the components will be transported via the vapour phase and deposit in crystals in the crystallization chamber because of the temperature dependence of the above equilibrium. Tiny amounts of the transporter are sufficient to transport practically unlimited amounts of the solid, because the transporter set free during crystallization diffuses back to pick up more solid, etc. The results of a transport reaction can be characterized by the quantity m , i.e. the amount of material transported per unit time from the vaporization chamber to the crystallization one. The amount of material transported m should not exceed a certain maximum value because otherwise the growing seeds cannot digest the arriving materials and supersaturation will increase until additional nucleation takes place.

To understand which parameters govern such a transport reaction and whether it is possible to make predictions of what kind of a transporter will yield optimal transport in a given system, the following considerations should be taken into account. The amount of material transported m can be written as the product of two functions, Δp and L . The function Δp characterizes the “chemical potential difference” between the vaporization and crystallization chambers and is proportional to the difference in vapour pressure of the

transporter in the two chambers, also Δp is a function of the “chemical parameters” of the system: the temperature T_1 of the vaporization chamber, the temperature T_2 of the crystallization chamber, the change in free energy ΔG for the reaction involved and the concentration of the transporter c_T :

$$\Delta p = f(T_1, T_2, \Delta G, c_T) \quad (2.2)$$

The function L characterizes the “conductance” of the system in respect to the vapour transport between the two chambers and is a function of the “geometrical parameters” of the system: the length l of the tube, its cross-section q and a “specific conductance” σ , which characterizes the physical nature of the transport mechanism: diffusion, convection or laminar flow. Thus

$$m = \Delta p(T_1, T_2, \Delta G, c_T) * L(l, q, \sigma) \quad (2.3)$$

To predict m for a chosen system it is thus necessary to derive the functions Δp and L explicitly; m can be controlled by Δp (variation of $\Delta T = T_2 - T_1$) as well as by L (the geometry of the system).

To derive Δp it is necessary to know the types of reactions taking place in the transport process and their free energy changes in the operating temperature range. By forming an expression as

$$\Delta G = \Delta H - T\Delta S = -RT \ln K \quad (2.4)$$

at the two temperatures T_1 and T_2 and observing the conditions imposed by c_T on the partial pressures of the components occurring in the explicit expression for K , one can solve Δp . However, there is another way to get important information if only the sign of the heat of reaction ΔH is known, because the expression

$$d \ln \frac{K}{dT} = \frac{\Delta H}{RT^2} \quad (2.5)$$

indicates whether transport is to be expected from hot to cold, or vice versa. Unlike ordinary sublimation, not all reactions transport from hot to cold. Only if $\Delta H > 0$, i.e. for endothermic reactions where K increases with temperature, the transport is from hot to cold. If $\Delta H < 0$, the reaction will transport from cold to hot. The theoretical interpretation of these aspects can be found in [78-79]. **However, transport of metal chalcogenides with iodine as transporter occurs always from hot to cold.** A good qualitative connection between Δp and ΔG is gained by the method described in [78] where Δp vs. ΔH curves, with the entropy change ΔS as parameter, are plotted. Such curves are particularly useful for estimating the relative magnitude of m for various substances transported by the same mechanism. The essential conclusion is that transport can occur only if K is of the order of unity, i.e. if the equilibrium is not extreme.

- The role of the transporter. Studies on the transport effect of different transporters have revealed that the most suitable one is iodine. Bromine gave much smaller m values and chlorine showed practically no transport at all. This is in qualitative agreement with an estimate of the ΔG values at room temperatures from literature data. The latter showed that the iodine reaction had the lowest ΔG value and thus the least extreme equilibrium position as required for a reasonable transport effect.

- The role of c_T . The increase of c_T on m is stronger than linear, with c_T up to a value of 15 mg I/cm³ which should not be exceeded for safety reasons. A strong dependence of the size and the quality of the resulting crystals on c_T was noted in [2-3]. At $c_T = 1$ mg I/cm³ the growth is very slow. Best results were obtained at $c_T = 5$ mg I/cm³. At higher iodine concentrations, e.g. $c_T = 15$ mg I/cm³, the amount of material transported is so large that polynucleation can occur.

- The role of T_1 and T_2 . The absolute values of these temperatures can vary over a relatively wide range if to consider only m and not the quality of the crystals. The range of permissible supersaturation, however, decreases with temperature. The difference ΔT between T_1 and T_2 was found to be of minor importance since at the geometry employed the “conductance” L rather than the partial pressure difference Δp appeared to be the rate determining step in the growth process. The optimal growth temperature T_2 has to be evaluated empirically for a given substance. Besides, the proper choice of T_2 depends on the physical properties required from the crystal such as the amount of transporter dissolved in the crystal, the number of imperfections, etc.

It is much more difficult to derive an explicit expression for L because transport of vapor can be affected in three ways.

1. By diffusion between the two chambers, if narrow tubes are used, and if the total pressure in the system is small. However, transport only by diffusion is slow and all of the experiments described below were well in the pressure range (of the order of 1 atm.) above pure diffusion.

2. By convection. This takes place at higher pressures, in wider tubes, and in tubes inclined against the horizontal.

3. By laminar flow, if the reaction involves a change in mole numbers, and if the reaction velocity on both sides is high enough to maintain a constant pressure difference.

Which mechanism prevails depends largely on the transporter concentration c_T determining the total pressure, and on the geometry of the system. Since there is usually an overlap between several of these mechanisms and the exact temperature distribution along the tube plays its role, it is difficult to arrive at an analytical expression for L .

- The role of m . The decrease of m is approximately linear with the tube length l because of the increase in flow resistance. However, to use very short tubes is not quite correct since the crystallization chamber should not be too small in order to avoid intergrowth between crystals. A good compromise between these requirements is to heat the tube not symmetrically but asymmetrically in such a way that the vaporization chamber is small but the crystallization chamber is large. The temperature distribution in the crystallization chamber should be as uniform as possible in order to avoid re-evaporation of crystals from warmer parts in the course of an experiment. For orientating experiments, on the other hand, it is quite useful to have a sloping temperature distribution along the crystallization chamber in order to find the temperature for the optimal crystal growth. The temperature drop between the two chambers should not be too abrupt in order to avoid a clogging up of the tube in this region.

- The role of σ . The most important geometrical parameter is the tube cross section σ which influences m decisively: the larger is σ the higher is m . This large influence of σ on m is probably due to the relative decrease of the friction of the moving gases along the walls of the tube and to a partial transition from diffusion to convection, with increasing σ . The latter is also substantiated by the fact that in large diameter tubes the crystals are always found at the bottom of the tube (according to the direction of the gas flow) whereas in smaller tubes they are found all around the circumference of the tube.

Concluding, the following requirements have to be fulfilled if transport reactions are to be used for the growth of single crystals.

1. The rate of transporting m is not to exceed the rate of growing seeds.
2. The optimal crystallization temperature has to be evaluated empirically for each system taking into account the possibility of polymorphism.
3. The crystallization chamber should be large in order to prevent intergrowth between adjacent seeds. Asymmetric heating is useful.
4. The temperature distribution in the crystallization chamber should be as uniform as possible to avoid partial re-evaporation of already grown crystals.
5. Well developed crystals form easier in large diameter tubes where convection determines the rate of transport.
6. The temperature difference between the two chambers can be made smaller if wider tubes are used (thus facilitating an even temperature distribution along the crystallization chamber) since the gas flow is here the rate determining step.

2.3. Synthesis and structural characterization of α – ZnAl_2S_4 by the CVT method

It is well known that ZnAl_2S_4 crystallize in different structures, depending on the type and conditions of preparation [80-81]. In the region of temperatures 700 – 850 K there are two phases: a face-centred cubic structure denoted α - spinel phase and a hexagonal dense pack of anions, with the cations randomly distributed among one set of the possible tetrahedral sites – the W wurtzite phase. Above this temperatures, in the region between 1000 and 1200 K there are three phases: an orthorhombic phase β which was described by Steigmann [81] as an ordered version of W phase, a rhombohedral phase γ which was related by Berthold[80] as a phase related to W phase but with a longer ordering period in c direction, and a wurtzite phase.

The spinel phase of this compound is of interest from the future optical application point of view, because it is the single cubic phase from those mentioned above with a very high isotropy. The spinel phase α is described by the general formula AB_2X_4 , where A is a divalent cation in the centre of a tetrahedral coordination formed by divalent anions X, and B is a trivalent cation in the centre of an octahedral coordination, Fig. 2.1. α - ZnAl_2S_4 crystallizes in a defect cubic spinel-type crystal structure with the space group $\text{Fd}\bar{3}\text{m}$ (O_h^7), with the lattice parameter $a=10 \text{ \AA}$. Sulphur atoms form a face-centered cubic (dense-packed) sublattice with eight formula units per elementary cell. The arrangement of atoms is such that, perpendicular to each three-fold axis, layers occupied only by cations in octahedral coordination alternate with others in which the tetrahedral and octahedral sites are filled in the ratio two to one.

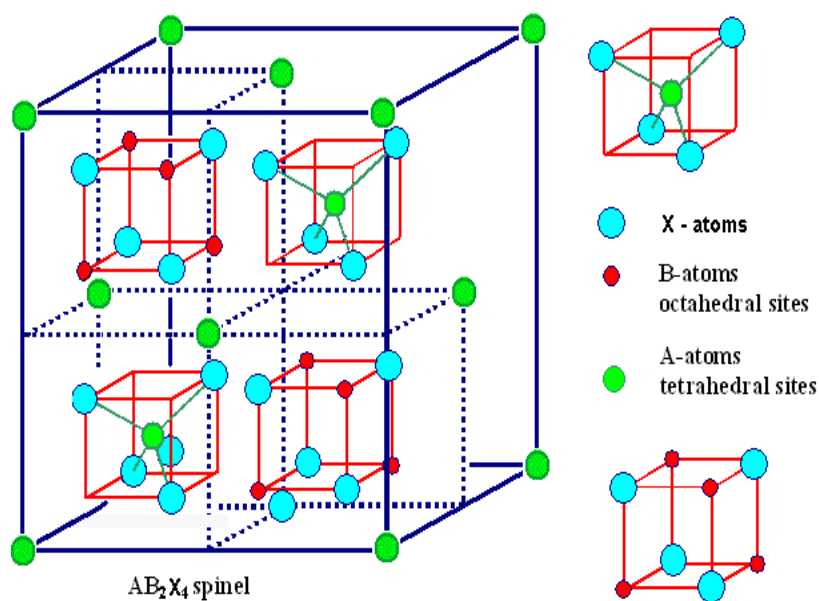


Fig. 2.1 Sulphur structure with eight face-centered cubic (dense-packed) sublattices per elementary cell

The first octant contains a Zn^{2+} ion at the center and has a tetrahedral coordination of S^{2-} ions with full T_d symmetry (A-site), and the second octant has a six-fold octahedral coordination of Al^{3+} ion belonging to the O_h point group (B-site). $ZnAl_2S_4$ has 96 cation sites, with only 24 being occupied by the cations, 8 of 64 A-sites are occupied by Zn^{2+} and 16 of 32 B-sites are occupied by Al^{3+} . In addition to a large number of unoccupied sites, on heating, Al^{3+} and Zn^{2+} ions may change their sites, giving rise to more or less random distribution of the cations, as is the case with $MgAl_2O_4$ [28]. Usually the site fraction of Al^{3+} on the Zn^{2+} sublattice (denoted i) is used as a representative of the degree of inversion. Fortunately, the studies in [80] have shown that the degree of inversion i for $\alpha - ZnAl_2S_4$ is less than 2%.

The undoped and the transitions metals Ti, Co and V doped $\alpha - ZnAl_2S_4$ single crystals were obtained by the CVT method using the Aldrich elements (purity 99,995%) Zn, Al, S, Co, V, and Ti as starting materials. The stoichiometry of the undoped compound was calculated using the following formula:

$$M_{Zn} + 2 * M_{Al} + 4 * M_S = M_{ZnAl_2S_4} \quad (2.6)$$

where M is the atomic weight of each component in part or of the entire material. If m is the amount of the material to be used in the growing process, then the amount m_x of each component x in part can be found according to:

$$m_x = \frac{M_x * m}{M_{ZnAl_2S_4}} \quad (2.7)$$

Practically the same expression is used to calculate the stoichiometry of the transition- metal doped $\alpha - ZnAl_2S_4$ compound, with the specifications as in the expression below

$$[M_{Zn} * n_{Zn}(\%) + M_y * n_y(\%)] + 2 * [M_{Al} * n_{Al}(\%) + M_y * n_y(\%)] + 4 * M_S = M_{ZnAl_2S_4} \quad (2.8)$$

$n_{Zn, Al}$ are the concentrations of metals to be substituted with the transition metal y in the n_y concentration. From equation, (2.8) it is clear that both main metals can be simultaneously partially substituted or this can be done for each of them in part. Actually, many attempts have been made to substitute only one of them taking in consideration the peculiarities of both the substituted and substituting materials. The concentration of the substituting material n_y varied between 0.05 – 0.1% at., and was not exceeded in order to avoid the creation of other defects in addition to those existing in the host lattice.

The initial material was in the same amount of 5g for all of the performed attempts and did not exceed it because of economical considerations. The starting materials were placed in evacuated sealed quartz ampoules of 8 mm inner diameter and the length which did not exceed 120 mm in order to exclude the increase of the amount of material transported per unit time m and the growing time, respectively. The ampoules were slowly heated up to the

synthesis temperature of 1000°C during two days in order to prevent the explosion and maintained in these conditions during five days. For this purpose, a one-zone tube furnace was used was inclined about 15 degrees to the horizontal, thus avoiding the transportation of the material to the other end of the ampoule. Halogen I₂ was used as transporter in the concentration of $c_T=5 \text{ mg l/cm}^3$.

After that the ampoules with the polycrystalline material were placed in a two-zone tube furnace, schematically presented in Fig. 2.2.

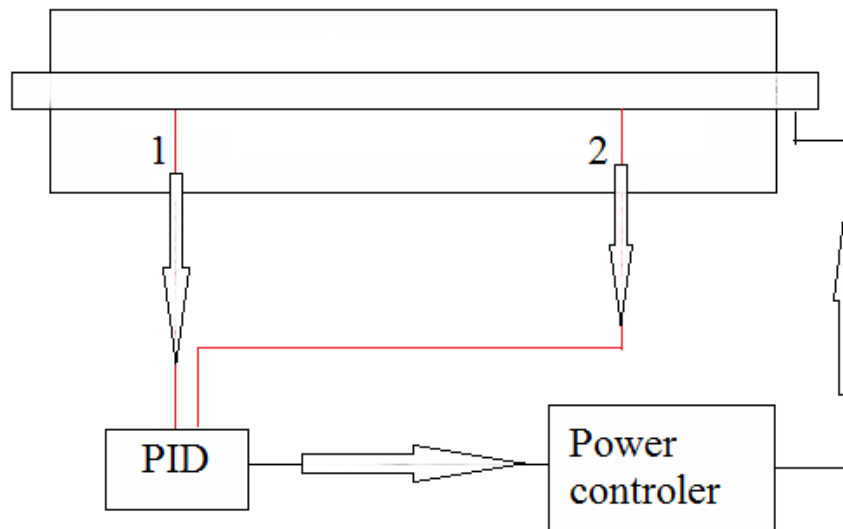


Fig. 2.2 Scheme of a dual-zone tube furnace. Inside the temperature is adjusted by the proportional–integral–derivative controller with the aid of thermocouples 1 and 2.

The temperature inside the alumina tube furnace has to be precisely controlled in order to prevent the oscillations of temperature; thus, the transport rate m is kept constant, which is very important for the quality of crystals. For the purposes of the present investigation two manually manufactured non-industrial furnaces with a $\pm 0.1^\circ\text{C}$ control precision of the temperature were used. The main parts of the furnaces, as seen in Fig. 2.2, are:

- alumina tube with two heating zones
- two thermocouples – one for each of two temperature zones, usually of type B(platinum –platinum/rhodium), are in direct contact with the alumina tube measuring the inside temperature.
- proportional–integral–derivative (PID) automatic digital controller that collects the temperature information from the thermocouples and, using a PID mathematic algorithm, adjusts the output power of the Output Power controller in order to achieve the input temperature set point.

- Output Power controller directly related with the alumina tube heating material.

The crystallisation chamber temperature was set at 750°C in the region of the spinel phase crystals growth, according to [80-81],. The temperature gradient was chosen to be as constant as possible, around the value 3.5°C/cm. A typical temperature distribution diagram is

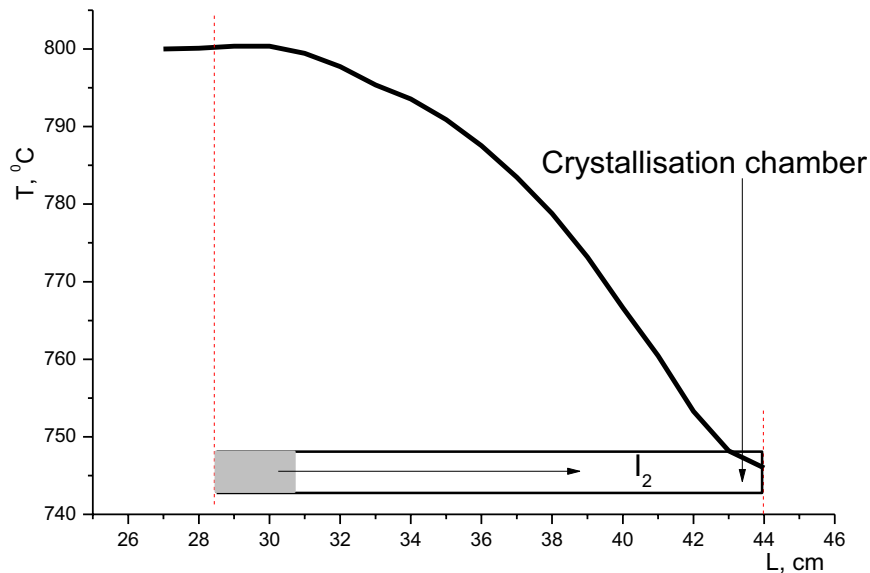


Fig. 2.3 Temperature distribution diagram in the tube furnace for growing the $ZnAl_2S_4$ spinel type single crystals

presented in Fig. 2.3. The ampoules were held in for the period of 21 days, after that they were slowly cooled until room temperature.

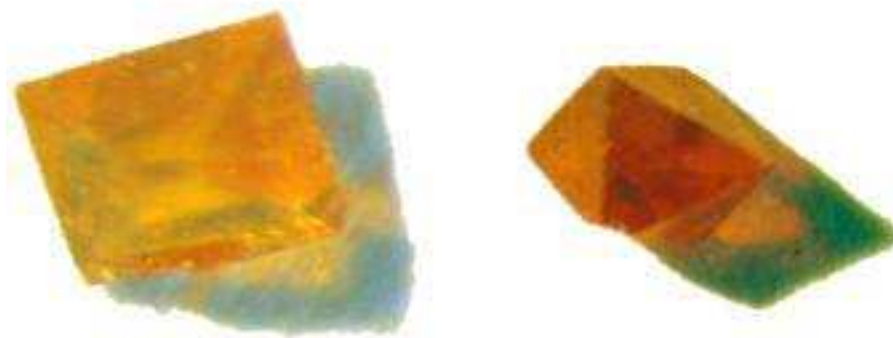


Fig. 2.4 α - $ZnAl_2S_4$ spinel type single crystals doped by vanadium – 0.05% at., grown by the chemical vapour transport method.

To sum up, the obtained undoped crystals were transparent and colourless while the palette of the doped ones was quite broad – from orange, red to completely dark depending on the type and concentration of the doping material. The intensity of colour depended on the concentration of the doping material: from slightly coloured for very low concentrations to practically dark for concentrations around 0.1% at. The crystals corresponded to optically

homogeneous octahedrons with volumes up to 20 mm³ and (111) - oriented mirror-like faces that were used directly for photoluminescence experiments, (see Fig. 2.4).

The structural characterisation was done by means of XRD, using a single crystal Oxford diffractometer, equipped with a CCD area detector and a graphite monochromator utilizing Mo K_{α} radiation. The x-ray data were collected at 200K temperature in the angle range $\theta = 0-50^{\circ}$. An example of all recorded data and different structural parameters of the undoped α - ZnAl₂S₄ are listed in Table 2.1.

Table 2.1 X-ray diffraction data of the undoped α - ZnAl₂S₄

<i>Crystal data</i>		Mo K_{α} radiation	
Al _{0.33} S _{0.67} Zn _{0.17}		Cell parameters from 0 reflections	
$M_r = 41.27$		$\theta = 0-50^{\circ}$	
Cubic, $Fd-3m$		$\mu = 6.76 \text{ mm}^{-1}$	
$a = 10.000 (5) \text{ \AA}$		$T = 200 \text{ K}$	
$V = 1000.0 (9) \text{ \AA}^3$		Block, yellow	
$Z = 48$		$0.10 \times 0.10 \times 0.10 \text{ mm}$	
$D_x = 3.289 \text{ Mg m}^{-3}$			
<i>Data collection</i>			
Area diffractometer		$R_{\text{int}} = 0.011$	
φ & ω scans		$\theta_{\text{max}} = 40.6^{\circ}$	
Absorption correction: none		$h = 1 \rightarrow 18$	
$T_{\text{min}} = 0.509, T_{\text{max}} = 0.509$		$k = 0 \rightarrow 12$	
292 measured reflections		$l = 0 \rightarrow 11$	
173 independent reflections		0 standard reflections	
172 reflections with $I > 2.0\sigma(I)$		every . reflections	
<i>Refinement</i>			
$R[F^2 > 2\sigma(F^2)] = 0.015$		$(\Delta/\sigma)_{\text{max}} < 0.0001$	
$wR(F^2) = 0.012$		$\Delta\rho_{\text{max}} = 0.53 \text{ e \AA}^{-1}$	
$S = 1.02$		$\Delta\rho_{\text{min}} = -0.51 \text{ e \AA}^{-1}$	
172 reflections		Extinction correction: Equation 22	
8 parameters		Extinction coefficient: 46 (4)	
<i>Geometric parameters (Å, °) for 1</i>			
Zn1—S3 ⁱ	2.3299 (7)	Al2—S3 ^v	2.4086 (12)
Zn1—S3 ⁱⁱ	2.3299 (7)	Al2—S3 ^{vi}	2.4086 (12)
Zn1—S3 ⁱⁱⁱ	2.3299 (7)	Al2—S3	2.4086 (12)
Al2—S3 ^{iv}	2.4086 (12)		

According to these data, the stoichiometry of the compound under study here is slightly distorted against the initial composition: Zn and S are slightly above whereas the Al is slightly below it. All other parameters are in good agreement with the calculated data for the spinel type structure. The space group, cell parameter a and cell volume have been found to be the same as in earlier works by different authors [7, 80-81]. Taking into account the similitude between the data and knowing that to determine the degree of inversion of the spinel structure more complicated analyses are required (which goes beyond the scope of this investigation), the degree of inversion for α -ZnAl₂S₄ has been taken from [7] and according to those authors it is less than 2%. The Chebychev polynomial has been used during the calculation process. A typical pattern diffraction data for α -ZnAl₂S₄ is presented in Fig. 2.5.

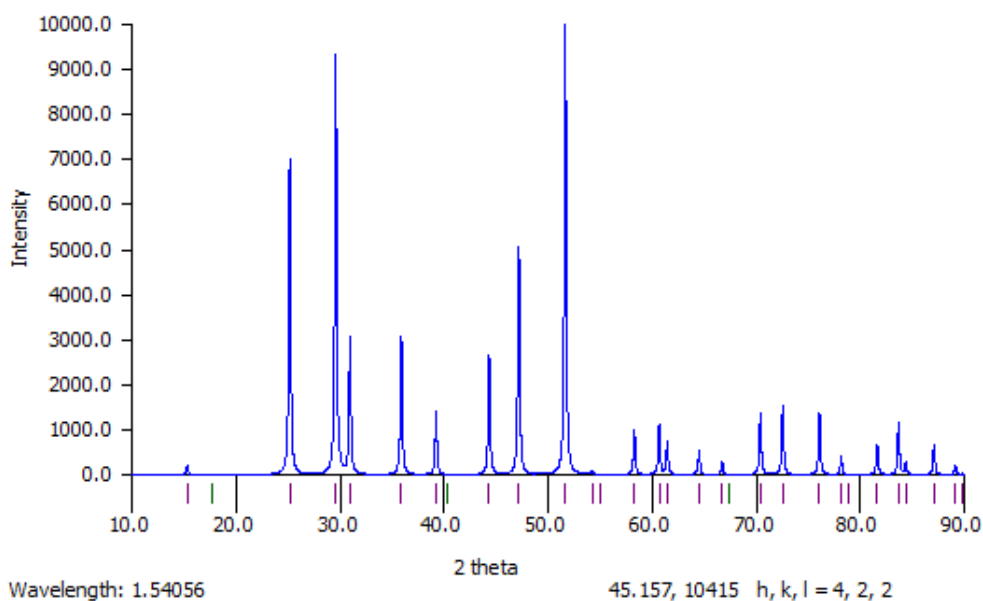


Fig. 2.5 XRD patterns of α -ZnAl₂S₄ spinel type single crystals

Thus, the x-ray analyses confirmed that all samples crystallised into the normal spinel type structure.

2.4. Measurements of absorption spectra

The main purpose of absorption measurements is to set the energy level scheme and to identify particular levels that may be convenient to “pump” the system so as to obtain luminescence or laser emission. The conventional absorption measurements are related to transitions originating in the ground state of the material. Absorption spectra are usually registered by instruments known as *spectrophotometers*. Fig. 2.6a shows a schematic diagram of the simplest spectrophotometer (*a single-beam spectrophotometer*). It consists of the following main elements:

- a light source (usually a deuterium lamp for the UV spectral range and a tungsten lamp for the VIS and IR spectral ranges) that is focused on the entrance to
- a monochromator used to select a single frequency (wavelength) from all of those provided by the lamp source and to scan over a desired frequency range;
- a sample holder, followed by
- a light detector (usually a photomultiplier for the UV–VIS range and a SPb cell for the IR range) to measure the intensity of each monochromatic beam after traversing the sample; and finally
- a computer, to display and record the absorption spectrum.

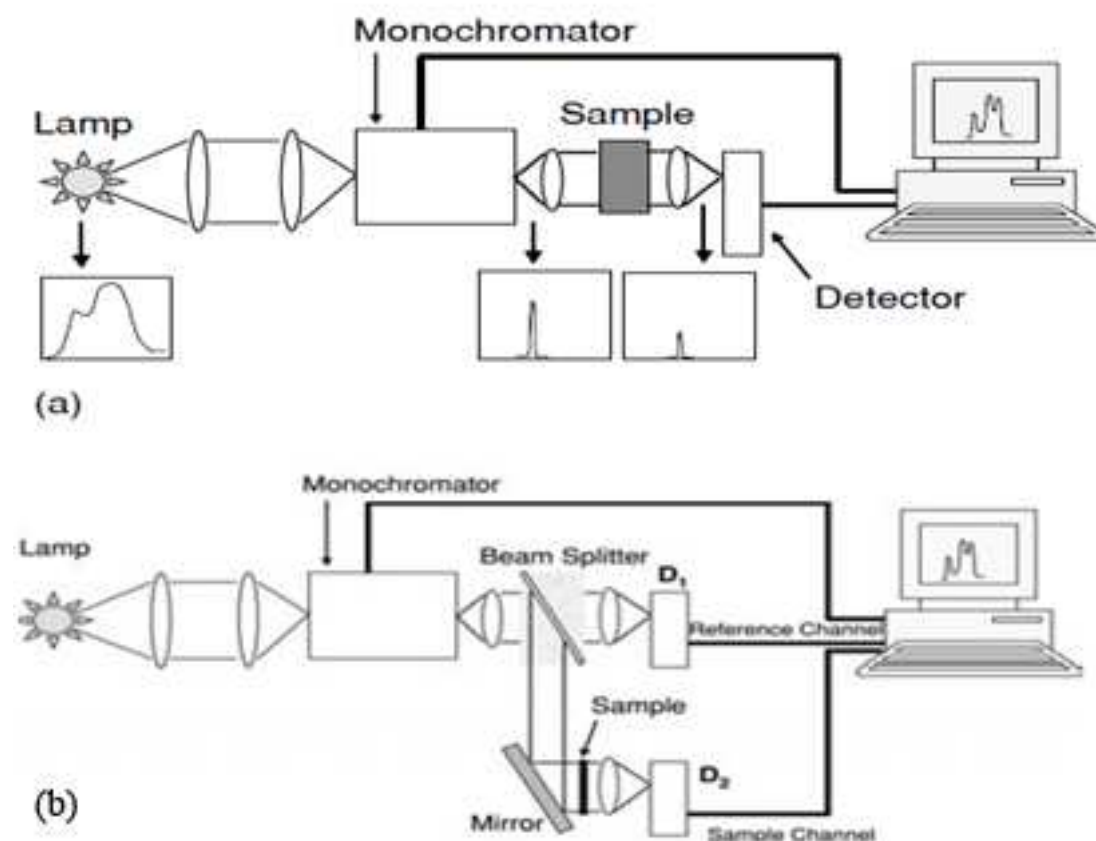


Fig. 2.6 Schematic diagrams of (a) a single-beam spectrophotometer and (b) a double beam spectrophotometer.

However, a single-beam spectrophotometer, as the one shown in Fig. 2.6a, presents a variety of problems, because the spectra are affected by spectral and temporal variations in the illumination intensity. Spectral variations are due to the combined effects of the lamp spectrum and the monochromator response, while the temporal variations occur because of lamp stability. To reduce these effects, *double-beam spectrophotometers* are used. Fig. 2.6b shows a schematic diagram of the main components of such a spectrophotometer. The illuminating beam is split into two beams of equal intensity, which are directed toward two different channels: a reference channel and a sample channel. The outgoing intensities

correspond respectively to I_0 and I , which are detected by two similar detectors, D_1 and D_2 . As a consequence, the spectral and temporal intensity variations of the illuminating beam affect both the reference and sample beams in the same manner, and these effects are minimized in the resulting absorption spectrum. The system can still be improved if a unique detector is used instead of the two detectors, D_1 and D_2 . In such a way, the errors introduced by the usual inexactly equal spectral responses of these detectors are also eliminated. This can be achieved by introducing fast rotating mirrors so that the intensities I_0 and I can be always sent to the same detector. Typical sensitivities of *optical density* $\rho_{\min} \approx 5 \times 10^{-3}$ can be reached with these spectrophotometers. The optical absorption spectra for both undoped and transition – metal (TM) doped α -ZnAl₂S₄ were recorded at room temperature using a Perkin Elmer Lambda 900 spectrometer in the wavelength range of 300 – 2000nm.

Optical spectrophotometers work in different modes to measure *optical density*, *absorbance*, or *transmittance*. The light beam is attenuated after passing the sample, according to the *Lambert–Beer law* [82]:

$$I(\lambda) = I(0) \cdot e^{-\alpha x} \quad (2.9)$$

which gives an exponential attenuation relating the incoming light intensity I_0 (the incident intensity minus the reflection losses at the surface) to the thickness x . The *optical density* is defined as

$$\rho(\lambda) = \log_{10} \frac{I_0(\lambda)}{I_T(\lambda)} \quad (2.10)$$

so that according to (2.9) the absorption coefficient is determined by

$$\alpha(\lambda) = \frac{\rho(\lambda) \cdot \ln 10}{x} \quad (2.11)$$

However, in order to exclude the effect of reflections of the surface of the sample the spectra should be registered for two samples with different thickness x_1 and x_2 . Thus, for the absorption coefficient the following relations can be written down as follows:

$$\begin{aligned} I_{T_1}(\lambda) &= I_0(\lambda) \cdot \exp[-\alpha(\lambda) \cdot x_1]; \\ I_{T_2}(\lambda) &= I_0(\lambda) \cdot \exp[-\alpha(\lambda) \cdot x_2]; \\ I_{T_1}(\lambda) / I_{T_2}(\lambda) &= \exp[-\alpha(\lambda) \cdot (x_1 - x_2)]; \\ \ln [I_{T_2}(\lambda) / I_{T_1}(\lambda)] &= \alpha(\lambda) \cdot (x_1 - x_2); \\ \alpha(\lambda) &= \ln [I_{T_2}(\lambda) / I_{T_1}(\lambda)] / (x_1 - x_2). \end{aligned} \quad (2.12)$$

The last expression in Equation (2.12) contains the term $\ln\left[I_{T_2}(\lambda)/I_{T_1}(\lambda)\right]$ that can be determined directly from the optical density or from the transmission spectra. According to (2.10), the optical density for two samples with different thickness can be written down as:

$$\rho_1 = \log_{10}\left(\frac{I_0}{I_{T_1}}\right) \qquad \rho_2 = \log_{10}\left(\frac{I_0}{I_{T_2}}\right)$$

$$\rho_1 - \rho_2 = \log_{10}\left(\frac{I_0}{I_{T_1}}\right) - \log_{10}\left(\frac{I_0}{I_{T_2}}\right) = \log_{10}\left(\frac{I_0}{I_{T_1}} * \frac{I_{T_2}}{I_0}\right) = \log_{10} \frac{I_{T_2}}{I_{T_1}} \quad (2.13)$$

$$\begin{cases} \log_{10}\left(\frac{I_{T_2}}{I_{T_1}}\right) = \ln\left(\frac{I_{T_2}}{I_{T_1}}\right) / \ln 10 \\ (\rho_1 - \rho_2) = \log_{10} \frac{I_{T_2}}{I_{T_1}} \end{cases} \Leftrightarrow \ln\left(\frac{I_{T_2}}{I_{T_1}}\right) = \ln 10 * (\rho_1 - \rho_2)$$

Thus by introducing the result for $\ln\left[I_{T_2}(\lambda)/I_{T_1}(\lambda)\right]$ in the expression for the absorption coefficient from (2.12), the latter can be determined in two ways, as follows:

1. from the optical density spectra

$$\alpha(\lambda) = \frac{\ln 10 * (\rho_1 - \rho_2)}{(x_1 - x_2)} \quad (2.14)$$

2. from the transmission spectra

$$\alpha(\lambda) = \frac{\ln\left[\frac{I_{T_2}(\lambda)}{I_{T_1}(\lambda)}\right]}{(x_1 - x_2)} \quad (2.15)$$

Nevertheless, it is important to emphasize here the advantage of measuring optical density spectra over transmittance or absorbance spectra. Optical density spectra are more sensitive, as they provide a higher contrast than absorbance or transmittance spectra.

2.5. Measurements of radiative properties

The luminescence spectra are measured to identify the luminescent states. They may also help to establish energy levels, especially the position of the ground state multiplets. The changes of spectra with temperature provide information regarding such temperature time-dependent processes as thermal line broadening and thermal change of line positions. The dependence of the spectral intensity on the concentration of luminescent centres may provide information on the threshold of quenching and on up-conversion. The step preceding the emission of luminescence is an excitation process that is aimed at populating the luminescent level(s).

The steady-state photoluminescence (*PL*) spectrum is obtained by registering the emitted light from a sample excited by an appropriate excitation source of constant energy. *Photoluminescence* occurs after excitation with light, i.e. radiation within the optical range. The spectrum is obtained using a monochromator equipped with an appropriate light detector (Fig. 2.7).

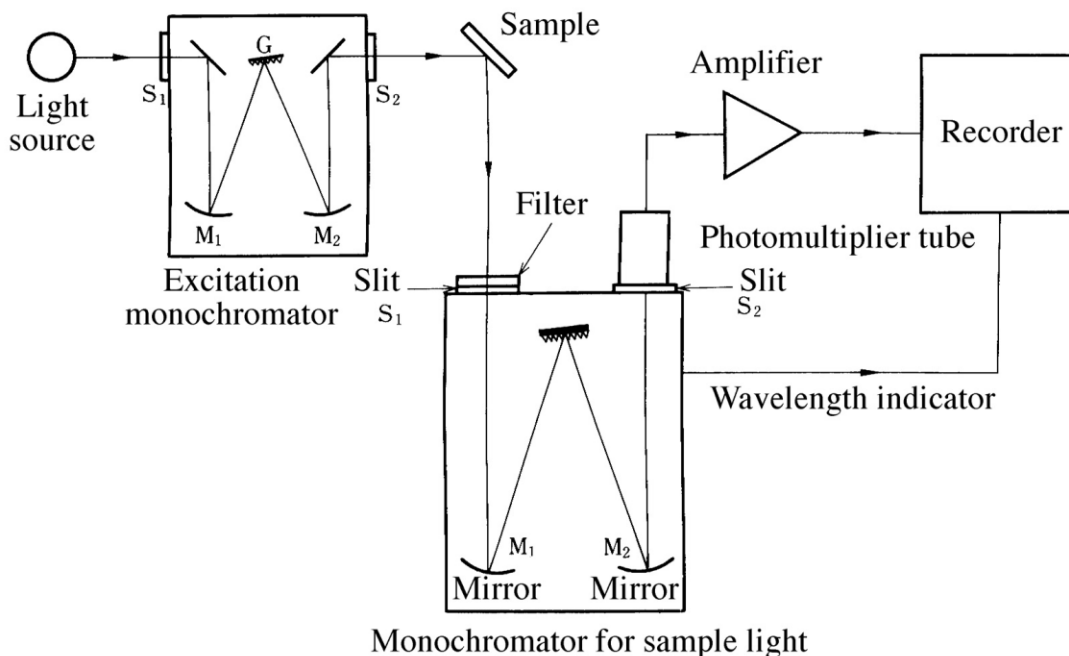


Fig. 2.7 Experimental set-up for spectroscopic investigations.

This excitation may be achieved by lamps or lasers. Selective excitation may be achieved by filtering the light of a lamp using a monochromator. However, lasers have become common in spectroscopy laboratories; they provide high light intensity in a very narrow spectral band. The exciting light sources can be continuous or pulsed. For the PL spectra the beam of the second harmonic of a *cw*-operating YAG: Nd ($\lambda = 532\text{nm}$) is chopped and the signal from the photomultiplier PMT-62 or from the InGaAs detector is sent to a lock-in amplifier before being recorded. The lock-in amplifier is tuned at the chopping frequency and selects out signals only at this frequency coming from the detector, reducing considerably the presence of noise. The samples are placed in a closed cycle cryostat and the PL spectra are registered in a broad temperature range: 10 – 300 K.

The photomultiplier tube was used for detecting UV and visible light. A photomultiplier tube having the appropriate spectral sensitivity for the wavelength region of interest was chosen. The following precautions must be taken when handling a photomultiplier tube:

1. Even when voltage is not applied to the tube, the tube should not be exposed to light.
2. A few hours prior to measurement, voltage should be applied to the tube in the dark to stabilize the output.

3. Tubes must be operated under the manufacturer's specified conditions. Particularly, the anode current must not exceed one tenth of the maximum allowed anode current, except during transient peaks measurements.
4. Tubes are extremely delicate and great care must be taken in their handling.

A solid-state detector was used to register the luminescent spectra in the NIR (near infrared) spectral region. The amount of the dark current of solid-state detectors can be reduced by cooling the detectors, as is the case in photomultiplier tubes. The signal-to-noise ratio of detectors can be improved by using thermoelectric devices to cool them.

The signal from the photodetector must be further processed electrically to obtain meaningful data. In order to acquire data with a good signal-to-noise ratio, a variety of techniques are usually employed. For the *look-in amplifier*, when the light signal is chopped at a certain frequency, the detector output consists of the signal and the non-signal component, alternately. The modified signal passes through a coupling capacitor and only the chopped frequency component is amplified by the synchronous amplifier. Using a reference signal generated by the chopper, the signal is phase-detected relative to the modulated signal. A phase shifter is adjusted to give a maximum output signal and a low-pass filter is adjusted for a time constant that optimizes the signal-to-noise ratio. Since only the input signal's phase is the same as that of the reference, the stray light that did not pass through the light chopper and other random electric noises is eliminated.

In a spectrum, light intensity at a given wavelength is expressed along the ordinate and the wavelength along the abscissa. Usually, the units of the ordinate are expressed in the arbitrary *units of the luminescence intensity*, however when accuracy is very important the units of the ordinate are either irradiance $E(W \cdot m^{-2})$ or number of photons $E_p(\text{photons} \cdot m^{-2})$. The units used depend on the purpose of the experiment. For energy efficiency, irradiance is employed and for quantum efficiency, photon irradiance is employed. The units of the abscissa are expressed in terms of wave number $\nu(\text{cm}^{-1})$, wavelength $\lambda(\text{nm})$ or energy $E(\text{eV})$. However, passing from a type of the abscissa units to another the correction on the photoluminescence spectra have to be done. If the luminescence intensity is expressed as function of the wave number:

$$I_\nu \approx f(\nu) \quad (2.16)$$

then the integral intensity, e.g. the total area under spectral curve is calculated as follows

$$\partial F_\nu = I_\nu \partial \nu \quad (2.17)$$

Passing to the wavelength dependence of the luminescence intensity

$$I_\lambda \approx f(\lambda) \quad (2.18)$$

the integral intensity is calculated

$$\partial F_{\lambda} = I_{\lambda} \partial \lambda \quad (2.19)$$

Obviously the integral intensity is the same in both cases

$$\begin{aligned} \partial F_{\nu} &= -\partial F_{\lambda} \\ I_{\nu} \partial \nu &= -I_{\lambda} \partial \lambda \end{aligned} \quad (2.20)$$

the sign ‘minus’ indicates that the changing in the wavelength would involve the change in energy with the reversible sign, e.g. the increase of the wavelength would lead to the decrease of the energy. Taking into account that

$$\lambda = \frac{c}{\nu} \quad \text{and} \quad \frac{\partial \nu}{\partial \lambda} = -\frac{c}{\lambda^2} \quad (2.21)$$

then

$$\begin{aligned} I_{\nu} \partial \nu &= -I_{\lambda} \partial \lambda \\ I_{\lambda} &= -I_{\nu} \frac{\partial \nu}{\partial \lambda} \\ \text{or} \\ I_{\lambda} &= I_{\nu} \frac{\lambda^2}{c} \end{aligned} \quad (2.22)$$

Thus, passing from the wave number dependency of the luminescence intensity to the wavelength dependency the PL spectra have to be multiplied by λ^2 . The same correction has to be applied when the PL spectra are transformed from the wavelength dependency to the energy dependency:

$$I_{E(eV)} = I_{\lambda} \frac{e\lambda^2}{hc} \quad (2.23)$$

where e is the electron charge, h – Planck’s constant and c – speed of light; those constants can be excluded from the multiplication. These corrections are very important, especially when the PL spectra are registered in a large spectral region. As is evident in (2.23), the PL intensity quadratically depends on the wavelength, thus the peculiarities of the spectrum that are placed in the long wavelength region are more affected by this correction.

Relevant information can be obtained under *pulsed wave excitation*. This type of excitation promotes a nonstationary density of centers N in the excited state. Pulsed excitation is generally achieved by sending a pulse of light at a selected wavelength in order to excite a particular level of the emitting center. The response of a particular emission line is monitored by filtering the luminescence emission. The detection of the response signal can be done by looking, on a scope, directly at the signal following the exciting pulse, or by using a boxcar integrator that integrates the signal over the time and by moving the time window. The boxcar is triggered at the same rate as the pulsed source. It is provided with a “time window” whose length and position with respect to the trigger pulse can be varied. The time window of the boxcar can also be moved continuously making the boxcar adapted to perform lifetime

measurements. This experimental procedure is called *time – resolved luminescence* (TRL) and may prove to be of great utility in understanding complicated emitting systems. The basic idea of this technique is to record the emission spectrum at a certain *delay time*, t , in respect to the excitation pulse and within a temporal *gate*, Δt , as is schematically shown in Fig. 2.8. Thus, for different delay times different spectral shapes are obtained.

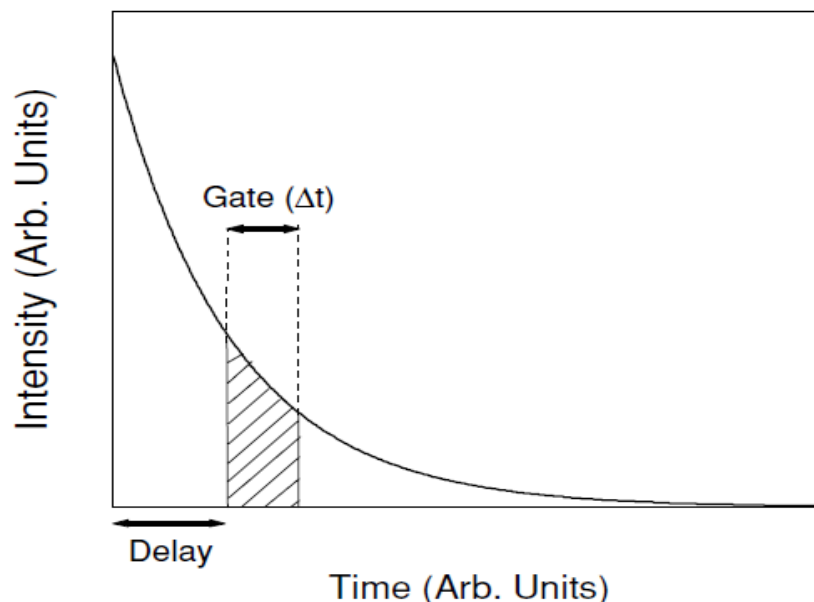


Fig. 2.8 Schematic temporal decay of luminescence, showing a gate of width Δt at delay time t_i .

It is important to mention that the experimental setup used for luminescence delay-time measurements is similar to that in Fig. 2.7, although the light source must be pulsed (alternatively, a pulsed laser can be used) and the detector must be connected to a time-sensitive system, such as an oscilloscope, a multichannel analyzer, or a boxcar integrator. For the TRL spectra the optical pulses of a tuneable YAG:Nd – Laser system *NT342B – SH/SFG* with a low repetition frequency were used and the signal was integrated with a boxcar integrator at different delay time duration and gate width.

The excitation spectra can specify in what spectral region it is necessary to pump the system in order to obtain the emission that is being monitored. Excitation spectra are essential for recognizing the presence of energy transfer among different centres, e.g. those of type X and those of type Y . Energy transfer from X to Y is present if the excitation spectrum of Y contains bands typical of X . Excitation spectra can also help in the assignment of luminescence transitions. A study of the temperature dependence of the monitored luminescence of X when pumped via the absorption bands of X and when pumped via the absorption bands of Y gives information on the role played by phonons in the energy transfer process. In order to acquire an excitation spectrum, in the present study the intensity of a specific luminescence line was monitored, with the continuous change of the wavelength of

the exciting light. This was (and is generally) achieved by putting a monochromator between a wide-spectrum source and the sample and a filter between the sample and the detector (Fig. 2.7). The detection system may use a combination of chopper/lock-in if the source is continuous, or a boxcar if the source is pulsed.

Transient properties of the luminescence of phosphor are as important as the spectra in elucidating luminescence mechanisms. By measuring transient properties, information about the lifetimes of luminescence levels and the effective nonradiative relaxation processes can be obtained. For practical applications, these measurements yield the decay of luminescence of phosphor and such information can be obtained under *pulsed wave excitation*. This type of excitation promotes a nonstationary density of centres N in the excited state. These excited centres can decay to the ground state by *radiative* (light-emitting) and *nonradiative* processes, giving decay-time intensity signal.

Assuming the radiative transition rate from a fluorescent level to the ground state is A_r , and the nonradiative transition rate between the same levels is A_{nr} , the fluorescence intensity at time t , $I(t)$, can be given by the relation:

$$\frac{dI(t)}{dt} = -(A_r + A_{nr}) * I(t) \quad (2.24)$$

Assuming the initial condition to be $I(0) = I_0$, the above equation becomes:

$$I(t) = I_0 e^{-(A_r + A_{nr}) * t} \quad (2.25)$$

Equation (2.25) corresponds to an exponential decay law for the emitted intensity, with a *lifetime* τ . The lifetime τ is defined as the inverse of the total emission probability A_T :

$$\tau = \frac{1}{A_T} \quad (2.26)$$

$$A_T = A_r + A_{nr}$$

This lifetime represents the time in which the emitted intensity decays to I_0/e and it can be obtained from the slope of the linear plot, $\log I$ versus t . As τ is measured from a pulsed luminescence experiment, it is called the *fluorescence or luminescence lifetime*. It is important to stress that this lifetime value gives the total decay rate (radiative plus nonradiative rates). Consequently the Equation (2.26) is usually written as:

$$\frac{1}{\tau} = \frac{1}{\tau_0 + \tau_{nr}} \quad (2.27)$$

or

$$\frac{1}{\tau} = \frac{1}{\tau_0} + A_{nr}$$

where $\tau_0 = 1/A_r$, called the *radiative lifetime*, would be the luminescence decay time measured for a purely radiative process ($A_{nr} = 0$). In the general case $\tau < \tau_0$ as the nonradiative rate differs from zero. The decay pattern of a luminescence signal may not be exponential

when the excitation energy reaches the luminescence level after undergoing a number of downward steps. If the number of these steps is n , then the decay signal will contain $(n + 1)$ exponentials. It may be difficult to disentangle all exponentials because the components faster than the response time of the detecting apparatus leave no trace. An additional mechanism that may contribute to the decay of a luminescent level is due to the emission of vibronic lines, corresponding to transitions that involve the emission of a phonon and the emission or absorption of a photon.

2.6 Conclusions

- It was elaborated and developed the necessary technological equipment for the single crystal growing process of the α -ZnAl₂S₄ semiconductor. The starting materials were placed in evacuated sealed quartz ampoules of 8 mm inner diameter and the length, which did not exceed 120 mm in order to exclude the increase of the amount of material transported per unit time and the growing time, respectively. The ampoules were slowly heated up to the synthesis temperature of 1000°C during two days in order to prevent the explosion and maintained in these conditions during five days. For this purpose, a one-zone tube furnace was used was inclined about 15 degrees to the horizontal. Halogen I₂ was used as transporter in the concentration of $c_T=5$ mg/cm³. The temperature inside the alumina tube furnace was precisely controlled in order to prevent the oscillations of temperature, with a temperature accuracy +/- 0.1°C ; thus, the transport rate was kept constant, which is very important for the quality of crystals.
- For the first time, the single crystals of the α -ZnAl₂S₄ spinel type wide band gap semiconductor doped by the transition metals Ti, Co and V have been obtained. The crystals, grown by the chemical vapour transport method, with the activator impurities concentrations 0.01 – 0.1% at. and the volume up to 20 mm³, correspond to optically homogeneous octahedrons with (111) - oriented mirror-like faces.
- The structural characterisation was done by means of XRD, using a single crystal Oxford diffractometer, equipped with a CCD area detector and a graphite monochromator utilizing Mo K_{α} radiation. The x-ray data collected at 200K temperature confirmed that all samples crystallised into the normal spinel type structure with O_h^7 (Fd3m) cubic symmetry.
- The grow α -ZnAl₂S₄: TM crystalline samples were investigated using the following spectroscopic techniques: optical absorption, steady state and time resolved luminescence together lifetime registration of the excited states and PL excitation spectroscopy.

3. SPECTROSCOPIC CHARACTERIZATION OF CO AND V-DOPED α -ZnAl₂S₄ SPINEL TYPE SINGLE CRYSTALS

3.1. Introduction

The potential of vibronic solid-state lasers as stable tunable light sources for high-resolution spectroscopy in the visible and near-infrared spectral range and the expectation for future tunable high-power lasers has stimulated intensive research and evaluations in the solid-state laser community. Currently the activities are mostly focused on transition metal - doped single crystals. Many host materials based on oxide or halide single crystals have been investigated and operated as tunable lasers. One of the most known activators in many host crystals is Cr³⁺ ion. Unlike the crystals containing trivalent chromium, systems based on other transition metal ions and/or other oxidation states are not easy to deal with; ions like Ti, V, Co have a strong tendency to form mixed valence systems [60, 62]. In a number of oxide spinels the tetrahedral coordinated Co²⁺ ions are characterized by a strong luminescence in the visible and near infrared (IR) regions with very short lifetimes [35, 38, 48]. Optical properties of the tetrahedral Co²⁺ in the sulphur surrounding have been studied in [37, 41] and references therein. Properties of vanadium ions incorporated in oxide spinels or other matrices have been studied in various publications, especially their optic and magnetic properties. However, as in the case of Co ions, there are no papers (available to the author of the present research work) on spectroscopic investigations of the V-doped sulphide spinels. This chapter will consider the spectroscopic properties of V- and Co- doped α -ZnAl₂S₄ single crystals.

Bulk stoichiometric α -ZnAl₂S₄ crystals were grown by the chemical vapour transport method, using I₂ as a transport agent, in the temperature range 750 – 850K. The obtained samples, with the initially V and Co – impurity concentrations in the region of 0.01-0.1 at %, were optically homogeneous octahedrons with the dimensions of up to 10mm³ and (111) oriented mirror-like faces. In contrast to the undoped colourless α -ZnAl₂S₄ crystals, the V-doped samples are brown, whereas the Co-doped samples are orange. The normal spinel-type structure of the samples was confirmed by the x-ray analyses, using a single crystal diffractometer Xcalibur (Oxford Instruments), equipped with a CCD area detector and a graphite monochromator utilizing Mo *K_α* radiation. The optical absorption spectra for both undoped and Co- and V-doped α -ZnAl₂S₄ were recorded at room temperature using a Perkin Elmer Lambda 900 spectrometer in the wavelength range 300 – 1700nm. Photoluminescence (PL) was investigated in the temperature range 10 – 300K under excitation in the spectral region of the V and Co impurity absorption bands using a *cw* frequency doubled YAG:Nd laser (λ =532 and 1064nm), He-Ne laser (633 and 1152nm) and a tuneable OPO (300 – 600

nm). The *PL* and *PLe* emission spectra were detected by a North Coast IR liquid nitrogen cooled Ge-photo-detector and an EOS InGaAs photodiode.

3.2. Spectroscopic characterization of Co -doped α -ZnAl₂S₄ spinel type single crystals

The absorption spectra at room temperature of both undoped and Co-doped α -ZnAl₂S₄ are presented in Fig. 3.1. The short-wavelength edge at 0.35 μm ($E_g(300\text{K}) = 28230 \text{ cm}^{-1}$) for the undoped α -ZnAl₂S₄ sample corresponds to the intrinsic absorption (indirect band gap), being in good agreement with the results obtained in [83]. The absorption spectrum of α -ZnAl₂S₄:Co crystals includes the impurity spectral bands located at about 1.6 μm ($E_{A1} \approx 6452 \text{ cm}^{-1}$, quadruplet), 0.77 μm ($E_{A2} = 12985 \text{ cm}^{-1}$, triplet) and 0.48 μm ($E_{A3} = 20163 \text{ cm}^{-1}$, broad band) [84]. As to the absorption edge, for the doped samples it shifts by about 6452 cm^{-1} towards lower energies.

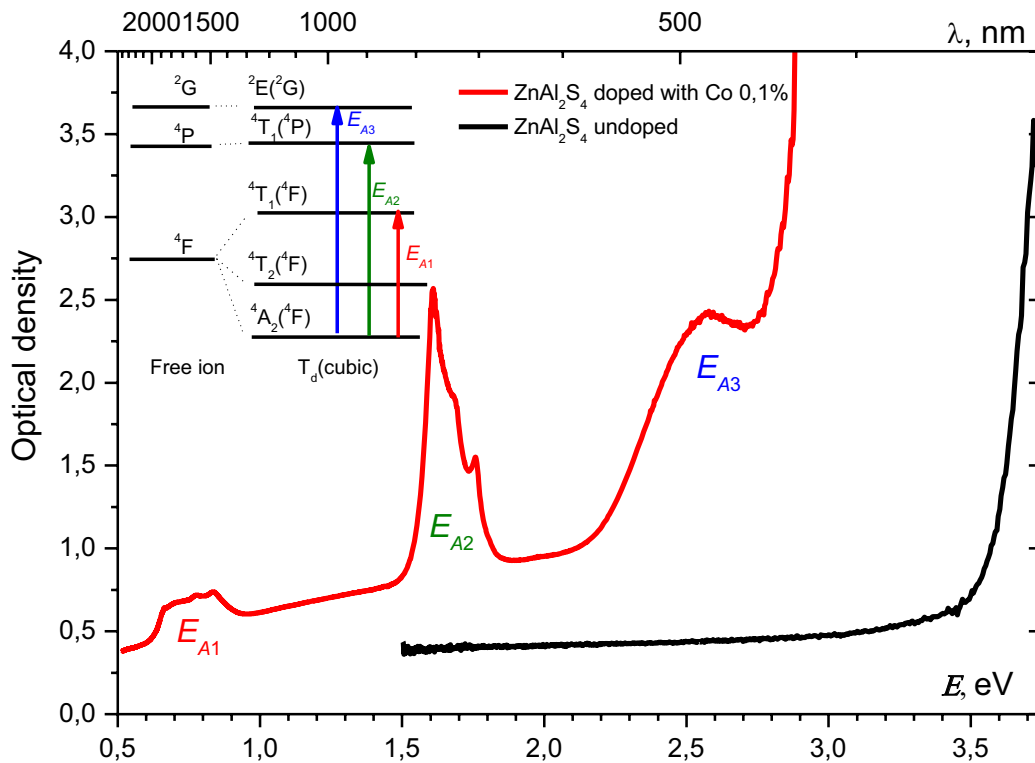


Fig. 3.1 Optical absorption spectra for undoped and Co-doped α -ZnAl₂S₄ single crystals. Energy level splitting for Co ions in T_d symmetry and transitions corresponding to the absorption bands doped material.

In fact, the observed impurity bands are quite similar to those reported for $\text{MgAl}_2\text{S}_4:\text{Co}^{2+}$ and $\text{CaAl}_2\text{S}_4:\text{Co}^{2+}$ [41], $\text{MgAl}_2\text{O}_4:\text{Co}^{2+}$ [85] and $\text{ZnGa}_2\text{S}_4:\text{Co}^{2+}$ [37], where Co ions are in tetrahedral coordination.

The E_{A2} absorption lines are ascribed to the spin and electric dipole allowed transitions ${}^4A_2(4F) \rightarrow {}^4T_1(4P)$. Indeed, in $\text{MgAl}_2\text{S}_4:\text{Co}^{2+}$, $\text{CaAl}_2\text{S}_4:\text{Co}^{2+}$ [41] as well as in $\text{ZnS}:\text{Co}^{2+}$, where the impurity replaces only the tetrahedral coordinated Zn^{2+} ion [32], the similar

absorption lines are located almost at the same energies (Fig. 3.2). In conformity with the Crystal Field Theory [75], the ${}^4T_1({}^4P)$ state of Co^{2+} ion sited in T_d symmetry splits into three sublevels Γ_6 , Γ_8 and $\Gamma_7+\Gamma_8$ due to the first order of the spin – orbit coupling effects. Thus, the observed three peaks of the E_{A_2} spectral component are assigned, according to the selection rules from [71], to the electron transitions from the ground state ${}^4A_2({}^4F)$ to the three sublevels of the excited level ${}^4T_1({}^4P)$. The energy of spin-orbital coupling of the interaction between total orbital angular momentum and total spin momentum of the valence electrons, obeying the Russel – Saunders coupling scheme, is describe by the relation:

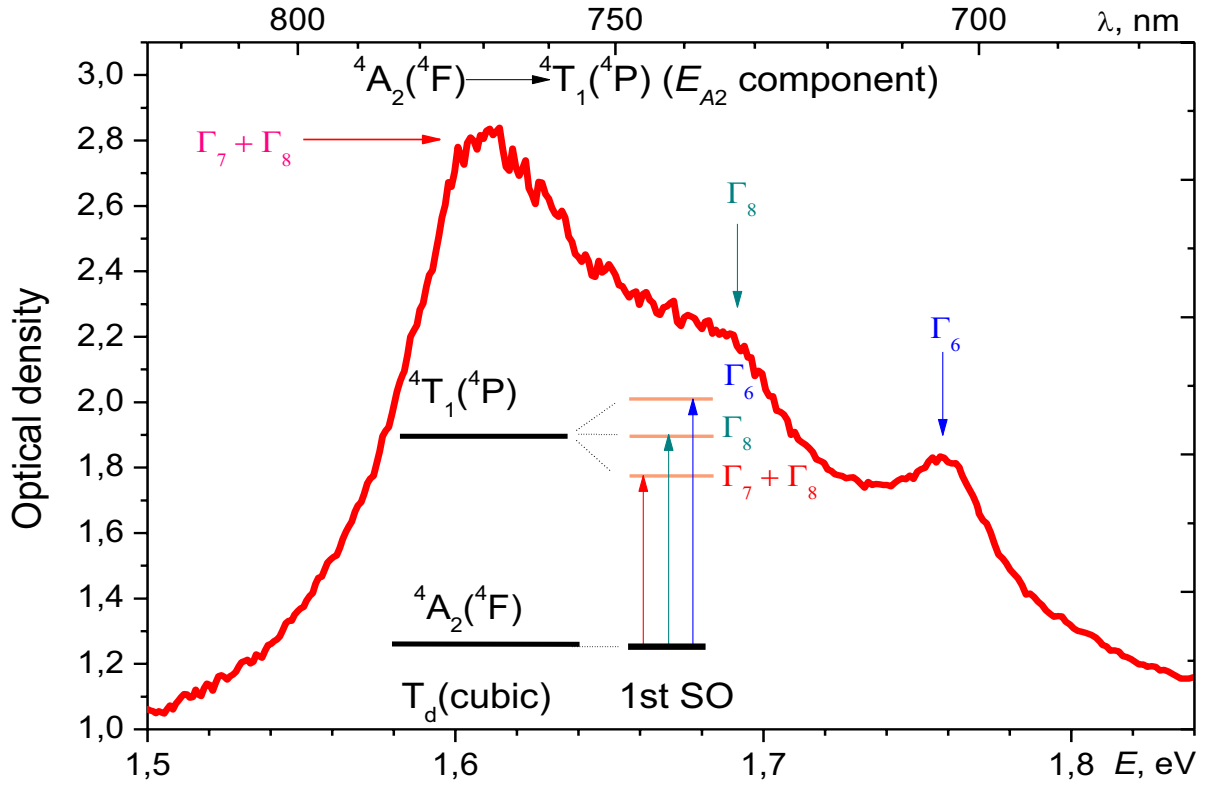


Fig. 3.2 E_{A_2} absorption component for Co-doped α -ZnAl₂S₄ single crystals and the transitions from the ground state ${}^4A_2({}^4F)$ to the three sublevels of the excited ${}^4T_1({}^4P)$ level splitted by spin-orbit coupling

$$W = \lambda(L, S) \frac{J(J+1) - L(L+1) - S(S+1)}{2} \quad (3.1)$$

where J , L , S are quantum numbers and $\lambda(L, S)$ is the constant of spin-orbit coupling. Thus, the energetic width of the multiplet ${}^4T_{1g}({}^4P)$, in other words, the distance between $J=|L+S|$ and $J=|L-S|$, is :

$$\left. \begin{aligned} \Delta W &= \lambda(L, S) S(2L+1) & \text{if } L \geq S \\ \Delta W &= \lambda(L, S) L(2S+1) & \text{if } L \leq S \end{aligned} \right] \quad (3.2)$$

The energetic distance between the terms of the multiplet is $\Delta W = 1286 \text{ cm}^{-1}$ (see Table 3.1). Hence, knowing that quantum numbers for the term ${}^4T_{1g}({}^4P)$ are $L=1, S=3/2$, it is possible to calculate the constant of the spin-orbit coupling :

$$\lambda(L,S) = \frac{\Delta W}{L(2S+1)} = \frac{1286(\text{cm}^{-1})}{4} \approx 321(\text{cm}^{-1}) \quad (3.3)$$

The E_{A1} IR component consists of at least four lines (see Fig. 3.3) ascribed to the ${}^4A_2({}^4F) \rightarrow {}^4T_1({}^4F)$ transition. By following the same procedure, as was described for the case above, the constant of spin-orbit coupling for the excited level ${}^4T_1({}^4F)$ has been estimated to be:

$$\lambda(L,S) \approx 132 \text{ cm}^{-1} \quad (3.4)$$

Both results are in good agreement with the data in [32, 37, 41] and are the confirmation that Co^{2+} ions are in the tetrahedral surrounding.

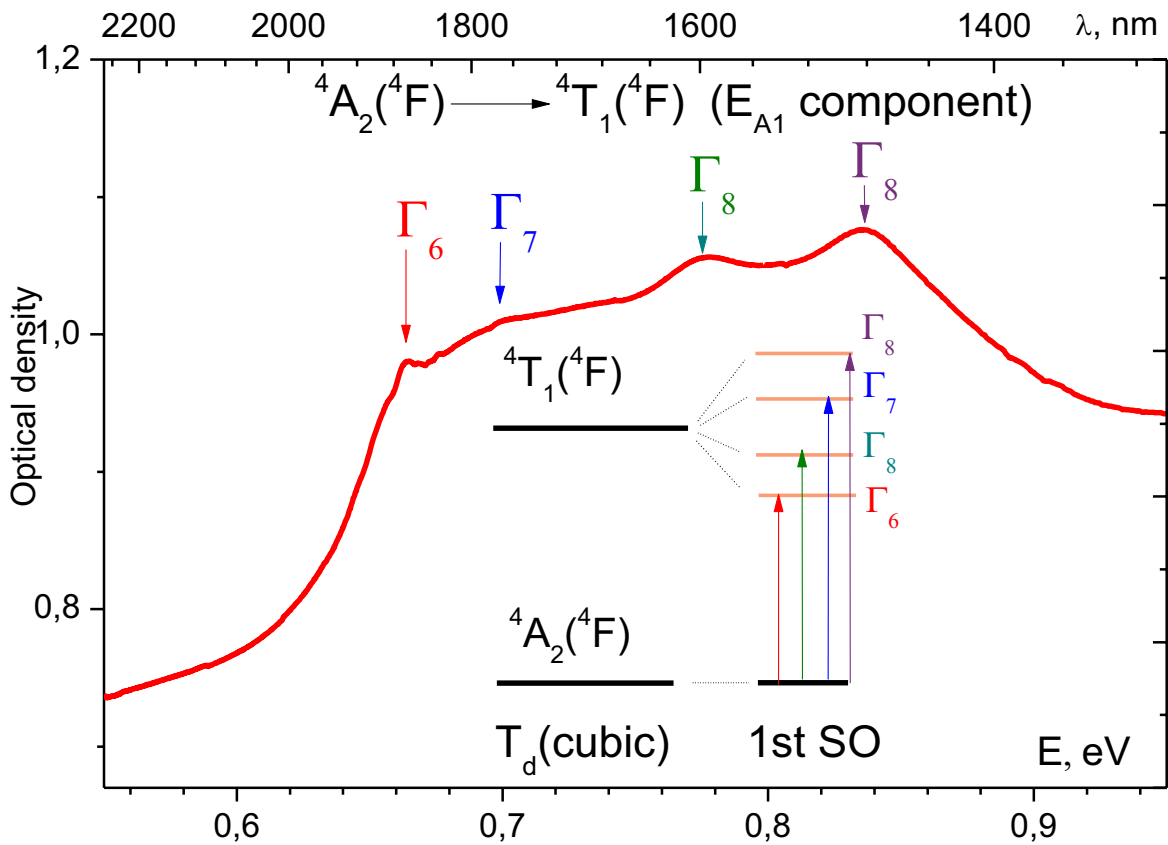


Fig. 3.3 E_{A1} IR absorption component for Co-doped $\alpha\text{-ZnAl}_2\text{S}_4$ single crystals and transitions from the ground state ${}^4A_2({}^4F)$ to the four sublevels of the ${}^4T_1({}^4F)$ excited level.

The quite intensive absorption within E_{A3} band is due to the fact that, in spite of the forbiddenness of the ${}^4A_2({}^4F) \rightarrow {}^2A({}^2G)$ transition, at the ligand field strength of Co^{2+} in T_d ($Dq \approx 400 \text{ cm}^{-1}$) the ${}^4T_1({}^4P)$ excited level is very close to the doublet states arising from the 2G free – ion term and the spin orbit mixing of quartets and doublets, that relaxes the spin-forbidden transitions to these doublet states.

The long-wavelength shift of the absorption edge of α -ZnAl₂S₄:Co crystals, with respect to the edge of the undoped samples, according to [37], could be attributed to an impurity energetic band that arises due to the formation of a solid solution between the dopant and the host lattice (Zn_(1-x)Co_xGa₂S₄). However, this is not the case for the compound discussed here, because in [37] the concentration of the dopant was quite large, up to 2% mol, i.e. about an order of magnitude higher than in the samples analysed by the author of the present research. Therefore, the observed “red shift” of the edge in the latter case can be attributed to the long wavelength side of an intensive absorption broad band caused by the high energy optical transitions of Co²⁺-ions, perhaps ${}^4A_2({}^4F) \rightarrow {}^2T_2({}^2G)$.

Table 3.1 Energies of the spectral components of the absorption and emission spectra of Co²⁺ ions in α -ZnAl₂S₄ spinel and their assignments

<u>Absorption</u>		<u>Emission</u>				
Energy, eV	Assignment	Energy, eV	Assignment			
E_{A1}	${}^4A_2({}^4F) \rightarrow {}^4T_1({}^4F)$	E_{PL1}	${}^2A_1({}^2G) \rightarrow {}^4T_1({}^4F)$			
				0.664	${}^4A_2({}^4F) \rightarrow \Gamma_6$	1.509
				0.700	${}^4A_2({}^4F) \rightarrow \Gamma_8$	1.499
				0.775	${}^4A_2({}^4F) \rightarrow \Gamma_7$	1.485
0.836	${}^4A_2({}^4F) \rightarrow \Gamma_8$					
E_{A2}	${}^4A_2({}^4F) \rightarrow {}^4T_1({}^4P)$	E_{PL2}	${}^2E_1({}^2G) \rightarrow {}^4T_2({}^4F)$			
				1.610	${}^4A_2({}^4F) \rightarrow \Gamma_7 + \Gamma_8$	1.470
				1.688	${}^4A_2({}^4F) \rightarrow \Gamma_8$	1.459
1.758	${}^4A_2({}^4F) \rightarrow \Gamma_6$	1.444				
E_{A3}	${}^4A_2({}^4F) \rightarrow {}^2A_1({}^2G)$	E_{PL3}	${}^4T_1({}^4P) \rightarrow {}^4T_2({}^4F)$			
2.570		1.122				
E_{A4}	${}^4A_2({}^4F) \rightarrow {}^2T_2({}^2G)$	1.098				
2.878		1.088				
		E_{PL4}	${}^2E_1({}^2G) \rightarrow {}^4T_1({}^4F)$			
		0.957				

The ratio of the energies of the absorption components $E_{A2}/E_{A1} \approx 2.1$ corresponds to the ratio of $Dq/B \approx 0.6$ in the Tanabe – Sugano diagram (see Fig. 3.4). Knowing the Dq/B value, one can find the Racah parameter B taking into account the E/B value for each level involved in the absorption process. In this way the crystalline field parameter Dq and the value of B for Co²⁺ ions in α -ZnAl₂S₄ were obtained as: $B = 0.076\text{eV}$ (618cm^{-1}) and $Dq \approx 0.046\text{eV}$ (370cm^{-1}). These values are in good agreement with those for Co ions in tetrahedral coordinations of sulphur obtained in [36-37]

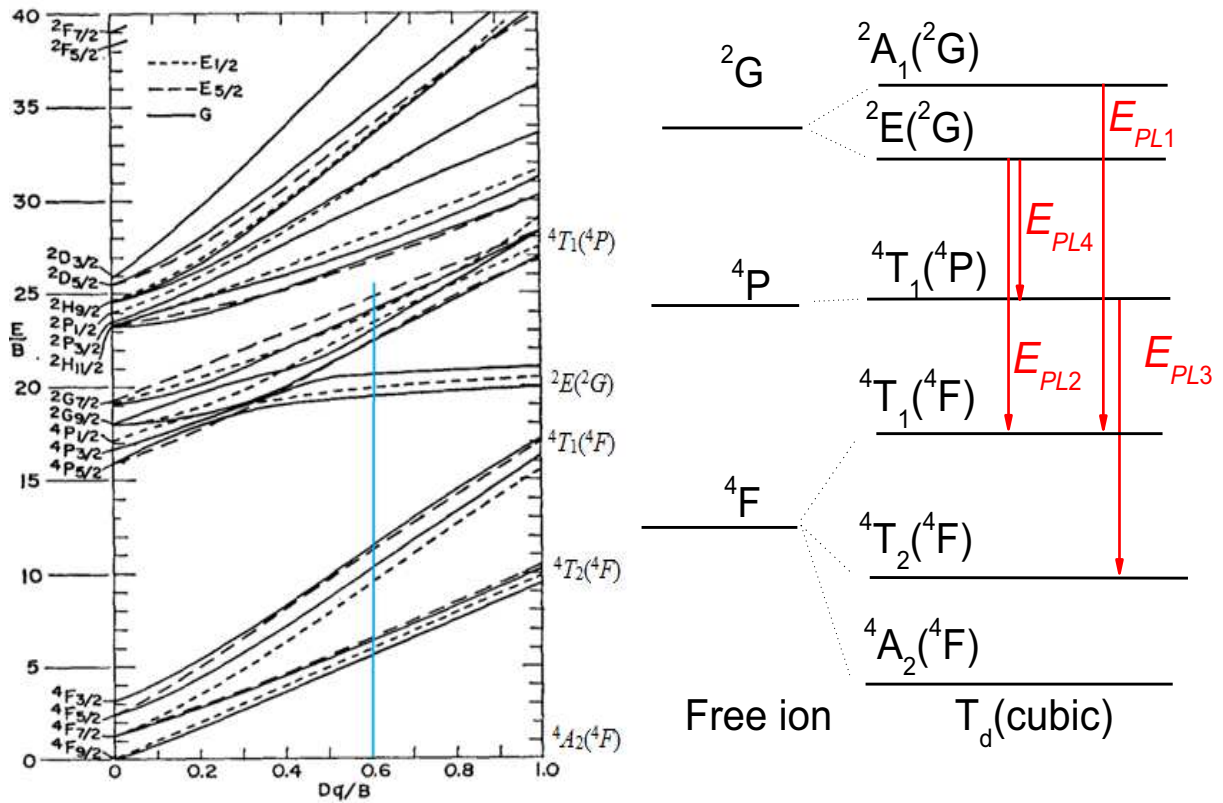


Fig. 3.4 Tanabe – Sugano diagram for Co^{2+} ions in tetrahedral coordination taken from [32]

The steady-state *PL* spectra taken at temperatures 10 and 75K are presented in Fig. 3.5 [86]. It should be mentioned that the integral intensity of luminescence is decreasing with the rise of temperature due to the nonradiative transitions that are more probable at high temperatures. On the short wavelength wing of the main spectral broad band, centred at about 1.3eV, one can distinguish several components consisting of narrow lines, which completely disappear at T over 100K. A weak narrow line can be also observed at 1.12eV ($T=10\text{K}$). However, a real contribution of different spectral components in the integral emission spectrum has been revealed using the time-resolved *PL* measurements at low temperature and different excitation wavelengths λ_{exc} (Fig. 3.6).

Fig. 3.6a shows the fast decaying spectral components that are manifested at the short (less than $1\mu\text{s}$) time delay. Several narrow well-resolved spectral lines in the 1.51eV-1.42eV interval (E_{PL1} component) are dominating the spectrum when the excitation photons energies correspond to the E_{A3} absorption broad band and exceed the E_{A2} value (measurements were carried out for $\lambda_{exc1}=496, 530$ and 658nm).

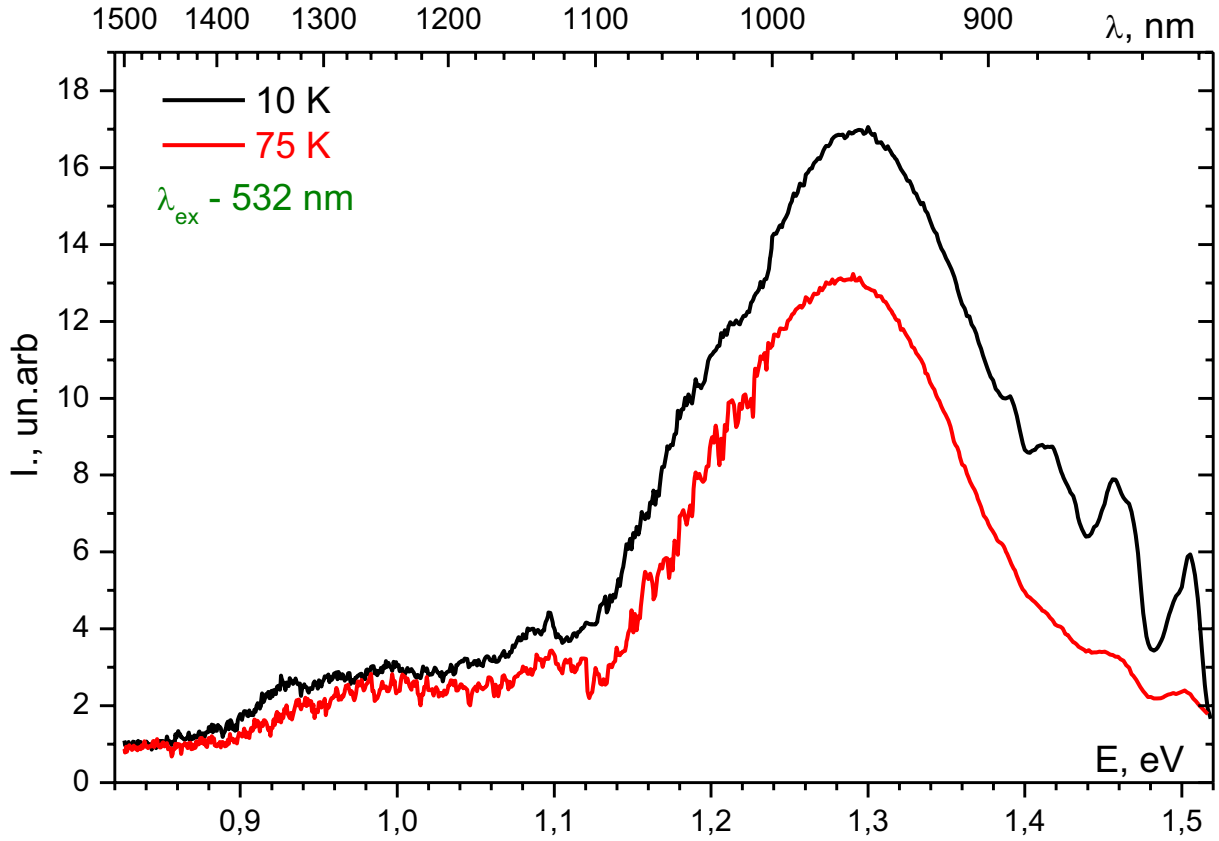


Fig. 3.5 Steady-state luminescence spectra of α -ZnAl₂S₄:Co²⁺ at low temperatures.

When the excitation energy lies within the E_{A2} absorption component ($\lambda_{exc2} = 700\text{nm}$), the short wavelength narrow lines disappear; there are narrow lines at 1.1eV (E_{PL3} component) that are coming to dominate the PL spectrum. The time decay of the E_{PL1} component is comparable with the time resolution of the measurements ($\sim 10^{-6}\text{s}$), limited by the time response of the Ge- detector. The fastest E_{PL1} narrow lines are ascribed to the transition from ${}^2A(^2G)$ level to the lower excited triple degenerated ${}^4T_1(^4F)$ state, split by the spin-orbit coupling. The zero phonon lines $E_{PL1}^{(0)} = 1.509\text{eV}$ are accompanied by the 1st ($E_{PL1}^{(1)} = 1.470\text{eV}$) and the 2nd ($E_{PL1}^{(2)} = 1.431\text{eV}$) vibronic replica, the phonon energy being equal to $\hbar\Omega_{Ph} = 39\text{meV}$ (see Table 3.1). The “intermediate” narrow line at $E_{PL3} = 1.122\text{eV}$, whose intensity is maximal at the excitation just into the E_{A2} band (${}^4A_2(^4F) \rightarrow {}^4T_1(^4P)$ optical transition), is attributed to the transition ${}^4T_1(^4P) \rightarrow {}^4T_2(^4F)$, i.e. as is the case of E_{PL1} , the final level is also an excited state of Co²⁺ ion. According to the Tanabe-Sugano diagram for the d^7 ions in a tetrahedral coordination[32], see Fig. 3.4, the slopes that characterize the behaviour of the upper ${}^2A(^2G)$ and ${}^4T_1(^4P)$ states energy as a function of the crystal field intensity (Dq/B values), and the corresponding slopes of the ${}^4T_1(^4F)$ and ${}^4T_2(^4F)$ lower states are nearly the same, which explains the narrowness of spectral lines in the emission.

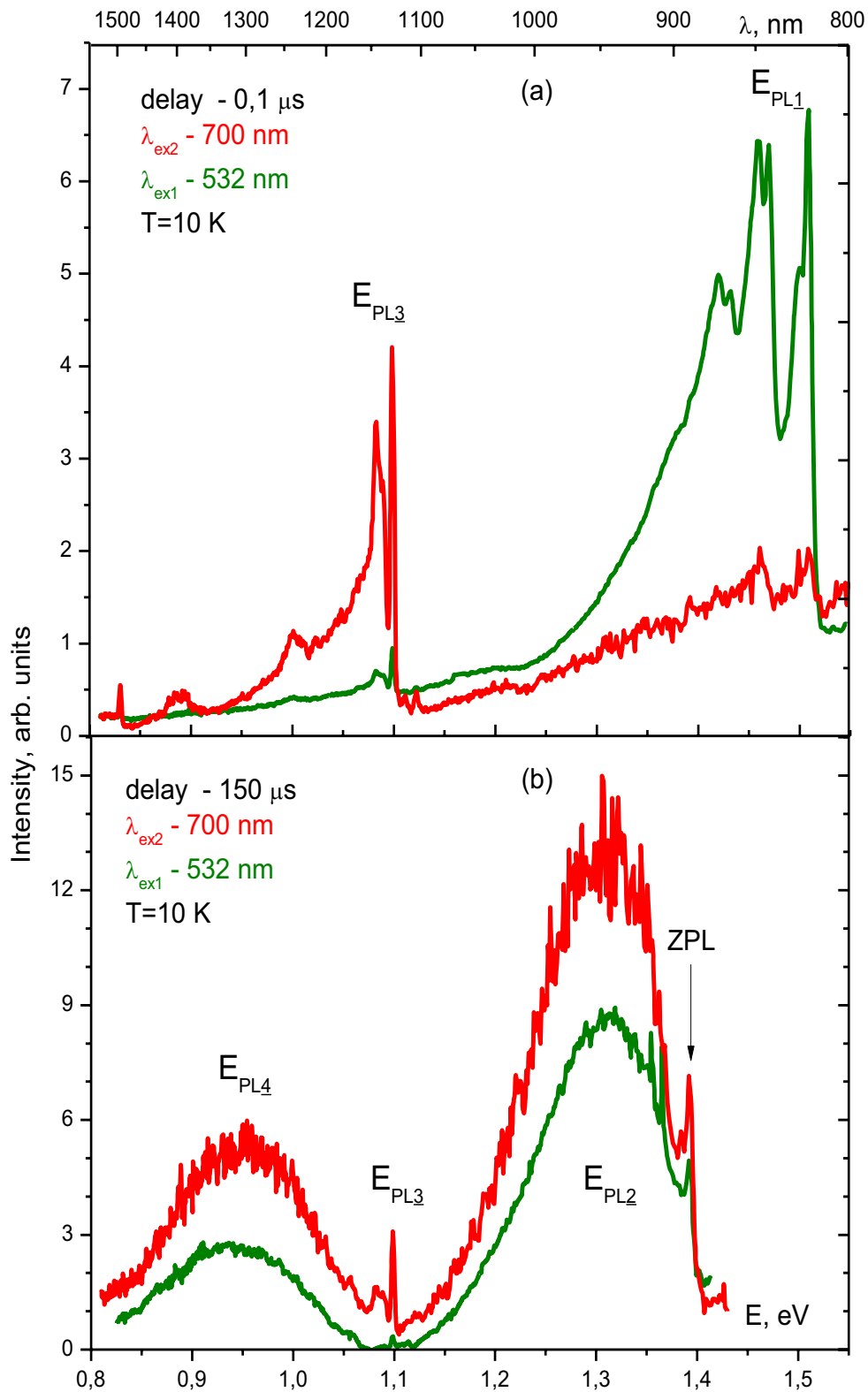


Fig. 3.6 Time-resolved luminescence spectra of Co-doped ZnAl₂S₄ at low temperature:

- a) E_{PL1} and E_{PL3} “fast” narrow line components under excitations at $\lambda_{exc1}=530\text{nm}$ and $\lambda_{exc2}=700\text{nm}$;
- b) E_{PL2} and E_{PL4} “slow” vibronic broad bands under same excitations.

The spectral components with a slow decay, registered with a time-delay $150\mu\text{s}$, are presented in Fig. 3.6b. Two broad bands centred at $E_{PL2} = 1.32\text{eV}$ and $E_{PL4} = 0.96\text{eV}$ appear under both pulsed excitations $\lambda_{exc1} = 530 \text{ nm}$ and $\lambda_{exc2} = 700 \text{ nm}$. Since the energy of the 2E (2G) level is lower than that of the 4T_1 (4P) one, the luminescent bands E_{PL2} and E_{PL4} can be

ascribed to the partially forbidden transitions ${}^2E({}^2G) \rightarrow {}^4T_2({}^4F)$ and ${}^2E({}^2G) \rightarrow {}^4T_1({}^4F)$, respectively. Unlike the fast components case, there is a big difference on the Tanabe-Sugano diagram between the slope of the upper long living ${}^2E({}^2G)$ level and of the ${}^4T_2({}^4F)$ and ${}^4T_1({}^4F)$ states, that is in good agreement with the big width of the *PL* spectral bands.

Thus, in conclusion, it can be mentioned that the optical absorption spectral bands attributed to Co^{2+} ions in the tetrahedral coordination of sulphur are similar to those of the cobalt-doped oxide spinels host crystals, the former being shifted to the lower energies. The impurity absorption of $\alpha\text{-ZnAl}_2\text{S}_4\text{:Co}$ crystals caused by the ${}^4A_2({}^4F) \rightarrow {}^4T_1({}^4P)$ (E_{A2} component) and ${}^4A_2({}^4F) \rightarrow {}^4T_1({}^4F)$ transitions (E_{A1} IR component) corresponds to the spectral region used in the fibre-optics communication systems, therefore this material could be of practical interest as a saturable absorber. The time-resolved *PL* spectra obtained under different excitation wavelengths revealed four radiative components caused by the electronic transitions from ${}^2A({}^2G)$, ${}^4T_1({}^4P)$ and ${}^2E({}^2G)$ initial excited levels of Co^{2+} ions, the final ones being ${}^4T_2({}^4F)$ and ${}^4T_1({}^4F)$ excited states.

3.3. Spectroscopic characterization of V-doped $\alpha\text{-ZnAl}_2\text{S}_4$ spinel type single crystals

This sub-chapter investigates the absorption and luminescent properties of $\alpha\text{-ZnAl}_2\text{S}_4\text{:V}$ single crystals. The emission efficiency of this material determined by V^{3+} -ions is shown to increase

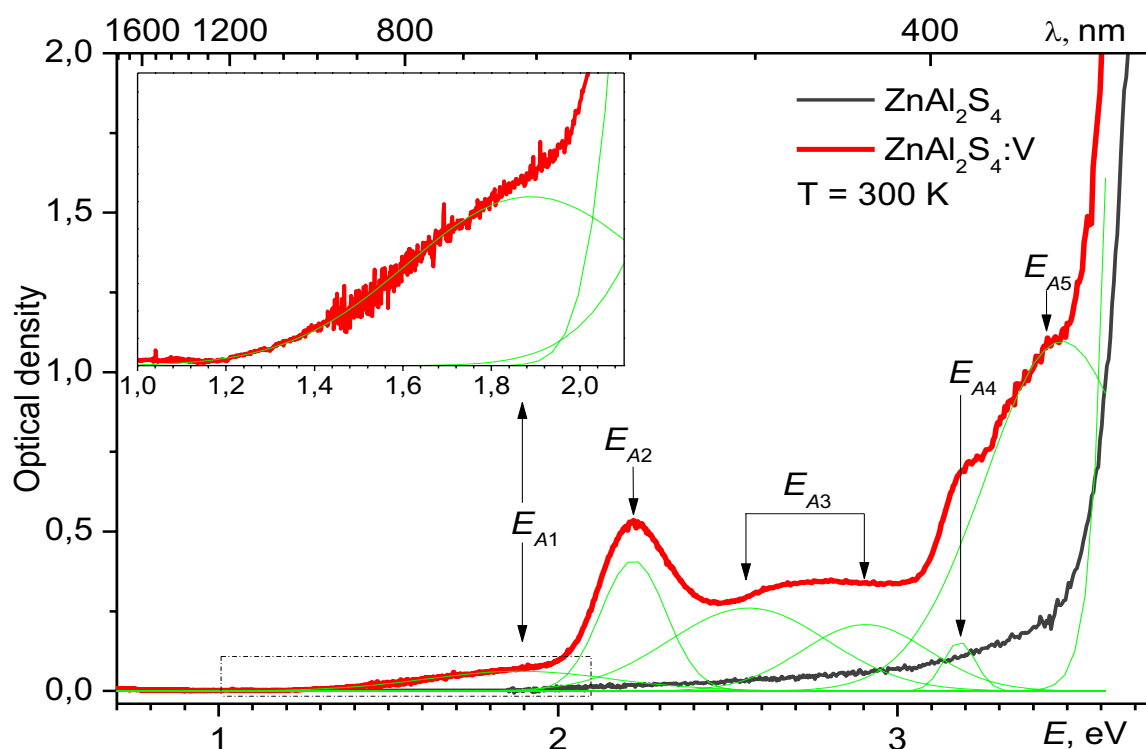


Fig. 3.7 Optical absorption spectra for undoped and V-doped $\alpha\text{-ZnAl}_2\text{S}_4$ single crystals; on the insert – E_{A1} absorption band

with the rise of temperature. The absorption spectra of both undoped and V-doped $\alpha\text{-ZnAl}_2\text{S}_4$ are presented in

Fig. 3.7. The short-wavelength edge located at the wavelength 0.35 μm for the undoped $\alpha\text{-ZnAl}_2\text{S}_4$ sample corresponds to the intrinsic absorption, being in good agreement with the results obtained in [83] (indirect band gap $E_g(300\text{K}) \approx 3.5\text{eV}$). The absorption spectrum of $\alpha\text{-ZnAl}_2\text{S}_4:\text{V}$ crystals includes several spectral components: a weak broad band located at $E_{A1} \approx 1.72\text{eV}$ (Fig. 3.7, insert); an intense band centred at $E_{A2} \approx 2.22\text{eV}$, at least one broad band at $E_{A3} \approx 2.7\text{eV}$, and two prominent bands at $E_{A4} \approx 3.18\text{eV}$ and $E_{A5} \approx 3.41\text{eV}$.

Steady-state PL spectra of $\alpha\text{-ZnAl}_2\text{S}_4:\text{V}^{3+}$ under $\lambda_{\text{exc}}=560\text{nm}$ at different temperatures are plotted in Fig. 3.8 [87]. As is clear from Fig. 3.8, the integral intensity of the spectrum is

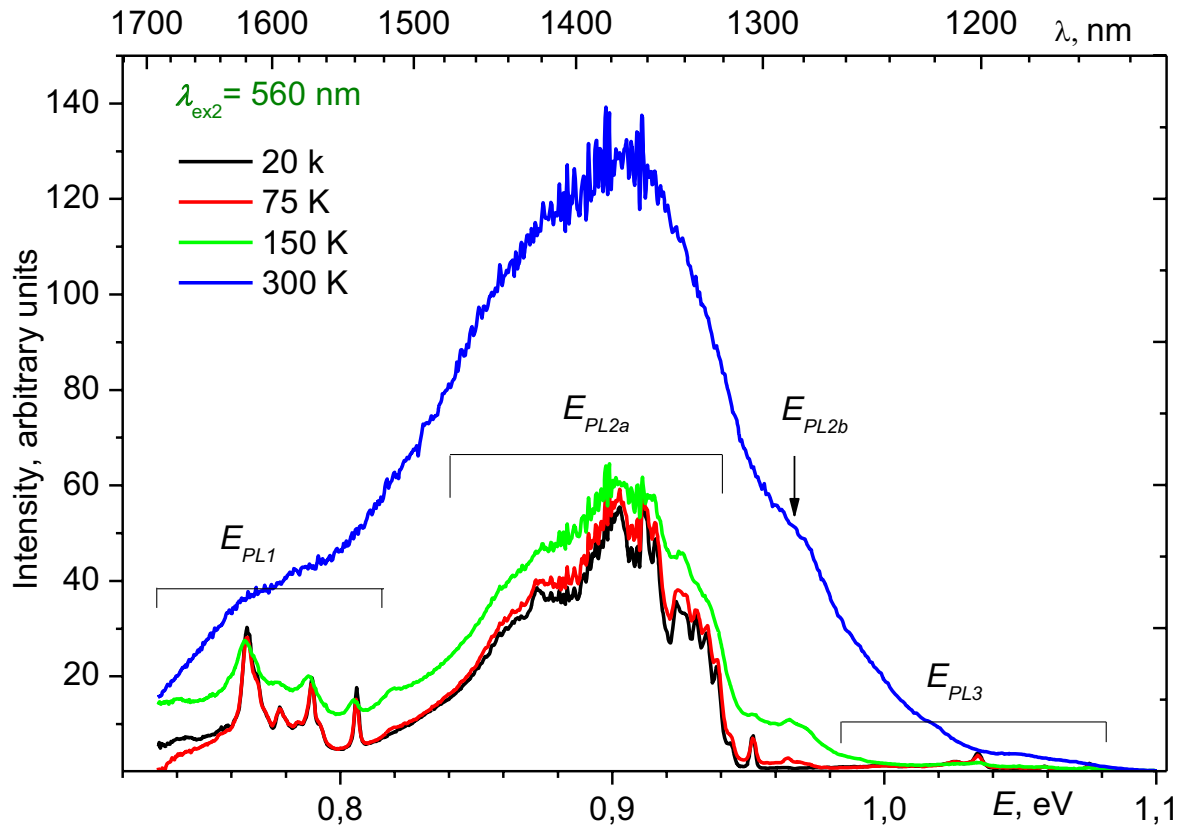


Fig. 3.8 Steady-state PL spectra of $\alpha\text{-ZnAl}_2\text{S}_4:\text{V}^{3+}$ at different temperatures

increasing dramatically with temperature; at room temperature it is higher by a factor of four reported to that at 10K (see also Fig. 3.9). In Fig. 3.8, at low temperature, three main spectral regions can be clearly distinguished – E_{PL1} , E_{PL2} and E_{PL3} . At room temperature, neither the intensity nor the shape of the PL spectra depend on the excitation light wavelength: $\lambda_{\text{ex1}}=633\text{nm}$ (E_{A1} band), $\lambda_{\text{ex2}}=560\text{nm}$, $\lambda_{\text{ex3}}=532\text{nm}$ (E_{A2} band) or $\lambda_{\text{ex4}}=410\text{nm}$ (E_{A4} band). On the contrary, at low temperature (20K), the features of the PL spectra, especially the intensity of the E_{PL3} narrow lines, are sensitive to the excitation wavelength (see also Fig. 3.10). Under excitation in the E_{A2} bands, their intensities are quite weak. When the excitation energies exceed 2.5eV these lines become prominent, but in both cases the intensity of the E_{PL3} lines is less than that of the E_{PL2} emission component. There occurs a dramatic increase of the E_{PL3}

narrow lines intensity under $\lambda_{ex1}=633\text{nm}$ excitation, those lines becoming the dominant component of the emission spectrum.

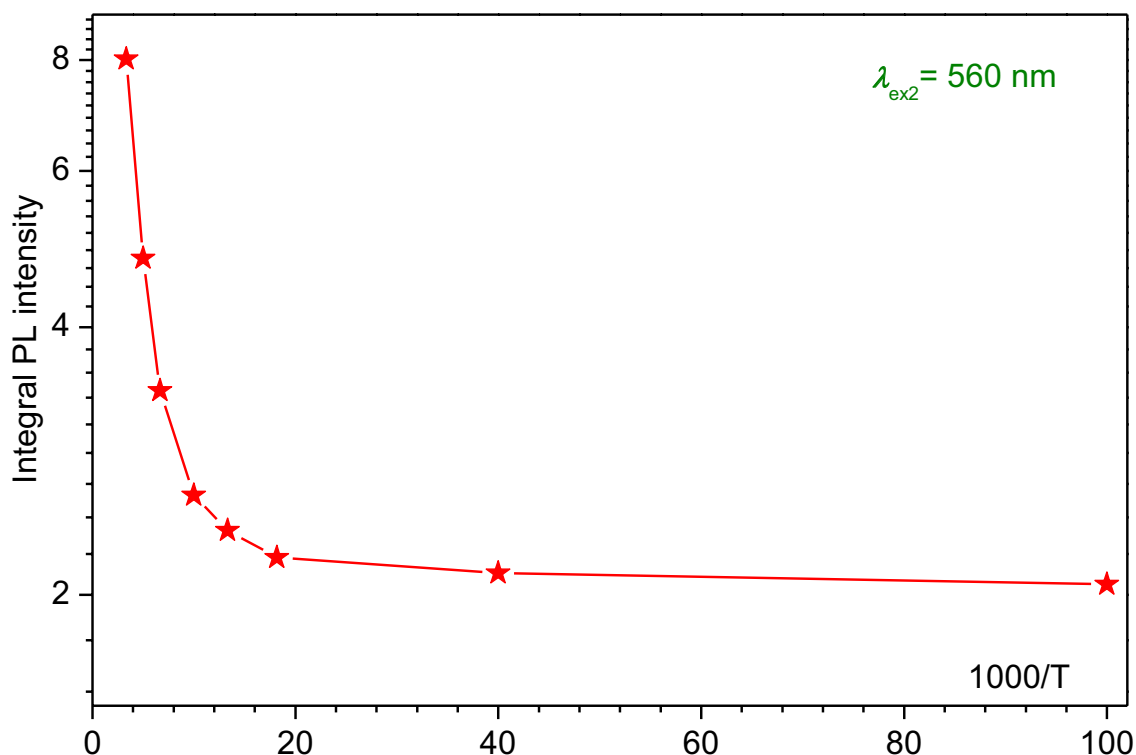


Fig. 3.9 Temperature dependence of the integral *PL* intensity of $\alpha\text{-ZnAl}_2\text{S}_4\text{:V}$.

The interpretation of the absorption spectra that is directly related to determination of the oxidation state of vanadium impurity is quite difficult because there are at least three possible oxidation states in two coordinations: V^{2+} , V^{3+} and V^{4+} ions in octahedral and tetrahedral sites of $\alpha\text{-ZnAl}_2\text{S}_4$ spinel structure. The monovalent V^+ oxidation state is less probable because of a big difference between its ionic radius and the radii of Al^{3+} (0.53\AA) and Zn^{2+} (0.74\AA) [88].

Aside from the case of V^{5+} , where optical spectra are the subject of a charge transfer process between ligands and the central ion, the radius of V^{4+} ion (0.58\AA) is the closest to that of Al^{3+} ions in the octahedral coordination. The replacement of the host trivalent cations by the V^{4+} ions was revealed in $\text{LaGaO}_3\text{:V}$ single crystals [66], where the IR luminescence observed at $\sim 1400\text{nm}$ is provided by the octahedral coordinated V^{4+} ions. The d^1 electronic configuration of the tetravalent vanadium, like that of the octahedral coordinated Ti^{3+} ions, is characterized by only one absorption and one emission broad bands due to ${}^2E \leftrightarrow {}^2T_2$ transitions. The shapes of these bands practically do not depend on temperature. However, in the case of $\alpha\text{-ZnAl}_2\text{S}_4\text{:V}$ the *PL* spectra have a complex structure that is dependent on temperature. This fact favours the assumption that there is no tetravalent vanadium in the octahedral or tetrahedral coordination.

The presence of V^{2+} and V^{3+} ions in tetrahedral coordination can be also excluded, taking into consideration that the luminescence manifested by the tetrahedral coordinated V^{2+} and V^{3+} ions (mixed valence states) in ZnS:V crystals corresponds to the middle infrared region ($\lambda_{PL} \sim 2\mu\text{m}$) [60]. The position, shape and temperature behaviour of the PL spectra are quite different from those presented in this investigation.

Still, the same two oxidation states of the vanadium ions in the octahedral sites are both possible, however, the radius of V^{3+} ion – 0.64\AA is closer to that of Al^{3+} ion, whereas that of V^{2+} ion radius is much larger (0.79\AA). Besides, V^{2+} ions in octahedral coordination of sulphur in the vanadium doped chalcogenide glass (GLS) [70] exhibit optical spectra that have not any similarity with the spectra presented in Fig. 3.8 and Fig. 3.10. Taking into account these facts, the V^{2+} oxidation state can be also excluded. The above arguments indicate that in the case of $\alpha\text{-ZnAl}_2\text{S}_4$ host lattice, the trivalent vanadium ions replace aluminium in the octahedral environment.

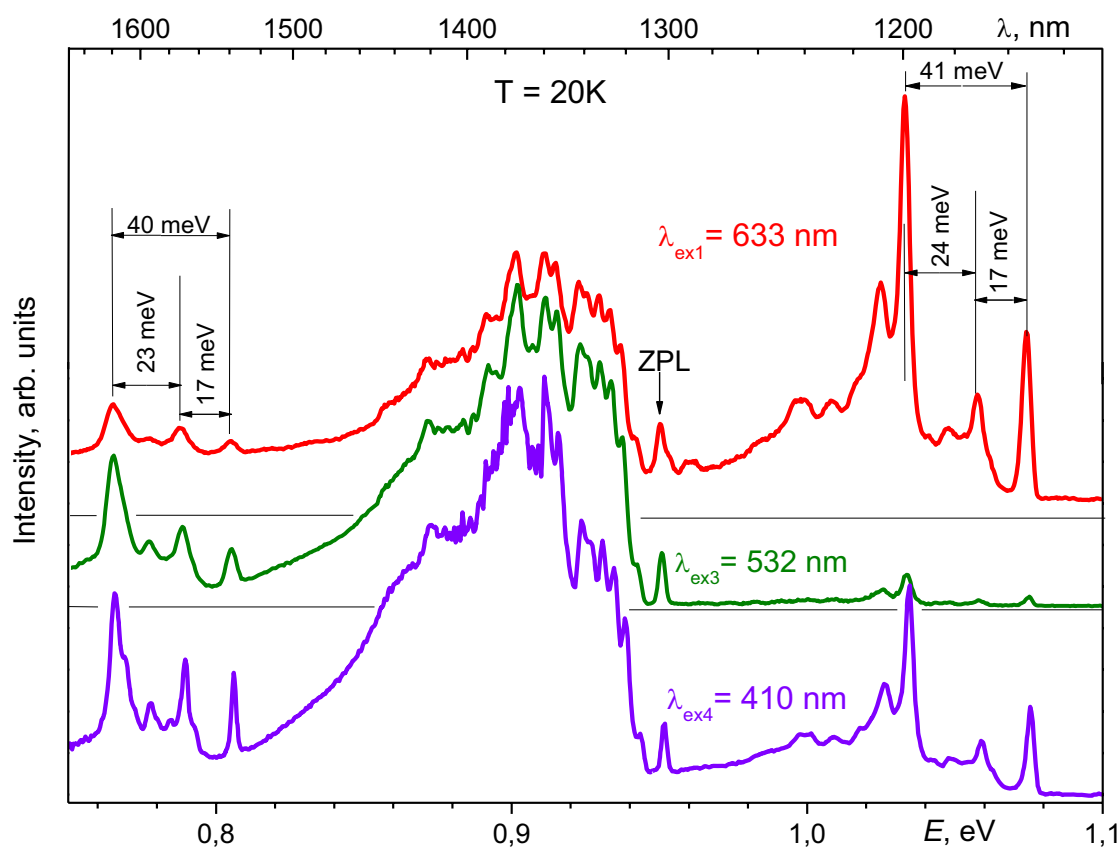


Fig. 3.10 Low temperature PL spectra at three excitation wavelengths: 410nm, 532nm and 633 nm.

A careful inspection of the PL spectra of $\alpha\text{-ZnAl}_2\text{S}_4\text{:V}^{3+}$ reveals the following peculiarities (Fig. 3.8 and Fig. 3.10). Firstly, the emission spectrum is located at about 1.3eV from the first prominent absorption band that by far exceeds a reasonable value of the Stokes shift. Secondly, with the rise of temperature, starting from the value $T > 100\text{K}$, the integral intensity of the PL increases (Fig. 3.9) and E_{PL2} emission becomes predominant, to the detriment of the E_{PL1} spectral component. However, it has to be underlined that in the low

temperature region of 10-100K the ratio of the intensities of these two components $I(E_{PL2})/I(E_{PL1})$ remains practically constant. The increase of the integral PL intensity with temperature indicates that there is an energetic barrier between the excited electronic levels responsible for these two components. The level providing the E_{PL2} emission is located higher than the level responsible for E_{PL1} by the energy corresponding to the $T \sim 100\text{K}$ and has a shorter radiative lifetime than that of E_{PL1} component. At low temperature, the structure of E_{PL2a} component includes a weak narrow line at 0.95eV that can be ascribed to the zero phonon line (ZPL) and a vibronic replica of this line merged into a broad band (0.82 – 0.94eV). Besides the E_{PL2a} component, at $T \sim 150\text{K}$ an additional broad band E_{PL2b} , centred at about 0.98eV, occurs. The intensity of this band rises with temperature and makes an essential contribution in the integral spectrum at 300K.

Thirdly, there are several structure similarities between the E_{PL1} and E_{PL3} components in spite of a wide spectral interval that separates them. As is evident in Fig. 3.10, the energy gaps between some E_{PL1} -peaks and between the similar peaks belonging to the E_{PL3} component are approximately the same. Hence, one can suppose that the radiative transitions related to the E_{PL3} and E_{PL1} spectral components involve the same excited level: in the first case, it serves as a final level for the transition from a higher excited state, in the second – as the initial level from which the transition to the ground state takes place. From the Tanabe – Sugano diagram for the octahedral d^2 configuration [74] (Fig. 3.11a) it follows that the role of such common level can be taken by the combination of the ${}^1T_{2g}$ and ${}^1E_g({}^1D)$ excited states, while the role of the higher excited level that provides the E_{PL3} emission – by the ${}^1A_{1g}({}^1G)$ state. These states are characterized by a weak electron-phonon interaction that explains the narrowness of the E_{PL1} and E_{PL3} emission lines.

Taking into account that the sum $E_{PL1} + E_{PL3} \approx 1.85\text{eV}$ corresponds to the energy of the E_{A1} absorption band, the proposed interpretation is consistent with the dramatic increase of the E_{PL3} contribution into the integral spectrum under the $\lambda_{\text{ex1}} = 633\text{nm}$ (1.96eV) excitation (Fig. 3.10). Thus the first absorption band E_{A1} can be ascribed to the spin-forbidden but electric quadrupole-allowed ${}^3T_{1g}({}^3F) \rightarrow {}^1A_{1g}({}^1G)$ electronic transitions.

The next absorption band – E_{A2} band – is attributed to the spin- and electric quadrupole-allowed ${}^3T_{1g}({}^3F) \rightarrow {}^3T_{1g}({}^3P)$ transitions, whereas the E_{A3} band is due to superposition of the partially forbidden transitions from the ground state ${}^3T_{1g}({}^3F)$ to ${}^1T_{1g}({}^1G)$ and ${}^1T_{2g}({}^1G)$ levels, that can be revealed by decomposition of the absorption spectrum into elementary Gaussian bands. The E_{A4} corresponds to the spin-allowed but electric quadrupole-forbidden ${}^3T_{1g}({}^3F) \rightarrow {}^3A_{2g}({}^3F)$ electronic transitions. Hence, the ratio of the energies of the absorption components $E_{A4}/E_{A2} \approx 1.25$ corresponds to the ratio of $Dq/B \approx 2.17$ in the Tanabe –

Sugano diagram. Knowing the Dq/B value, one can find the Racah parameter B taking into account the E/B value for each level involved in the absorption process. In this way the crystalline field parameter Dq and the value of B for V^{3+} ions in $\alpha\text{-ZnAl}_2\text{S}_4$ were obtained as: $B=61\text{meV}$ (490cm^{-1}) and $Dq \approx 0.132\text{eV}$ (1070cm^{-1}). These values are in good agreement with those for V ions in octahedral coordinations of sulphur obtained in [70]. The $E_{A5}=3.41\text{eV}$ band most probably is due to the charge transfer process between $S^{2-} - V^{3+}$ ions. The overlap of that band with the fundamental absorption edge can lead to the red shift of the latter. It is necessary to emphasise the relatively high intensities of the E_{A1} and E_{A3} spin-forbidden components and their very large bandwidths – at least two times larger than those of the E_{A2} and E_{A4} bands (Fig.1). This situation may be tentatively explained by the influence of the host lattice intrinsic defects (the cation inversion or anion vacancies, for example) on the environment of the impurity ions, resulting in the partial violation of the selection rules and inhomogeneous broadening, i.e. in the modification of the impurity optical spectrum [89-90].

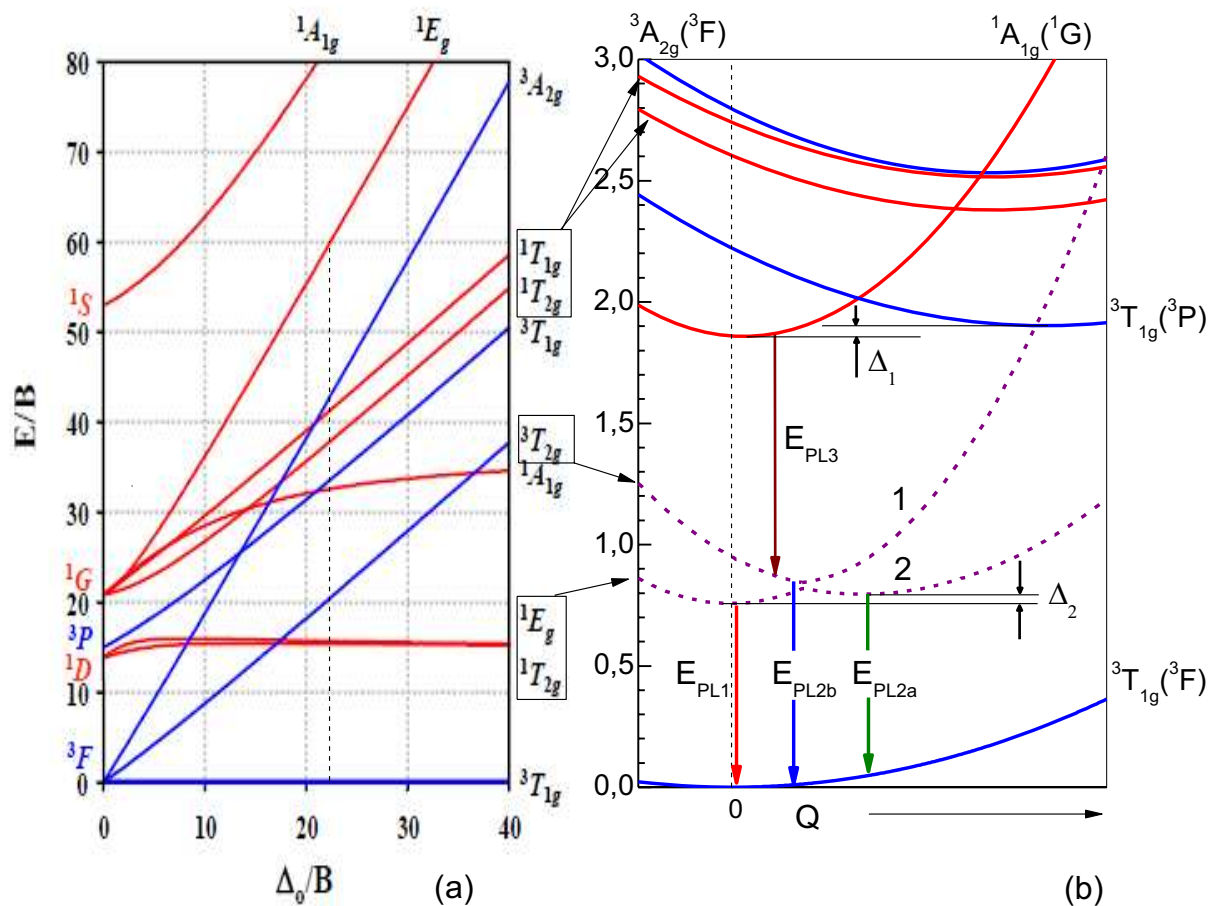


Fig. 3.11 a) Tanabe-Sugano diagram for d^2 octahedral configuration;
b) Single configuration coordinate diagram for V^{3+} ion in $\alpha\text{-ZnAl}_2\text{S}_4$ host crystal.

Fig. 3.11b shows the single configuration coordinate diagram for V^{3+} ions in $\alpha\text{-ZnAl}_2\text{S}_4$ spinel host, constructed using the spectroscopic data obtained above.

The upper level of the transition ${}^1A_{1g}({}^1G) \rightarrow {}^1T_{2g}, {}^1E_g({}^1D)$ responsible for E_{PL3} emission at excitation energies $\hbar\omega_{\text{ex}} > 2.5\text{eV}$ is partially populated due to the nonradiative transitions from the levels located higher than the ${}^3T_{1g}({}^3P)$ state. When the excitation takes place just in the E_{A3} absorption band, the intensity of the E_{PL3} component decreases (see Fig. 3.10) because the energetic barrier between the ${}^3T_{1g}({}^3P)$ and ${}^1T_{2g}, {}^1E_g({}^1D)$ levels is not high enough to prevent, even at low temperature, the nonradiative depopulation of the ${}^3T_{1g}({}^3P)$ state minimum in favour of the population of the ${}^1T_{2g}, {}^1E_g({}^1D)$ levels. However, due to the energetic barrier Δ_1 , at low temperature, the intensity of the E_{PL3} emission increases significantly and becomes comparable with that of the E_{PL2} component under the resonant excitation of the ${}^1A_{1g}({}^1G)$ term, i.e. in the region of E_{A1} band. When the temperature increases, the electrons, overcoming the Δ_1 -barrier, leave the ${}^1A_{1g}({}^1G)$ term in favour of the ${}^1T_{2g}, {}^1E_g({}^1D)$ and ${}^3T_{2g}({}^3F)$ terms.

The E_{PL1} component narrow lines can be ascribed to the spin-forbidden transitions ${}^1E_g, {}^1T_{2g}({}^1D) \rightarrow {}^3T_{1g}({}^3F)$, whereas the E_{PL2} component broad band – to the ${}^3T_{2g}({}^3F) \rightarrow {}^3T_{1g}({}^3F)$ spin-allowed radiative transitions, the ${}^3T_{2g}({}^3F)$ state being located upper than the ${}^1E_g({}^1D)$ one by the energy Δ_2 . But the fact that the E_{PL2} broad band coexist with E_{PL1} narrow lines even at lowest temperatures, when the thermal energy $k_B T$ is much less than the Δ_2 barrier value, suggests that the case of V^{+3} ions in $\alpha\text{-ZnAl}_2\text{S}_4$ is similar to that of Cr^{+3} ions in some garnet crystals [91-92], where due to the phonon-assisted tunnelling the mixing of the 4T_2 vibronic wave function with that of the 2E lowest state results.

Transition metal ions in ionic crystals interact strongly with lattice vibrations because of the spatial extent of the d -electron wavefunctions in the crystal. The motion of electrons is more rapid than that connected with lattice vibrations. Because of it, the electronic wavefunction in the adiabatic approximation [93] is assumed to vary only as a function of the coordinates R . The vibronic wavefunction $\Psi_j(r, R)$ of the Hamiltonian including electron-phonon interaction is written as the product of an electron wavefunction $\phi_j(r, R)$ and a nuclear vibrational wavefunction $\phi_{jl}(R)$ where subscripts j and l denote electron and phonon states, respectively. According to the authors of [91], the electron configurations of the excited states 2E and 4T_2 of Cr^{3+} are t^3_{2g} and $t^2_{g}e_g$, respectively. The 4T_2 state, which involves an e_g orbital, is strongly influenced by the lattice vibration because of σ -bonds with the s – and p – orbitals of the ligand ions. As a result, the electron – phonon interaction for the 4T_2 state is expected to be much larger than that of the 2E state.

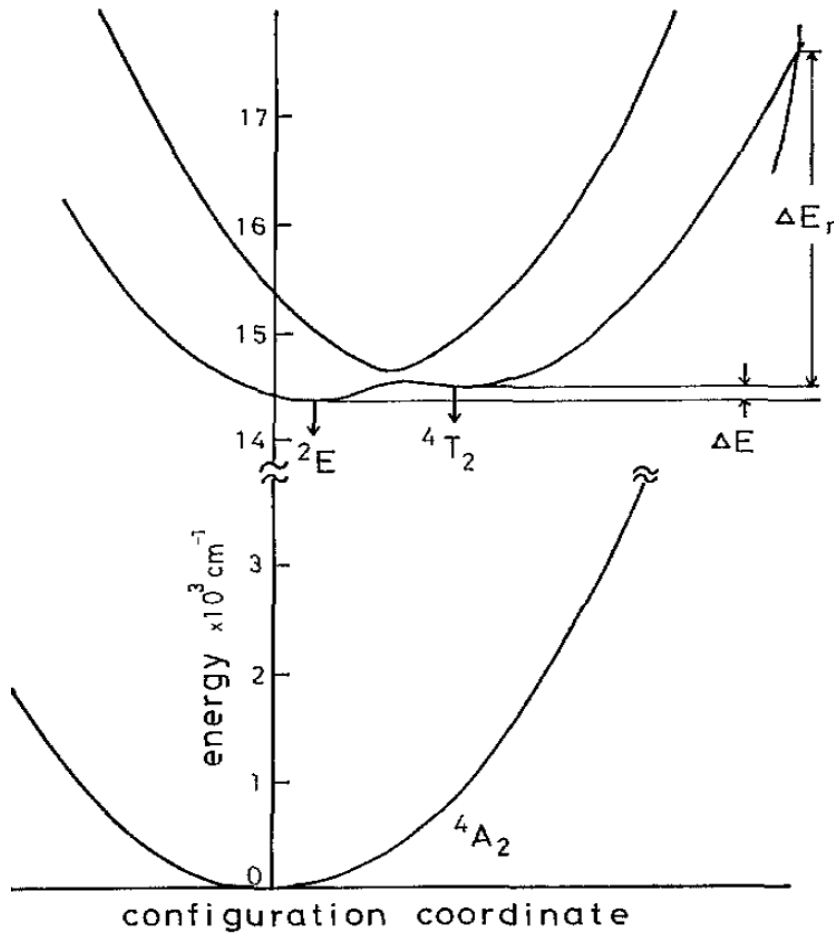


Fig. 3.12 Configuration coordinates diagram for the 2E and 4T_2 excited states for Cr^{3+} GSGG [91]

Fig. 3.12 shows the potential energy for the two different excited states 2E , 4T_2 and the ground state 4A_2 as a function of nuclear displacement for Cr^{3+} in GSGG[91]. At low temperatures, the barrier separating the excited 2E and 4T_2 states in Fig. 3.12 is lowered until it becomes comparable with the phonon energy, $\hbar\omega$. Tunnelling occurs between the two configurations through zero-point lattice vibrations, and a mixing of vibronic wavefunctions $\psi_E(r,R)$ and $\psi_T(r,R)$ of the excited states 2E and 4T_2 results. Due to that, a broad band emission from 4T_2 is observable at 1.6 K even when the thermal energy $k_B T$ is fairly small compared to the barrier height. The dashed curves in Fig. 3.11b have been drawn by analogy with the configuration diagram for Cr^{3+} ions in GSGG crystal garnet [91] and represent the adiabatic potentials for the mixed ${}^1E_g({}^1D)$ and ${}^3T_{2g}({}^3F)$ excited states of V^{3+} ion, with a higher and a lower levels resulted after the mixing (noted by 1 and 2, respectively, in Fig. 3.11 a and b).

Such configuration makes it possible to explain the coexistence of E_{PL1} and E_{PL2a} components at low temperatures ($k_B T \ll \Delta_2$) and the temperature behaviour of the $I(E_{PL2a})/I(E_{PL1})$ ratio, that looks similar to dependences observed for Cr^{3+} luminescence in garnet crystals [92]. Moreover, in the frame of the tunnelling model, the E_{PL2b} broad band,

which appears at $T > 150\text{K}$, can be ascribed to the radiative transition between the upper split potential of the ${}^3T_{2g}({}^3F)$ and ${}^1E_g({}^1D)$ mixed states and the ground state.

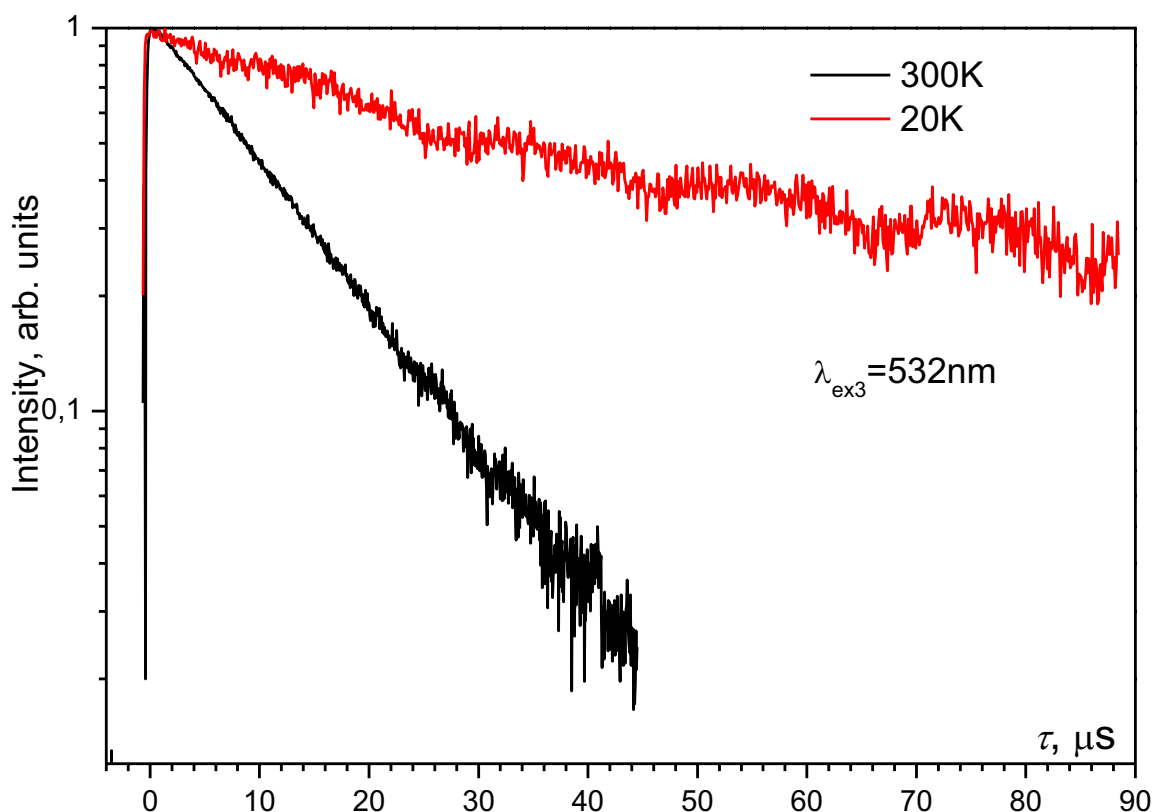


Fig. 3.13 Life-times of E_{PL2a} spectral component at two temperatures

In the case when the integral luminescence at low temperature would be provided only by the ${}^1E_g, {}^1T_{2g}({}^1D) \rightarrow {}^3T_{1g}({}^3F)$ spin-forbidden transition and at room temperature by the ${}^3T_{2g}({}^3F) \rightarrow {}^3T_{1g}({}^3F)$ spin-allowed transition, then the radiative life time should change its value by minimum an order of magnitude passing from the first transitions to the second one. However, as can be seen from Fig. 3.13, the radiative life time of the E_{PL2a} spectral component is decreasing only three times passing from low to room temperature. That clearly indicates that the E_{PL2a} component is presented even at low temperature, being enabled by the mechanism described above. Also, the E_{PL2a} lifetime seems to be the same whatever is the excited wavelength (see Fig. 3.14), which makes the mixing of ${}^1E_g, {}^1T_{2g}({}^1D)$ and ${}^3T_{2g}({}^3F)$ energy levels to be the only one from which E_{PL2a} and E_{PL1} components of the PL spectra occur. Moreover, due to this mixing there is no big difference between ${}^1E_g, {}^1T_{2g}({}^1D)$ and ${}^3T_{2g}({}^3F)$ lifetimes, in spite of the fact that the lifetime of the former should be of the order of μs .

In order to describe the temperature dependence of the PL decay, a simplified two-level kinetic model was used, assuming that three excited levels ${}^1E_g, {}^1T_{2g}({}^1D)$ and ${}^3T_{2g}({}^3F)$ are in quasithermodynamic equilibrium, and that the radiationless transitions to the ground state can be neglected.

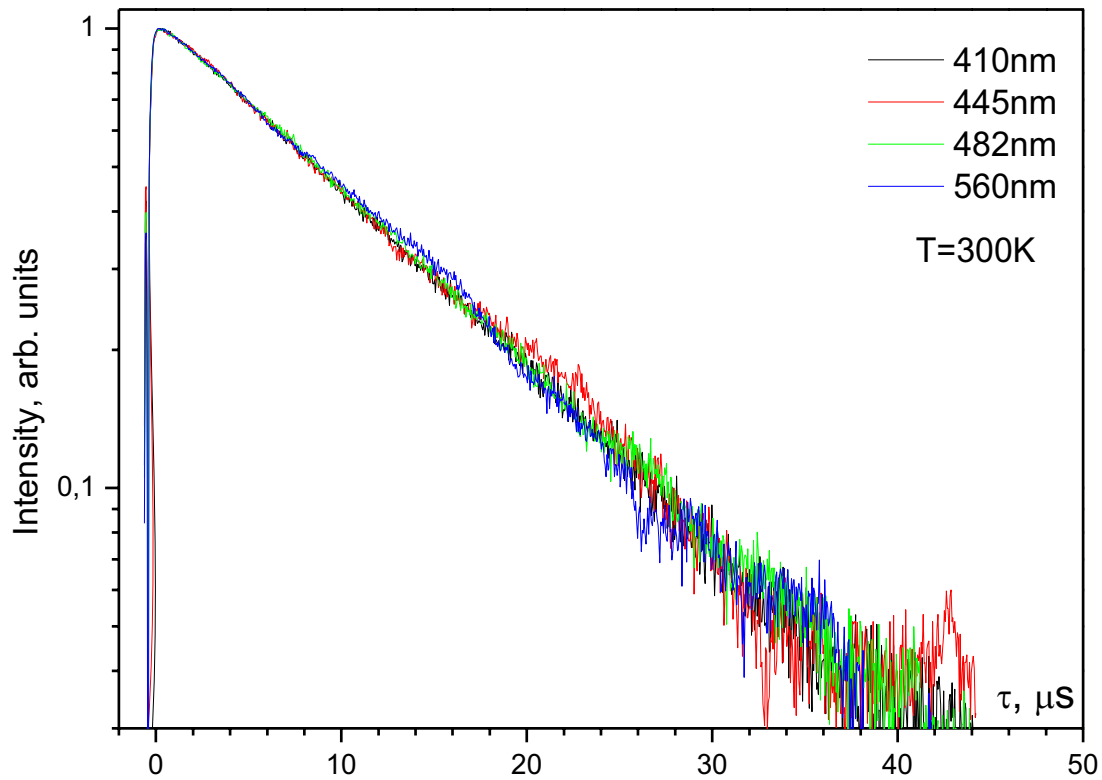


Fig. 3.14 Life-times of E_{PL2a} spectral component under different excitations at room temperature

Indeed, according to the model of the configurational coordinate diagram presented in Fig. 3.11a and b, the change of the total population of ${}^1E_g, {}^1T_{2g}({}^1D)$ and ${}^3T_{2g}({}^3F)$ levels, n is described by the rate equation:

$$\frac{dn}{dt} = -\left(\frac{1}{\tau_{R1}}\right)n_1 - \left(\frac{1}{\tau_{R2}}\right)n_2 \quad (3.5)$$

where n_1 , $1/\tau_1$ and n_2 , $1/\tau_2$ are the population and the radiative rate of ${}^1E_g, {}^1T_{2g}({}^1D)$ and ${}^3T_{2g}({}^3F)$ levels, respectively. The total population is described by the relation:

$$n = n_1 + n_2 \quad (3.6)$$

and the redistribution of the population between the two levels involved occurs according to:

$$n_2 = C_d n_1 e^{-\frac{\Delta E}{kT}} \quad (3.7)$$

where ΔE is the energetic barrier between the upper – 1 and lower – 2 levels of the mixing of ${}^1E_g, {}^1T_{2g}({}^1D)$ and ${}^3T_{2g}({}^3F)$ levels, k is the Boltzmann constant, T is the temperature and C_d is the degeneracy of the ${}^3T_{2g}({}^3F)$ level relative to the ${}^1E_g, {}^1T_{2g}({}^1D)$ levels. Thus taking into account the last equations the population of the each level can be rewritten as:

$$\begin{aligned}
n &= n_1 + C_d n_1 e^{\frac{\Delta E}{kT}} \Rightarrow n_1 = \frac{n}{1 + C_d e^{\frac{\Delta E}{kT}}} \\
n &= n_2 + \frac{n_2}{C_d e^{\frac{\Delta E}{kT}}} \Rightarrow n_2 = \frac{n C_d e^{\frac{\Delta E}{kT}}}{1 + C_d e^{\frac{\Delta E}{kT}}}
\end{aligned} \tag{3.8}$$

So, Equation (3.5) takes the following form:

$$\begin{aligned}
\frac{dn}{dt} &= -\left(\frac{1}{\tau_{R1}}\right) \frac{n}{1 + C_d e^{\frac{\Delta E}{kT}}} - \left(\frac{1}{\tau_{R2}}\right) \left(\frac{C_d e^{\frac{\Delta E}{kT}}}{1 + C_d e^{\frac{\Delta E}{kT}}}\right) n \\
\frac{dn}{dt} &= -\frac{\left(\frac{1}{\tau_{R1}}\right) + \left(\frac{1}{\tau_{R2}}\right) C_d e^{\frac{\Delta E}{kT}}}{1 + C_d e^{\frac{\Delta E}{kT}}} n
\end{aligned} \tag{3.9}$$

Thus the radiative lifetime for the mixing described above, according to (3.9), is defined as:

$$\begin{aligned}
\tau &= \frac{1 + C_d e^{\frac{\Delta E}{kT}}}{\left(\frac{1}{\tau_{R1}}\right) + \left(\frac{1}{\tau_{R2}}\right) C_d e^{\frac{\Delta E}{kT}}} \\
\text{or} \\
\tau &= \tau_{R1} \frac{1 + C_d e^{\frac{\Delta E}{kT}}}{1 + \left(\frac{\tau_{R1}}{\tau_{R2}}\right) C_d e^{\frac{\Delta E}{kT}}}
\end{aligned} \tag{3.10}$$

Knowing the radiative lifetime of luminescence, Equation (3.10) can be fitted in order to find the τ_1 , τ_2 , and ΔE values.

Fig. 3.15 presents the values for the radiative lifetime of E_{PL2a} spectral component of luminescence under $\lambda_{ex3}=532\text{nm}$ at different temperatures fitted curve according to Equation (3.10). The experimental values for the lifetimes of the excited levels and the Δ_2 energies, obtained from a fit of the $\tau(T)$ dependence over the whole temperature range are $\tau_1=31\ \mu\text{s}$, $\tau_2=3.8\ \mu\text{s}$ and $\Delta E=60\text{meV}$. At first appearance the energetic barrier value is high enough to prevent the population of the upper level – 1 of the mixing, however taking into account that the phonon energy is $\approx 40\text{meV}$, the ΔE value seems to be reasonable and corresponds to the temperature $T=200\text{K}$. Indeed, the PL intensity increases drastically starting with this temperature as can be seen from the Fig. 3.8 and Fig. 3.9.

The quantum efficiency of the PL spectrum can be easily expressed in term of radiative and nonradiative lifetimes:

$$\eta = \frac{W_R}{W_R + W_{NR}} = \frac{\frac{1}{\tau_R}}{\frac{1}{\tau_R} + \frac{1}{\tau_{NR}}} = \left(1 + \frac{\tau_R}{\tau_{NR}}\right)^{-1} \quad (3.11)$$

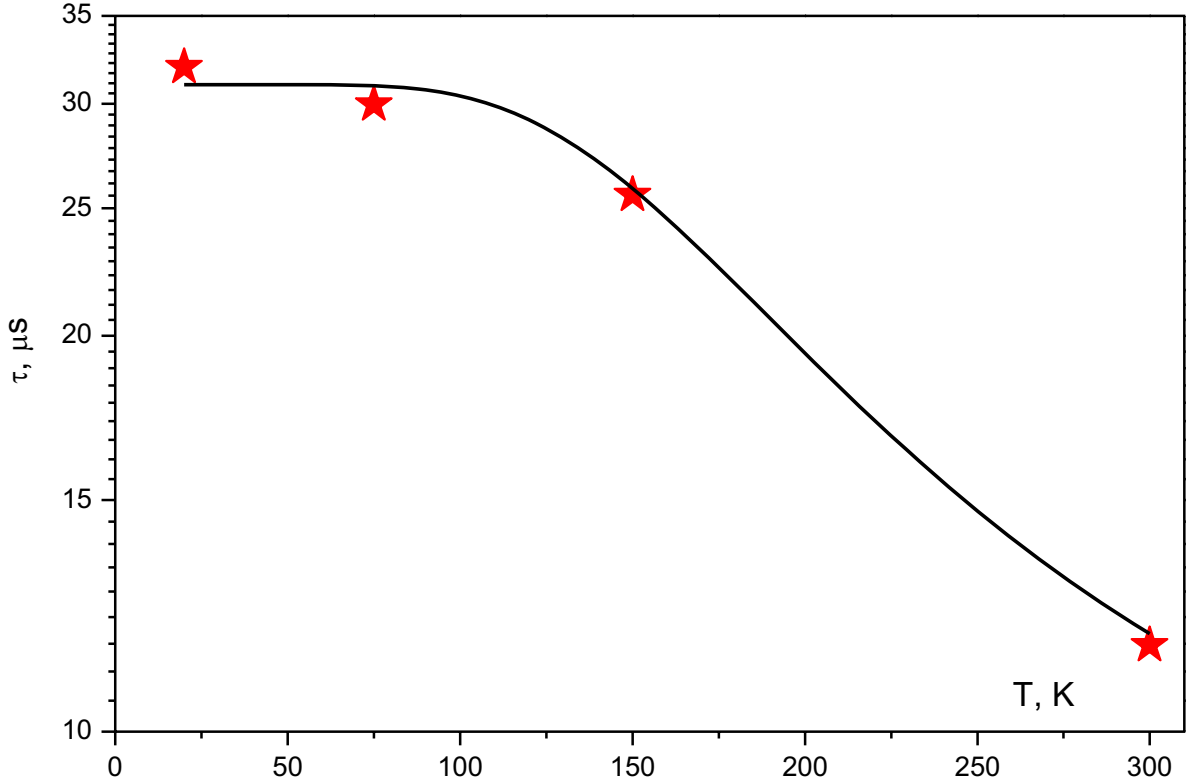


Fig. 3.15 Lifetimes of the E_{PL2a} spectral component under $\lambda_{ex3}=532\text{nm}$ at different temperature (star point). The solid line represents the least square fits to the (3.10) equation.

Thereby, the substitution of the τ_R with the corresponding formula from (3.10) allows to fit the temperature dependence of the PL integral intensity (see Fig. 3.9); the fitted parameters being the same as for the lifetime fitting process with the appearance here of a new parameter – the nonradiative lifetime τ_{NR} .

The fitting of the integral PL spectrum dependence on temperature has been done using the formula (see also Fig. 3.16):

$$\eta = \left(1 + \frac{\tau_R}{\tau_{NR}}\right)^{-1} = \left(1 + \frac{\tau_{R1} \frac{1 + C_d e^{-\frac{\Delta E}{k} T}}{1 + \left(\frac{\tau_{R1}}{\tau_{R2}}\right) C_d e^{-\frac{\Delta E}{k} T}}}{\tau_{NR}}\right)^{-1} \quad (3.12)$$

So, the parameters obtained after fitting are $\tau_1 = 35 \mu\text{s}$, $\tau_2 = 3.1 \mu\text{s}$ and $\Delta E = 50\text{meV}$ and $\tau_{NR} = 1.6 \mu\text{s}$. It has to be mentioned here that the obtained parameter values are very close to those obtained after the fitting of the temperature dependence of the radiative lifetime, i.e. the fitted

parameters obtained from two independently measurements are very similar, which indicates that they are correctly determined.

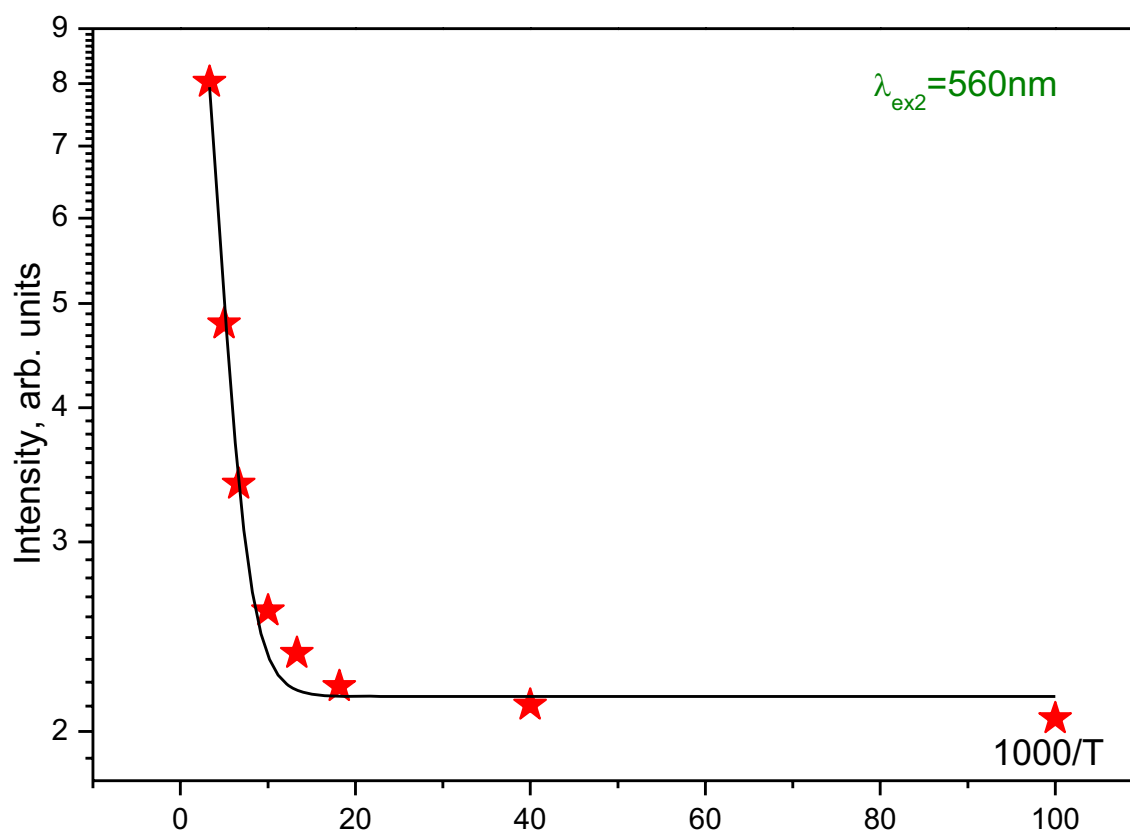


Fig. 3.16 Temperature dependence of the integral PL intensity of α -ZnAl₂S₄:V.

The solid line represents the least square fits to equation (3.12).

Perhaps the absence of a band related to the ${}^3T_{1g}({}^3F) \rightarrow {}^3T_{2g}({}^3F)$ optical transitions in the absorption spectrum may be interpreted as a consequence of the ${}^3T_{2g}({}^3F)$ and ${}^1E_g({}^1D)$ states mixing, as above. In spite of the fact that this transition is spin- and electric quadrupole-allowed and should appear as a prominent absorption band, all attempts to reveal it have been unsuccessful. In some cases such transitions are manifested better in the *PL* excitation spectra, as is the case of A_0 band for t - α -ZnAl₂S₄:Ti⁴⁺, which appears only in the excitation spectrum (see Chapter IV). However, under excitation using $\lambda_{\text{ex5}}=1064\text{nm}$ (1.164eV) and $\lambda_{\text{ex6}}=1152\text{nm}$ (1.075eV), i.e. in the energy region for the ${}^3T_{1g}({}^3F) \rightarrow {}^3T_{2g}({}^3F)$ expected transitions, there was not observed any emission.

3.4 Conclusions

- The absorption spectrum of α -ZnAl₂S₄:Co crystals measured at room temperature, composed of three components located at 0.77eV ($E_{A1} \approx 6450 \text{ cm}^{-1}$, quadruplet), 1.60eV ($E_{A2} \approx 12990 \text{ cm}^{-1}$, triplet) and 2.58eV ($E_{A3} \approx 20160 \text{ cm}^{-1}$, broad band) is determined by the electronic transitions of Co²⁺ ions located in tetrahedral sites. The values of the spin-orbit coupling constants of first two components found to be 189 and 321 cm⁻¹, respectively, indicate a weak crystal field influence and a strong spin-orbit coupling.
- It has been shown that the luminescence of α -ZnAl₂S₄:Co crystals is due to the electronic transitions between the excited levels of the Co²⁺ ions. Four radiative spectral components have been revealed using the time-resolved spectroscopy at different excitation wavelengths ($\lambda = 496, 532$ and 700 nm). The fastest E_{PL1} narrow lines located in the spectral range 1.42 - 1.51eV are ascribed to the transition from the ${}^2A({}^2G)$ short life-time level to the lower excited triple degenerated ${}^4T_1({}^4F)$ state; the narrow line at $E_{PL3} = 1.122\text{eV}$ is attributed to the transition ${}^4T_1({}^4P) \rightarrow {}^4T_2({}^4F)$; the two broad bands centred at $E_{PL2} = 1.32\text{eV}$ and $E_{PL4} = 0.96\text{eV}$ with a slow decay, are ascribed to the partially forbidden transitions ${}^2E({}^2G) \rightarrow {}^4T_2({}^4F)$ and ${}^2E({}^2G) \rightarrow {}^4T_1({}^4F)$, respectively.
- The absorption and luminescent properties of α -ZnAl₂S₄:V crystals are the result of electronic transitions of trivalent vanadium ions located in octahedral sites. The three main spectral components of α -ZnAl₂S₄:V IR luminescence – $E_{PL1} \approx 0.75\text{eV}$, $E_{PL2} \approx 0.9\text{eV}$ and $E_{PL3} \approx 1.05\text{eV}$ revealed at low temperatures are caused, respectively, by the ${}^1E_g({}^1D) \rightarrow {}^3T_{1g}({}^3F)$; ${}^3T_{2g}({}^3F) \rightarrow {}^3T_{1g}({}^3F)$, and ${}^1A_{1g}({}^1G) \rightarrow {}^1E_g({}^1D)$, ${}^1T_{2g}({}^1D)$ electronic transitions of the V³⁺ ions. The coexistence of the E_{PL2} broad band with E_{PL1} narrow lines at low temperatures, when the thermal energy $k_B T$ is much less than the height of the potential barrier between the ${}^3T_{2g}({}^3F)$ and ${}^1E_g({}^1D)$ excited states, is explained assuming that there is a phonon assisted tunnelling between these two states.
- It has been found that the rise of temperature leads to the enhancement of the integral luminescence intensity and to the broadening of the spectrum centered at $\lambda = 1.4\mu\text{m}$, due to the ${}^3T_{2g}({}^3F) \rightarrow {}^3T_{1g}({}^3F)$ vibronic transitions which suppress other emission channels.
- Taken together, the results obtained on the base of comparative analysis of the spectroscopic properties of α -ZnAl₂S₄ spinel type crystals doped with transition metals Ti, Co, and V suggest that α -ZnAl₂S₄:V³⁺ compound is the most appropriate for applications as active media for solid state IR-lasers tunable in the 1.2-1.6 μm wavelength range that corresponds to the spectral region used in the fibre-optics communication systems.

4. SPECTROSCOPIC CHARACTERIZATION OF Ti-DOPED α -ZnAl₂S₄ SPINEL TYPE SINGLE CRYSTALS

4.1. Introduction

Recently, there has been considerable interest in titanium doped crystals as the active media for solid-state lasers. Besides the well known Ti-sapphire (Al₂O₃:Ti) [11] there are several crystalline hosts where titanium ions manifest broad band luminescence in the near IR and visible regions [25-26]. The spectroscopic properties of Ti impurity in MgAl₂O₄ spinel host crystal have been investigated in [27-29], and blue emission with strong intensity has been detected. Meanwhile, the interpretation of spectroscopic properties of different oxides doped by titanium is not straightforward. The simultaneous presence of Ti³⁺ and Ti⁴⁺ ions in the host is a matter of some difficulty. The authors in [12] have found out that the absorption spectrum of Ti³⁺:Al₂O₃ crystals consists of the main blue-green absorption band and a weak infrared band. The intensity of the IR absorption decreases on annealing in a reducing atmosphere. Combined optical and EPR studies allowed to assume that the center associated with the red band is a cluster involving Ti³⁺ and Ti⁴⁺, with a neighbouring charge compensating Al³⁺ vacancy. A similar problem to that observed with Ti³⁺:Al₂O₃ has been reported for Ti³⁺:YAlO₃, wherein a broad absorption is observed around 950 nm in addition to the normal visible absorption bands at 434 and 492 nm [14]. Two types of Ti⁴⁺ in Al₂O₃ (locally and nonlocally charge compensated) have been identified optically in [13]. The lifetimes of the charge-transfer emission as a function of temperature have been well explained by a three-level scheme with a lower triplet excited state and a higher singlet excited state. The presence of Ti⁴⁺ occupying the Al³⁺ site in the spinel host has been confirmed in [30]. As in [12-14], the mechanism proposed in [30] is based on the assumption of a charge-transfer excitation from O²⁻ (*2pσ*) into the empty (3d)-orbital of Ti⁴⁺, resulting in Ti³⁺ in the electronic excited state with a subsequent emission of a photon from this titanium 3d-state stabilized by the interaction with lattice vibrations.

In the vein to obtain room-temperature IR sources of radiation, the spectral properties of titanium doped chalcogenides have been also intensively studied by many authors along with titanium doped oxide compounds. In earlier publications absorption, photoconductivity and the Hall measurements are reported on CdS [15-18] and CdSe [17, 19-20]. In particular, strong Ti²⁺ absorption bands determine the energies of the two prominent transitions from ³A₂(³F) to ³T₁(³F) and ³T₁(³P) levels. A very weak absorption is also detected in both materials with maxima at about 3100 cm⁻¹ in CdSe [20] and 3320 cm⁻¹ in CdS [16]. This

absorption has been assigned to the transition ${}^3A_2({}^3F) \rightarrow {}^3T_2({}^3F)$ which is forbidden in T_d symmetry. An EPR investigation of the hyperfine interactions with ligand nuclei of the Ti^{2+} centre in single crystals of hexagonal CdS and CdSe on sites with trigonal C_{3v} symmetry has been undertaken in [21-22]. The experimental data obtained in [21] show that no change of the EPR spectra could be observed under irradiation of CdS: Ti^{2+} with light in the spectral region 400 to 800 nm. An irradiation with light of longer wavelengths results in a strong quenching and a line broadening of the EPR signal. The maximum quenching of the EPR spectrum was found to correspond with the maximum of the photoconductivity. The observed effect was explained by the depopulation of the 3A_2 term through the transitions to the excited levels that are in the conduction band of CdS. The authors in [23] used the EPR to detect the ground states of Ti^{2+} and Ti^{3+} , indicating a substitutional incorporation of Ti ions into Cd-sites in CdS, CdSe and Cd(S,Se) crystals. For the first time [23], the Jahn-Teller ion Ti^{3+} was observed by its ${}^2T_2 \rightarrow {}^2E$ transition in photoluminescence. Optical and paramagnetic properties of titanium centres in ZnS were examined in [24] and it was shown that Ti^{2+} ion on a cubic site presents an isotropic EPR signal with $g=1.928$ observable up to 80 K. Signals of Ti^{2+} ions on axial sites were detected in the same temperature range. In [24] it was also demonstrated that in emission Ti^{2+} ion exhibits the ${}^3T_2({}^3F) \rightarrow {}^3A_2({}^3F)$ transition, structured by no-phonon lines of centres in various environments. The prominent line at 3613cm^{-1} in the emission spectrum was assigned to the centre with the T_d symmetry, while the lines at 3636 , 3634 and 3632cm^{-1} were assumed to originate from the impurity centres in various trigonally distorted environments as corroborated by the EPR data.

Thus, the Ti- doped systems demonstrate interesting peculiarities of their spectroscopic properties due to the possibility to embed Ti ions with different oxidation degrees into the host crystal. In some cases the simultaneous presence of impurity Ti^{2+} and Ti^{3+} ions can be observed [24]. To sum up, all of the above cited papers deal with titanium doped chalcogenides or oxides. In this chapter for the first time the case of titanium doped α - $ZnAl_2S_4$ crystals is addressed, with Ti ions in octahedral sulphur surrounding.

4.2. Experimental results

Bulk stoichiometric α - $ZnAl_2S_4$:Ti crystals with impurity concentration 0.05-0.5 at.% were grown by a closed tube vapour method with halogen as a transport agent, as was described in chapter 2. The samples represented optically homogeneous octahedra with volumes up to 30 mm^3 and (111) oriented mirror like faces that were used directly for photoluminescence experiments, coloured from brown to dark-brown in dependence of the

concentration. For optical absorption and luminescence measurements, some crystals were cut and polished in order to obtain flat parallel faces.

At temperatures $T=10-300\text{K}$ the studies of the steady-state and time-resolved photoluminescence (*PL*) spectra, as well as of the PL excitation (*PLE*) and absorption spectra were performed in the spectral range $0.4-1.5\ \mu\text{m}$ using a liquid nitrogen cooled Ge-detector or photomultiplier. The EPR studies of the samples were carried out as well.

The optical density spectra at room temperature for three different thicknesses of $\alpha\text{-ZnAl}_2\text{S}_4\text{:Ti} - 0.1\ \text{at.}\%$ single crystal are presented in Fig. 4.1. The shift of the spectral edge of different samples towards the high energies is due to the difference in the thickness of the samples: $d_1=0.12\ \text{mm}$, $d_2=0.72\ \text{mm}$ and $d_3=1.12\ \text{mm}$. This behaviour of the optical density spectra is due to that fact the method of the optical density measurement is quite sensible to the thickness of the sample: the thinner is the samples, the less are the loses on the scattering on the bulk defects, absorption on the colour centres and impurities others than those studied. In addition, the decrease of thickness leads to the reduction of absorbing centres – in this way, the absorption intensity is reduced, which results in the appearances of the impurity absorption bands, as is the case of the A_2 absorption band or the A_1 band.

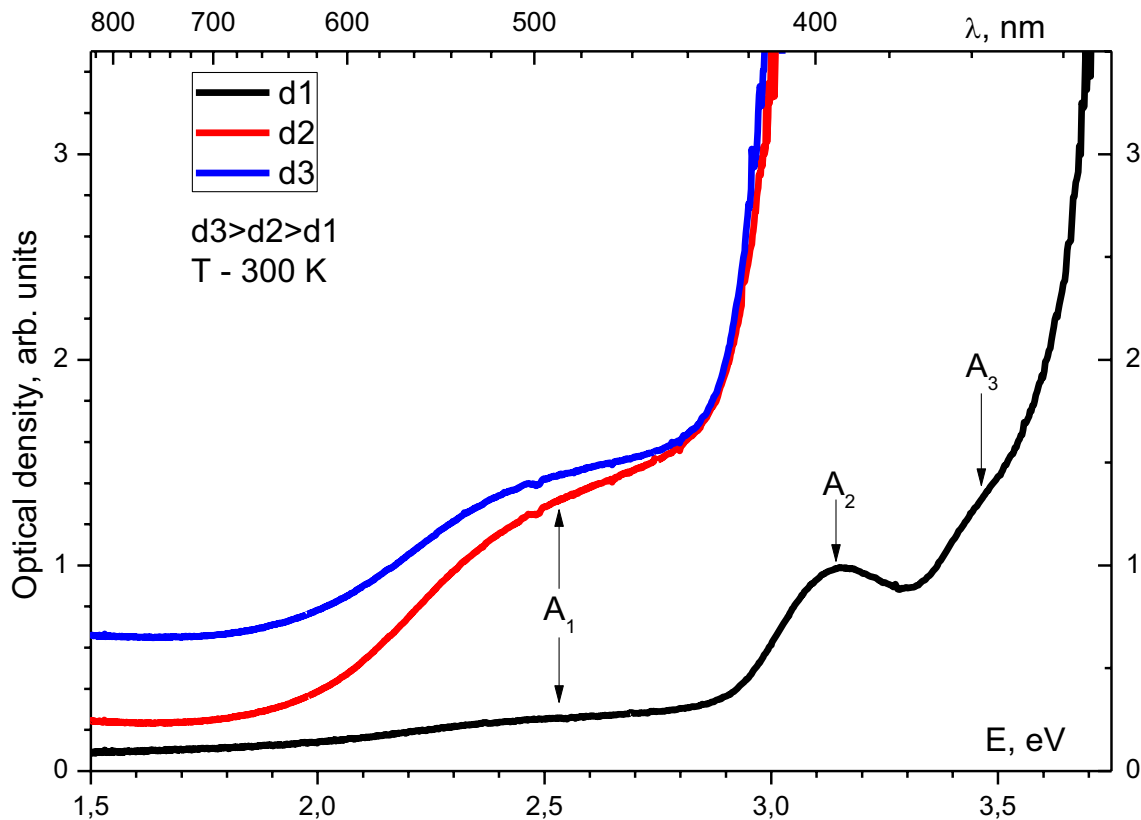


Fig. 4.1 Absorption spectrum at room temperature for three thickness of $\alpha\text{-ZnAl}_2\text{S}_4\text{:Ti} - 0.1\ \text{at.}\%$ single crystal

Thus the best optical density spectra were achieved on the samples with the thickness d_1 . The room temperature optical absorption spectrum (Fig. 4.2) consists, at least, of three

broad bands centred at $E_{A3}=3.4\text{eV}$, $E_{A2}=3.1\text{eV}$ and $E_{A1}=2.4\text{eV}$ which can be attributed to the Ti impurity.

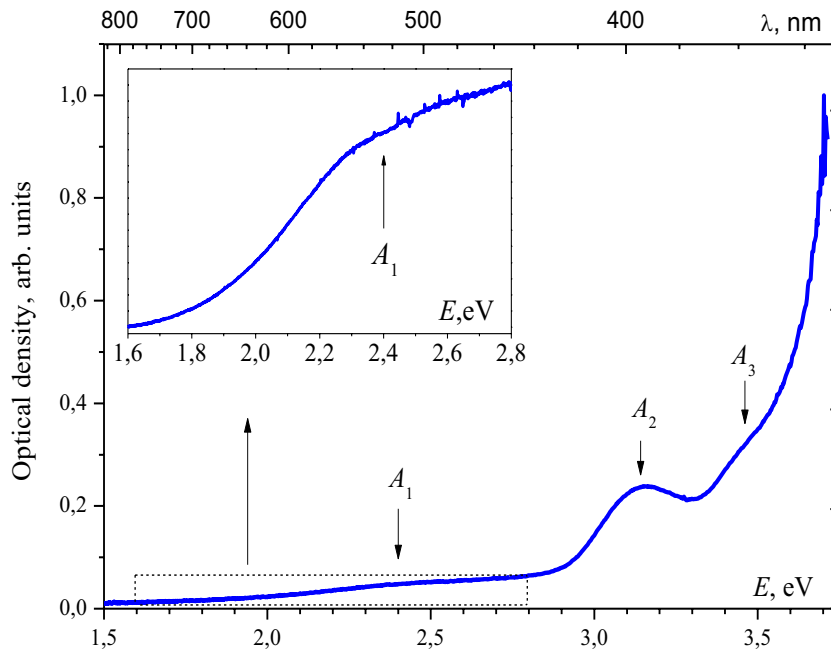


Fig. 4.2 Absorption spectrum at room temperature of $\alpha\text{-ZnAl}_2\text{S}_4\text{:Ti} - 0.1$ at.% single crystal for $d1$ thickness.

The spectral edge observed at 3.6eV corresponds to the host crystal intrinsic absorption [83, 94]. The absorption coefficient spectrum was calculated using the Formula (2.14) and the spectrum is presented in Fig. 4.3. This wavelength dependence of the intensity of the absorption coefficient fits in the normal values for the transition metals doped spinels and does not exceed 50 cm^{-1} [85].

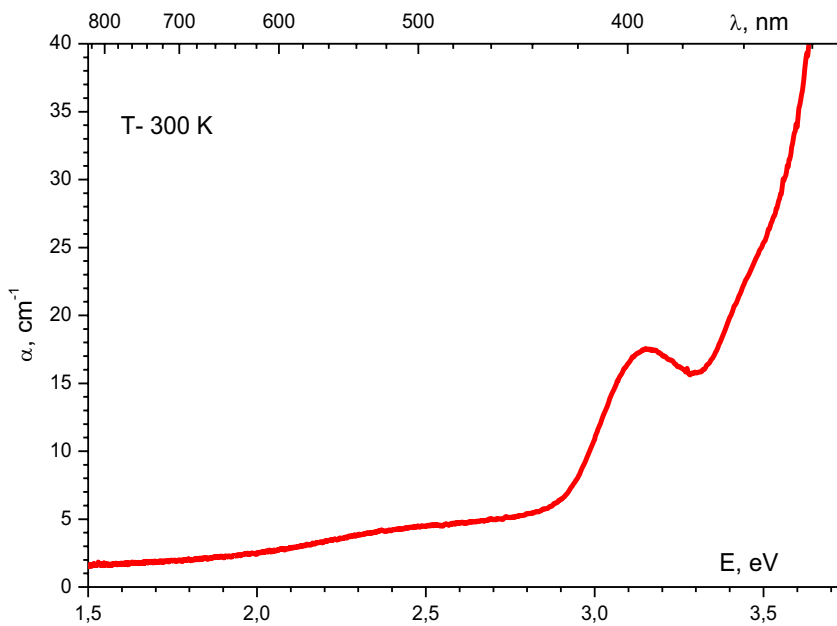


Fig. 4.3 The absorption coefficient spectrum of $\alpha\text{-ZnAl}_2\text{S}_4\text{:Ti} - 0.1$ at.% single crystal

In order to provide the selective excitation of the impurity, the steady state *PL* spectra were measured using, as excitation sources, the Ar⁺ laser operating at $\lambda_{exG}=514\text{nm}$ (“green” excitation, $E_{exG}=2.41\text{eV}\approx E_{A2}$) and He-Ne laser (“red” excitation, $\lambda_{exR}=633\text{nm}$).

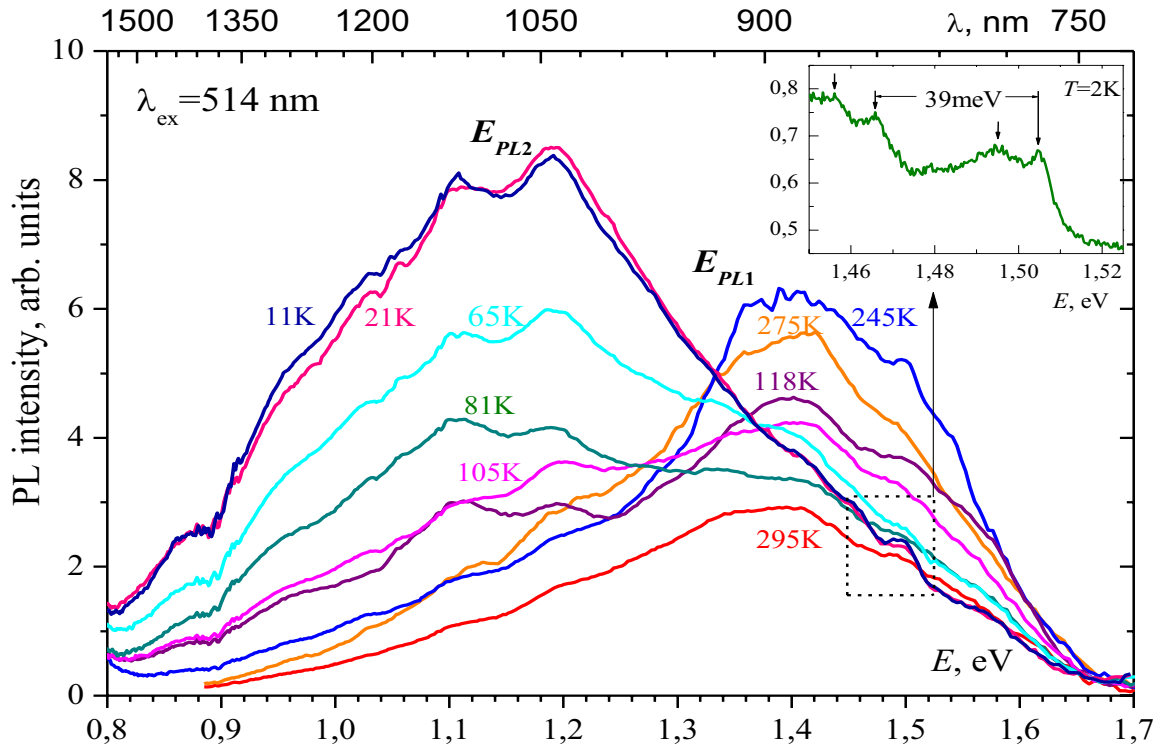


Fig. 4.4 Emission spectra under "green" excitation at different temperatures.

Under “green” excitation, an unusual behaviour of the steady-state *PL* spectra of ZnAl₂S₄:Ti - 0.1 at % crystals is revealed: these consist of two broad bands centred at $E_{PL1}=1.41\text{eV}$ and $E_{PL2}=1.19\text{eV}$ whose intensity is redistributed with temperature (Fig. 4.4).

The second component E_{PL2} dominates in the spectrum at low temperatures ($T<80\text{K}$). At the rise of temperature, the redistribution of intensities occurs but at about 80K the peak intensities of the bands differ insignificantly. Beginning from $T\approx 100\text{K}$ the height of the band at 1.41eV exceeds that corresponding to the band at 1.19eV. At temperatures close to 300K, the shape of the integral spectrum is practically determined by the first broad band E_{PL1} . The maximum of this band at room temperature is located at 1.4eV. At excitation with the wavelength of $\lambda_{exR}=633\text{nm}$, the main contribution to the *PL* spectra in the whole temperature range is provided by the component at $E_{PL1}=1.41\text{eV}$ (Fig. 4.5). It is worth noting that at room temperature the spectra obtained under “red” and “green” excitations have practically the same shape and peak position. Besides, it has to be mentioned that the intrinsic *PL* of the undoped samples [31], excited by the 248 nm (5eV) line of a KrF excimer laser, has shown an ultraviolet spectral peak at 3.25eV (296K).

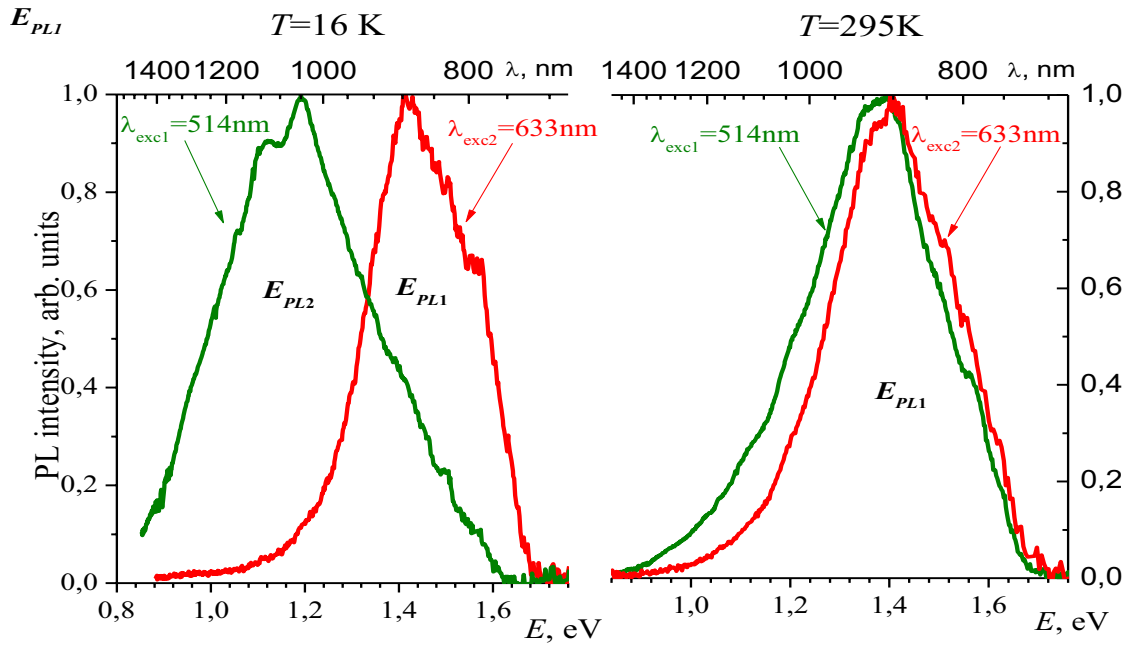


Fig. 4.5 PL spectra under "green" and "red" excitations at low and room temperatures.

The time resolved *PL* spectra measured under pulsed excitation with wavelengths: "green" - $\lambda_{excGP}=532\text{nm}$ are presented in Fig. 4.6.

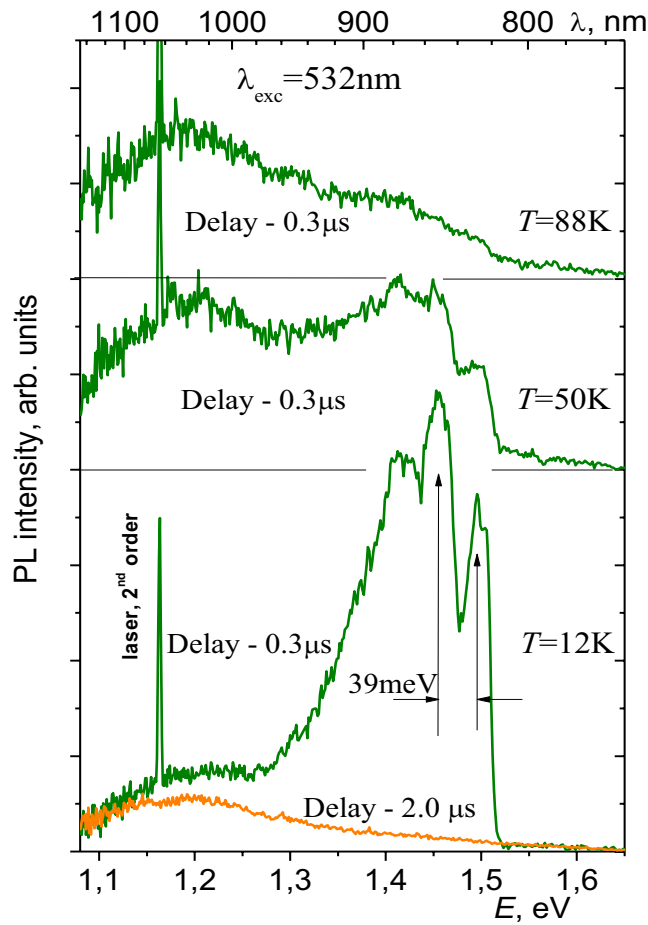


Fig. 4.6 Time resolved PL spectra under "green" pulsed excitation

At “green” pulsed excitation, three relatively sharp spectral lines located at $E_{PL3a}=1.45\text{eV}$, $E_{PL3b}=1.49\text{eV}$ ($E_{PL3b}-E_{PL3a}=39\text{meV}$) and $E_{PL3c}=1.505\text{eV}$ are revealed. These lines disappear in a very short time (less than $\sim 1\mu\text{s}$) after the exciting pulse (time resolution $\sim 0.1\mu\text{s}$) and can be observed only at low temperatures ($T < 90\text{K}$). Under “red” pulsed excitation – $\lambda_{exRP}=630\text{nm}$ (close to λ_{exR}) this sharp lines emission does not arise. It should be noted that the E_{PL3} components can be also observed at low temperatures as a small feature on the short wavelength shoulder of the steady-state PL spectra obtained at “green” excitation (Fig. 4.4, insert).

The kinetics was registered at different temperatures under pulsed excitation practically at the same wavelengths as the PL spectra: $\lambda_{ex}=532\text{ nm}$ and $\lambda_{ex}=633\text{ nm}$ Fig. 4.7. The kinetics excited by the last one was registered for the E_{PL1} maximum and obeys the exponential law with a single decay time which is decreasing with the rise of temperature.

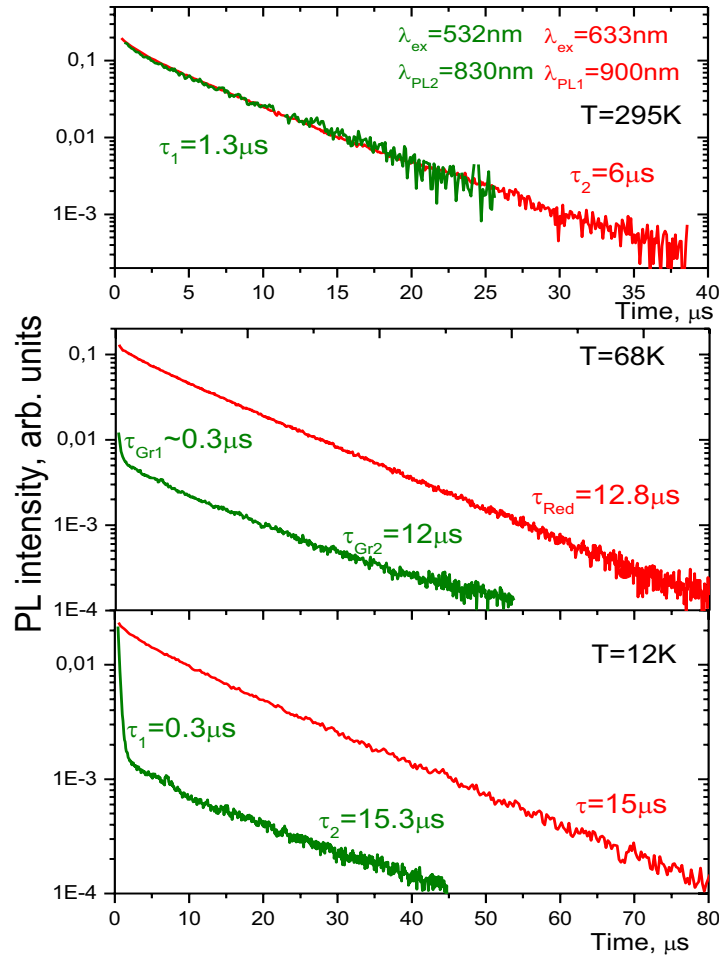


Fig. 4.7 Luminescence kinetics under $\lambda_{ex}=532\text{ nm}$ and $\lambda_{ex}=633\text{ nm}$ excitation at different temperatures.

In contrast to the previous, the emission decay of the E_{PL2} by $\lambda_{ex}=532\text{nm}$ excitation can be described by the superposition of two exponents with different lifetimes: one very fast component τ_1 that disappears at temperatures above 100 K and the main component τ_2 that decreases with the rise of temperature.

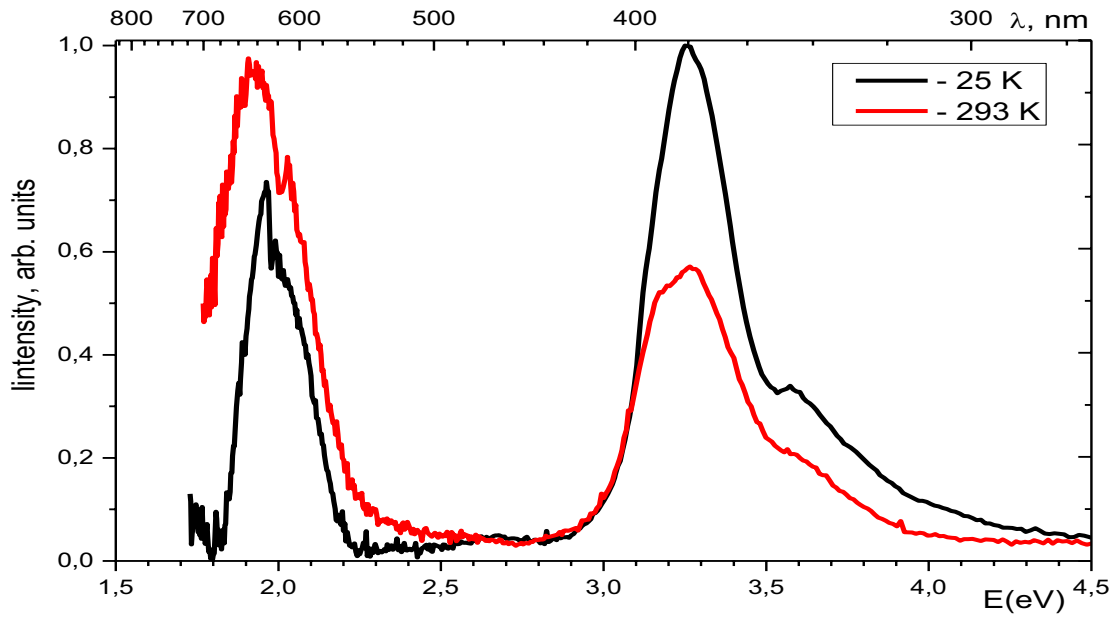


Fig. 4.8 Excitation spectra for α -ZnAl₂S₄:Ti – 0.1 at.% single crystal at two temperatures

The PLE spectra were registered at different temperatures for the spectral range (860 – 900) nm, approximately in the E_{PL1} maximum (Fig. 4.8). There are two prominent peaks at 1.9eV and 3.35eV whose intensity is changing with temperature: with the rise of temperature, the intensity of the first one is increasing relative to the intensity of the second one, at low temperature – vice versa.

The plotting of the absorption density spectrum and excitation spectrum on the same graphic reveals some peculiarities (Fig. 4.9).

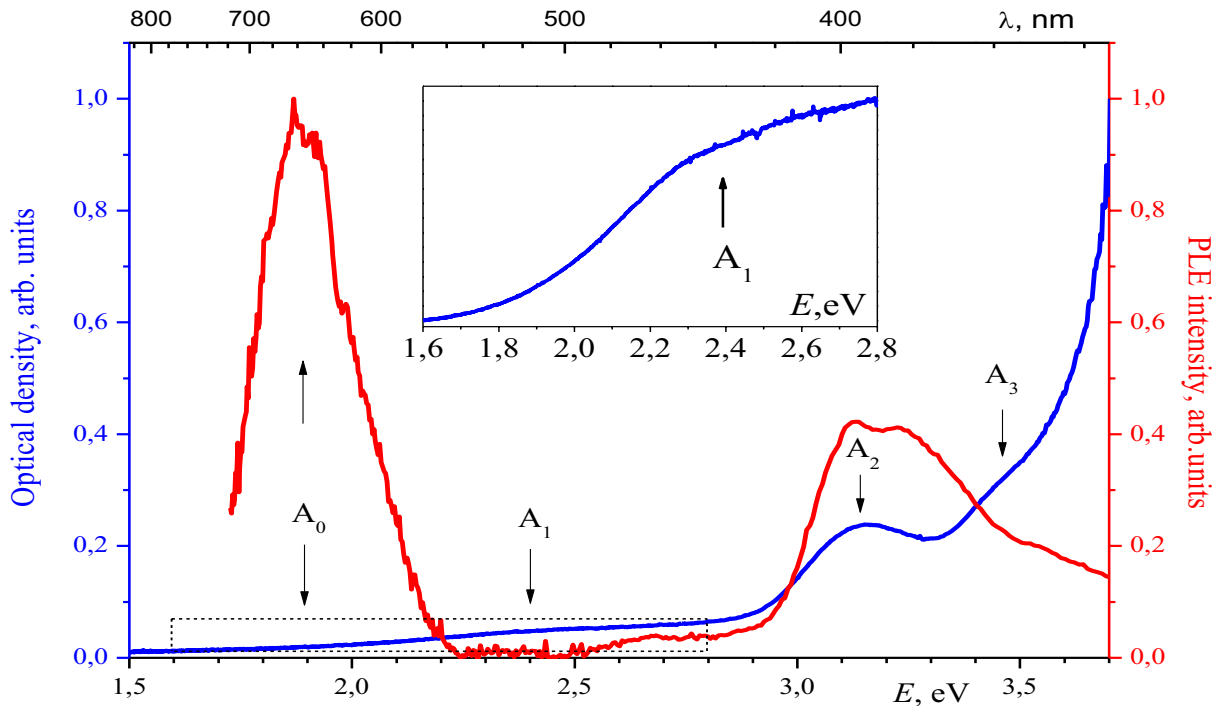


Fig. 4.9 Absorption and PLE spectra of α -ZnAl₂S₄:Ti single crystal.

First of all, the absorption bands A_3 , and A_2 are presented in both spectra; however, the fundamental absorption band at 3.6eV gives no contribution in the excitation spectra and thus the above enumerated bands seem to appertain only to the Ti impurity centres. The A_1 absorption band is not detectable in the *PLE* spectrum, instead the presence of the excitation band at 1.9eV – the A_0 band should be mentioned, which is not detectable in the optical density spectrum.

4.3. Theory and interpretation of the experimental data

In order to explain the observed spectra transformations the results of the EPR measurements were employed which apparently show that the Ti- impurity is EPR silent in α - $ZnAl_2S_4$ crystals. This allows drawing a conclusion that there is no Ti^{3+} and Ti^{2+} valence states. Otherwise, as in papers [21-24] dealing with impurity titanium ions in sulphur surroundings (see Introduction), an EPR signal should be observed. Spectroscopic data on impurity $CdS:Ti^{2+}$ and $CdSe:Ti^{2+}$ systems [16, 20] show three absorption bands in the range of approximately 9000, 5000 and 3000 cm^{-1} . However, in the absorption spectra of the examined $ZnAl_2S_4:Ti$ compound the bands are located at 19360, 25000 and 27424 cm^{-1} and cannot be attributed to Ti^{2+} ions. In ZnS doped by Ti^{2+} ions [24], as was already mentioned above, the luminescence spectrum under excitation at 458 nm was observed at around 3600 cm^{-1} . A luminescence band centered at 4500 cm^{-1} corresponds to the ${}^2T_2 \rightarrow {}^2E$ emission of Ti^{3+} in ZnS under the same excitation wavelength. However, the luminescence spectrum of Ti-doped α - $ZnAl_2S_4$ consists of two broad bands centred at $E_{PL1}=1.41eV$ (11373 cm^{-1}) and $E_{PL2}=1.19eV$ (9600 cm^{-1}) and does not manifest similar features with those of Ti^{2+} and Ti^{3+} ions in ZnS [24]. Then, if the presence of Ti^{3+} and Ti^{2+} ions in both octahedral and tetrahedral coordinations is not confirmed by EPR and optical spectra, it is logical to assume that titanium is present as Ti^{4+} (ionic radius 0.61Å[88]) occupying the Al^{3+} site (ionic radius 0.67Å[88]). Since the α - $ZnAl_2S_4$ semiconductor has a wide indirect band-gap (E_g^{ind} (80K) =3.50eV[83]), the observed IR emission bands have been assigned to the $S^{2-}-Ti^{4+}$ charge transfer transitions. For the interpretation of the *charge transfer spectra*, the *Molecular orbital (MO) theory* is generally applied.

The basic idea behind the MO method, as compared with crystal field theory (CFT) discussed in the previous chapter, is to drop the main restricting CFT assumption that the electronic structure of ligands can be ignored, and include explicitly all the electrons in the quantum-mechanical treatment of the molecular system. The MO approach makes no *a priori* assumptions about the nature of the chemical bonding. Unlike CFT, where the atoms or groups of atoms of the complex are assumed to preserve mainly their individual features, in

the MO method the coordination system is considered, in principle, as an integral system in which separate atoms lose their individuality. Exact solution of the Schrödinger equation (1.1) for a coordination system is hardly possible at present because of computation difficulties. So far, the only practically acceptable approaches are those based on the *adiabatic approximation* and the *one-electron approximation*, which assumes that each electron can be considered as moving independently in the mean field created by the nuclei and the remaining electrons. In the one-electron approximation, the coordination system is described by one-electron states that in general extend throughout the entire system; they are called *molecular orbitals*.

In general, evaluation of one-electron molecular orbitals is still a complicated problem. The approach is based on the calculation of molecular orbitals of the AB_6 pseudo-molecule, ψ_{MO} , from various trial combinations of the individual atomic orbitals ψ_A and ψ_B , of the A and B ions, respectively. The molecular orbitals ψ_{MO} of the centre AB_6 are conveniently written in the form:

$$\psi_{MO} = N(\psi_A + \lambda\psi_B) \quad (4.1)$$

where N is a normalized constant and λ is a mixing coefficient. These molecular orbitals are approximate solutions to the Schrödinger equation(1.1), and their validity as wave functions for the AB_6 centre is tested by calculating observable quantities with these molecular orbital functions and then comparing with experimental results.

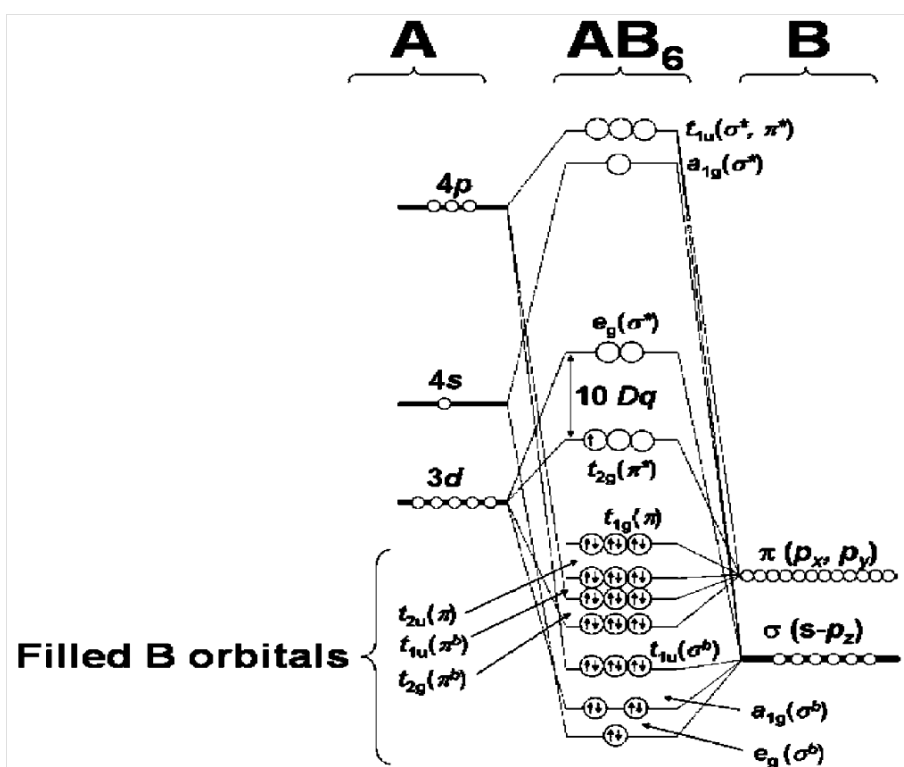


Fig. 4.10 A schematic energy-level diagram for an octahedral AB_6 centre in the frame of MO theory.

This diagram is constructed from the atomic levels of A and B[95]

In Fig. 4.10 A is the transition metal cationic ion and B are the anionic ions. Outer orbitals of A : $3d$, $4s$, and $4p$, in the valence (oxidation) state in complexes form the following sequence of energy levels:

$$E(3d) < E(4s) < E(4p) \quad (4.2)$$

Overlap of the wave functions of these orbitals with ligand functions is larger for $4s$ and $4p$ orbitals and smaller for the $3d$ functions. The different MO and energy levels of the molecule are determined from the outer atomic orbitals $3d$, $4s$, and $4p$ of the ions A (the left-hand side in Fig. 4.10) and the p and s atomic orbitals of the ligand B ions (the right-hand side in Fig. 4.10). The $4s$ orbital belongs to the A_{1g} representation (symmetry), $4p$ belongs to T_{1u} , and the five $3d$ orbitals form two groups: two $3d(e_g)$ orbitals (d_z^2 and $d_{x^2-y^2}$) belonging to the E_g representation, and three $3d(t_{2g})$ orbitals (d_{xy} , d_{xz} , and d_{yz}) that belong to T_{2g} . Due to symmetry reasons, only linear combinations of the ligand s and p orbitals must be considered for bonding, giving rise to the $\pi(p_x, p_y)$ and $\sigma(s-p_z)$ energy levels of B as in Fig. 4.10. The e_g orbitals are directed with their lobes of charge distribution toward the ligands and form σ bonds, whereas the t_{2g} orbitals can form only π bonds. Hence the overlap of the $3d(t_{2g})$ orbitals with the corresponding ligand functions is smaller than that of $3d(e_g)$. Each type of bonding produces a favourable energetic situation, σ or π bonding, and an unfavourable energetic situation, σ^* or π^* antibonding. It follows that the largest splitting into bonding and antibonding orbitals is expected in the formation of molecular orbitals by the $4s$ and $4p$ orbitals of the CA, smaller splitting comes from the $3d(e_g)$ orbitals, and the smallest one is due to the $3d(t_{2g})$ orbitals. It is seen that the lowest molecular orbitals a_{1g} , t_{1u} , e_g , and t_{2g} are bonding; the t_{1u} , t_{2u} , and t_{1g} molecular orbitals are nonbonding, while the remaining molecular orbitals (marked by asterisks) are antibonding. The antibonding states correspond to the higher energy levels of the AB_6 centre and are identified by an asterisk. The bonding states correspond to the lower energy levels of the AB_6 centre.

Therefore, further on the discussion is focussed on the observed PL spectra of $\alpha\text{-ZnAl}_2\text{S}_4:\text{Ti}^{4+}$ in terms of a cluster composed of the central Ti^{4+} ion and six sulphur ligands [96-97]. In favor of this assumption, the following proof can be also adduced. The one-electron energies of the $3p$ sulfur and $3d$ titanium electrons in free atoms are equal to -0.86 and -0.68 Rydbergs[98], respectively. Thus, the energy of the electron transfer from the $3p$ orbital of sulfur to the $3d$ orbital of titanium is equal to 0.18 Rydbergs or 19746 cm^{-1} . This value which does not account for the crystal field splitting of the $3d$ -state is very close to the energy of the observed absorption band at 2.40eV (19360 cm^{-1}) in $\text{ZnAl}_2\text{S}_4:\text{Ti}$ (see Fig. 4.2). The outer electronic configuration of Ti^{4+} ions is $3d^0$, while each S^{2-} ion has an outer electronic configuration $3p^6$. Thus, there are 36 electrons given by the six S^{2-} ions (B ions) which fill all the bonding energy levels of the AB_6 centre. For symmetry reasons, the $3p_z$

atomic orbitals of S^{2-} ions are combined with the $3s$ atomic orbitals of the S^{2-} ions to provide σ bonds, while the $3p_x$ and $3p_y$ atomic orbitals provide π bonds. The ground state of this cluster is the ${}^1A_{1g}$ -state. The configuration of this state can be illustratively written as $[Ti^{4+}(t_{2g}^{*0}e_g^{*0}), {}^1A_{1g}][S_6, {}^1A_{1g}]$. The schematic molecular orbitals energy-level diagram for an octahedrally coordinated Ti -ion (TiL_6 is a cluster, L is a ligand) presented in [95] makes it possible to assume that the excited states of TiS_6 complex characterized by odd parity arise from the electronic configurations $t_{2g}^*t_{1u}^5$ and $t_{2g}^*t_{2u}^5$ that contain an electron in the t_{2g}^* shell and a hole in the t_{1u} or t_{2u} shell. The configuration $t_{2g}^*t_{1u}^5$ gives rise to states with all possible combinations of $S = 0, 1$ and $\Gamma = A_{2u}, T_{1u}, T_{2u}, E_u$.

For states arising from the configuration $t_{2g}^*t_{2u}^5$ $S=0, 1$, while $\Gamma = A_{1u}, T_{1u}, T_{2u}, E_u$. The PL transitions ${}^{2S+1}A_{2u}, {}^{2S+1}A_{1u}, {}^{2S+1}T_{2u}, {}^{2S+1}E_u \rightarrow {}^1A_{1g}$ ($S = 0, 1$) are dipole forbidden, in the case of $\Delta S = 1$ some of these transitions are also spin forbidden ($\Delta S = 1$). The allowed electric-dipole transitions are ${}^1T_{1u}^c \rightarrow {}^1A_{1g}$, where $c = a, b$, and ${}^1T_{1u}^a$ and ${}^1T_{1u}^b$ denote the lower and the high energy states arising from mixing of the ${}^1T_{1u}(t_{2g}t_{1u}^5)$ and ${}^1T_{1u}(t_{2g}t_{2u}^5)$ terms by the Coulomb interaction. At the same time according to Hund's rule, the lowest in energy excited state is the ${}^3T_{1u}^a$ -state. The labeling of this state has the same sense as in the case of the ${}^1T_{1u}^a$ state with the only difference that the two states ${}^3T_{1u}^c$ ($c = a, b$) arise from the mixing of the terms ${}^3T_{1u}(t_{2g}t_{1u}^5)$ and ${}^3T_{1u}(t_{2g}t_{2u}^5)$ by the Coulomb interaction. The PL transition ${}^3T_{1u}^a \rightarrow {}^1A_{1g}$ is spin forbidden, but dipole allowed. Basing on these considerations it is assumed that the two observed IR bands can be possibly assigned to the ${}^3T_{1u}^a \rightarrow {}^1A_{1g}$ and ${}^1T_{1u}^a \rightarrow {}^1A_{1g}$ transitions.

The performed analysis of the experimental data; makes it possible to suppose that the energy spectrum of the TiS_6 complex can be conditionally illustrated by three adiabatic potential sheets (Fig. 4.11). The ground adiabatic potential sheet ${}^1A_{1g}$ looks as follows:

$$E({}^1A_{1g}) = \frac{\hbar\omega}{2}q^2 \quad (4.3)$$

where $\hbar\omega$ is the energy of the vibrational quantum. The expressions for the first ${}^3T_{1u}^a$ and second ${}^1T_{1u}^a$ excited sheets

$$E({}^3T_{1u}^a) = \frac{\hbar\omega}{2}q^2 + \Delta_1 - \nu_1q; \quad E({}^1T_{1u}^a) = \frac{\hbar\omega}{2}q^2 + \Delta_2 - \nu_2q \quad (4.4)$$

include the energy gaps Δ_1 and Δ_2 between the ground ${}^1A_{1g}$ and excited states (respectively, ${}^3T_{1u}$ and ${}^1T_{1u}$) in the rigid lattice, as well as the terms responsible for the interaction of the ${}^3T_{1u}$ and

1T_1 states with the full symmetric vibration of the TiS_6 complex. Finally, ν_1 and ν_2 are the corresponding vibronic coupling constants.

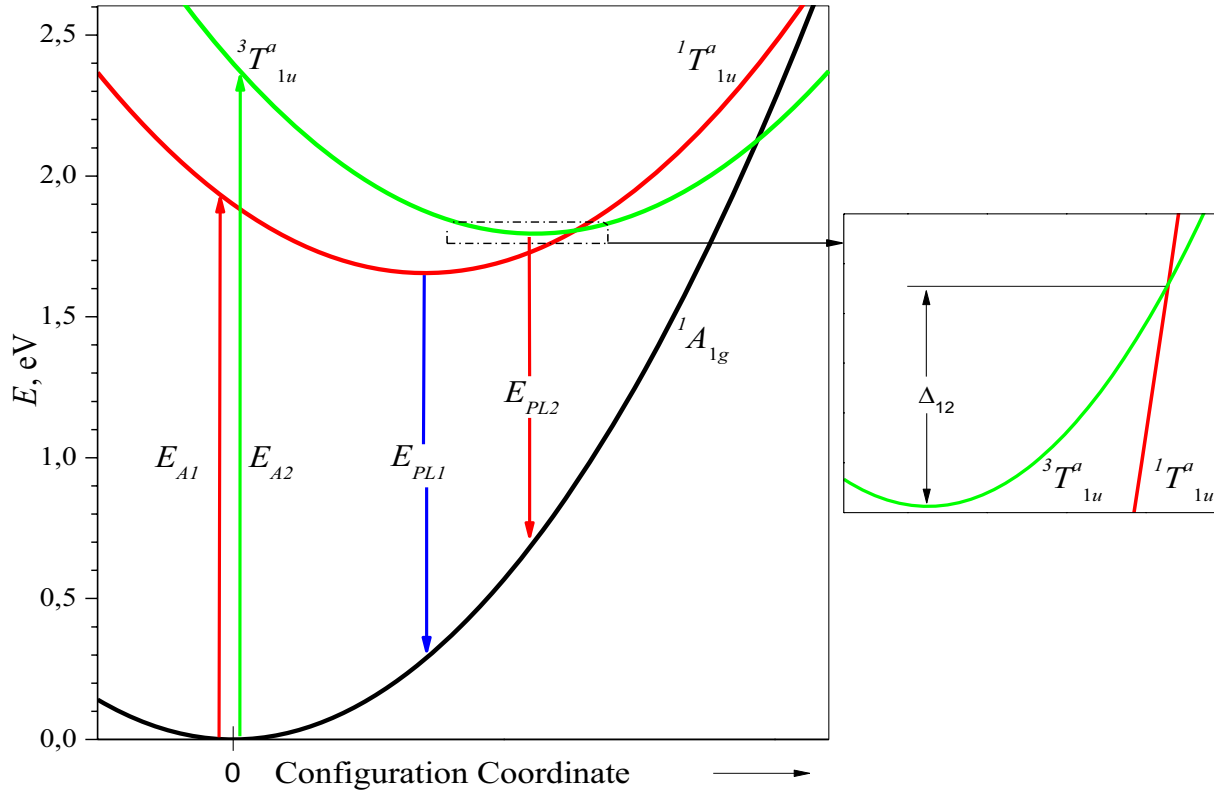


Fig. 4.11 Single configuration-coordinate diagram for TiS_6 complex in $\alpha\text{-ZnAl}_2\text{S}_4$.

In the adiabatic approximation the maxima of the luminescence bands under “red” (E_{PL1}) and “green” (E_{PL2}) excitation can be estimated as follows from(4.6). The minimum of the ${}^3T_{1u}$ energy level is to be determined by equalizing its first derivate with zero:

$$\begin{aligned}
 E({}^3T_{1u}^u) &= \frac{\hbar\omega}{2}q^2 + \Delta_1 - \nu_1q; \\
 \frac{dE({}^3T_{1u}^u)}{dq} &= \hbar\omega q - \nu_1; \quad \hbar\omega q - \nu_1 = 0; \\
 q &= \frac{\nu_1}{\hbar\omega}
 \end{aligned}
 \tag{4.5}$$

and the difference between the excited and ground states in this point gives the maximum of photoluminescence

$$\begin{cases}
 E({}^3T_{1u}) = \frac{\nu_1^2}{2\hbar\omega} + \Delta_1 - \frac{\nu_1^2}{\hbar\omega}; & E({}^3T_{1u}) - E({}^1A_{1g}) = \frac{\nu_1^2}{2\hbar\omega} + \Delta_1 - \frac{\nu_1^2}{\hbar\omega} - \frac{\nu_1^2}{2\hbar\omega}; \\
 E({}^1A_{1g}) = \frac{\nu_1^2}{2\hbar\omega}
 \end{cases}
 \tag{4.6}$$

$$E_{PL1} = \Delta_1 - \frac{\nu_1^2}{\hbar\omega}$$

The same procedure is carried out to determine the maximum of the luminescence bands under “green” (E_{PL2}) excitation, which is described by the following relation:

$$E_{PL2} = \Delta_2 - \frac{\nu_2^2}{\hbar\omega} \quad (4.7)$$

Hereafter it is assumed that gaps Δ_1 and Δ_2 are approximately equal to the energies of the A_0 - and A_1 absorption bands $\Delta_1 = E_{A0} \approx 1.9\text{eV}$, $\Delta_2 = E_{A1} \approx 2.4\text{eV}$. On the other hand, as can be seen from the insert in Fig. 4.4 or especially from the Fig. 4.6, the energetic distance between the pick located at 1.5eV, which seems to be a zero – phonon line, and that of the first vibronic replica is equal to the quantum vibrational energy $\hbar\omega = 39\text{meV} = 315\text{cm}^{-1}$. This value is in good agreement with the data in [83] for the undoped ZnAl_2S_4 spinel type crystals. Taking into account the experimental values of the $E_{PL1} \approx 1.41\text{eV}$ and $E_{PL2} \approx 1.19\text{eV}$ emission components, the vibronic coupling constants $\nu_1 = 138\text{meV} = 1115\text{cm}^{-1}$ and $\nu_2 = 217\text{meV} = 1753\text{cm}^{-1}$ have been obtained from Equations (4.6) and (4.7), respectively. The height of the activation barrier can be found if the following is observed:

- at the intersection point of the ${}^3T_{1u}$ and ${}^1T_{1u}$ levels the energy is the same for both levels

$$\begin{aligned} E({}^3T_{1u}^u) &= E({}^1T_{1u}^u) \\ \frac{\hbar\omega}{2}q^2 + \Delta_1 - \nu_1q &= \frac{\hbar\omega}{2}q^2 + \Delta_2 - \nu_2q \\ q &= \frac{\Delta_1 - \Delta_2}{\nu_1 - \nu_2} \end{aligned} \quad (4.8)$$

- thus the barrier height is

$$\left\{ \begin{aligned} {}^1T_{1u}^u(\text{min}) &= \Delta_1 - \frac{\nu_1^2}{2\hbar\omega} \\ {}^1T_{1u}^u(\text{intersection}) &= \frac{\hbar\omega}{2} \left(\frac{\Delta_1 - \Delta_2}{\nu_2 - \nu_1} \right)^2 + \Delta_1 + \nu_1 \frac{\Delta_1 - \Delta_2}{\nu_2 - \nu_1} \end{aligned} \right.$$

$${}^1T_{1u}^u(\text{intersection}) - {}^1T_{1u}^u(\text{min}) = \delta_{12} \quad (4.9)$$

$$\delta_{12} = \frac{\hbar\omega}{2} \left(\frac{\Delta_1 - \Delta_2}{\nu_2 - \nu_1} + \frac{\nu_2}{\hbar\omega} \right)^2 \approx 11\text{meV}$$

The estimated barrier height $\delta_{12} \approx 11\text{meV} \approx 130\text{K}$ (Fig. 4.11, insert) is in good accordance with the experimental value $T \approx 120\text{K}$ at which the intensity of the luminescence band E_{PL1} becomes higher than that of E_{PL2} band. Under “green” excitation and $T \leq 80\text{K}$, when only the minimum of the adiabatic potential sheet complying with the ${}^1T_{1u}^a$ – state is populated, the maximum of the emission band corresponds to $E_{PL2} = 1.19\text{eV}$. With

temperature rise the tunnelling through the barrier δ_{12} leads to the population of the adiabatic potential sheet minimum related to the ${}^3T_{1u}^a$ - state, and in the *PL* spectra, along with band E_{PL2} band E_{PL1} appears. At $T > 200$ K this band dominates in the spectra. Thus, at “green” excitation significant changes in the shape of the luminescence band with temperature increase can be observed as a result of depopulation of the minimum of the adiabatic potential ${}^1T_{1u}$ and simultaneous population of the minimum of the adiabatic potential sheet ${}^3T_{1u}$ due to the tunnelling through the barrier. Such a process can take place because the tunnelling through the barrier in this case occurs much faster than the spontaneous decay of ${}^1T_{1u}$ state.

As mentioned above, the excitation by green light leads to the appearance of short-living narrow lines (Fig. 4.6) in the *PL* spectra at low temperatures. With temperature rise these lines cannot be discerned, they merge with the broad band having the peak position at $1.1\mu\text{m}$. The origin of these lines in the first interpretation may be probably assigned to spin- and dipole-forbidden transitions of the type of ${}^3E_u \rightarrow {}^1A_{1g}$ and ${}^3A_{1(2)u} \rightarrow {}^1A_{1g}$. These transitions would have represent an analogue of the well-known optical transition ${}^2E_g \rightarrow {}^4A_{2g}$

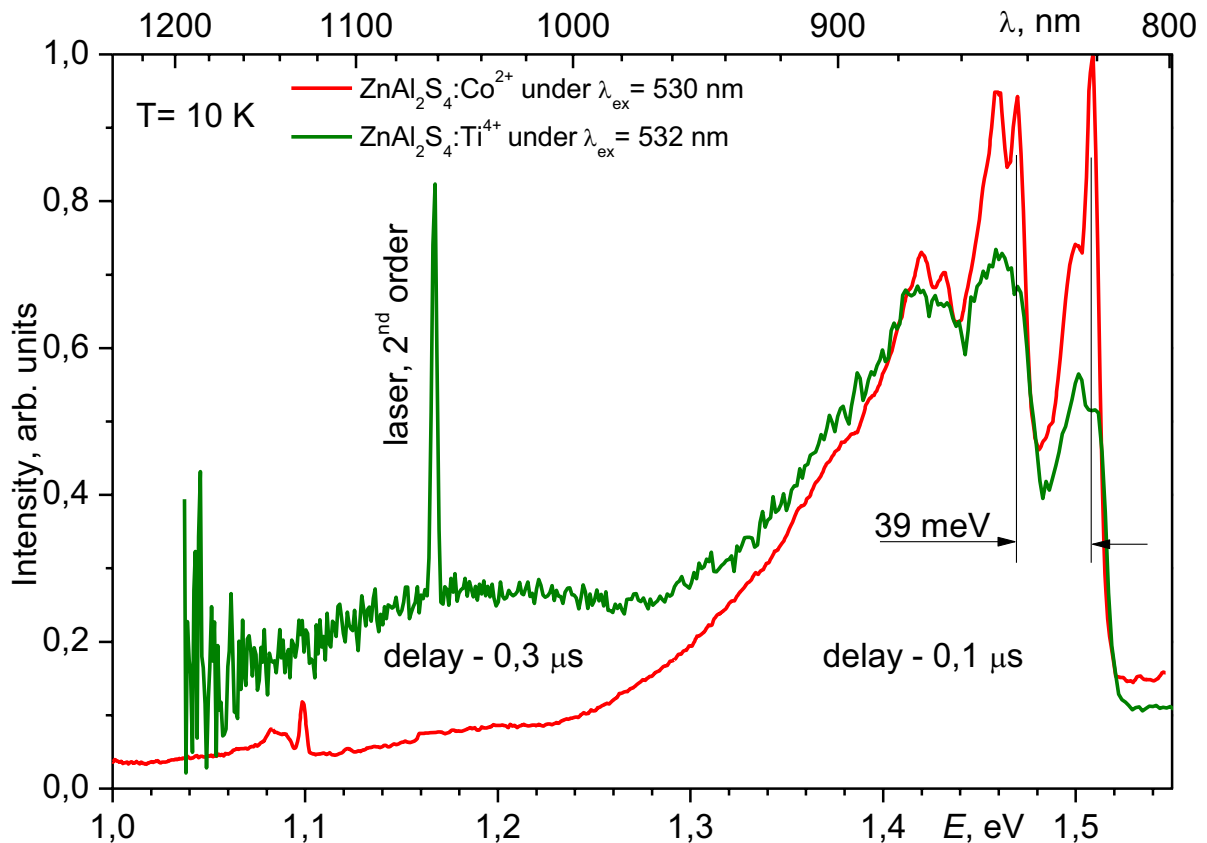


Fig. 4.12 Time-resolved luminescence spectra of $\text{ZnAl}_2\text{S}_4:\text{Co}^{2+}$ and $\text{ZnAl}_2\text{S}_4:\text{Ti}^{4+}$ under “green” excitation at low temperature

in ruby and in $\alpha\text{-ZnAl}_2\text{S}_4:\text{Cr}$ [31], which manifests in the low-temperature *PL* spectra as a narrow zero-phonon R-line that disappears at higher temperatures. As to the optical transitions

facilitated by electron transfer between the orbitals t_{2g} and t_{1g} they are parity forbidden, and, therefore, are not included in consideration.

In Chapter 3, the analysis has been made on the luminescence properties of the Co-doped ZnAl_2S_4 single crystals. The time-resolved luminescence at low temperature consists of several components at different delays from the laser impulse. The fastest of them, under $\lambda_{\text{ex}} = 530\text{nm}$, have the same similitude as the time-resolved luminescence of ZnAl_2S_4 : Ti presented in Fig. 4.6. Moreover, they practically coincide as energetic position and distance between the picks (Fig. 4.12). The fastest narrow lines of the tetrahedral coordinated Co^{2+} doped ZnAl_2S_4 are ascribed to the electronic transition from the ${}^2A({}^2G)$ level to the lower excited triple degenerated ${}^4T_1({}^4F)$ state, split by the spin-orbit coupling (see Chapter 3). The zero phonon lines located at 1.509eV are accompanied by the 1st (1.470eV) and the 2nd (1.431eV) vibronic replica, the phonon energy being equal to $\hbar\Omega_{ph} = 39\text{meV}$. Thus, it is obvious that the fast component of the ZnAl_2S_4 : Ti revealed in the time-resolved luminescence is due to the electronic transitions of the Co^{2+} ions located in tetrahedral sites. In addition, the fast decay time component τ_1 under “green” excitation presented in the Fig. 4.7 seems to characterize the ZnAl_2S_4 : Co luminescence discussed above. In this way the time-resolved and decay time components discussed above can be excluded as being due to the electronic transitions of the octahedral Ti-doped ZnAl_2S_4 .

4.4 Conclusions

- It has been found that the α -ZnAl₂S₄:Ti single crystals exhibit luminescence in the IR spectral range 0.8–1.4 μ m. The obtained spectroscopic results (steady-state and time resolved photoluminescence, optical absorption and excitation luminescence spectra), have been interpreted in terms of a cluster composed of the central Ti⁴⁺ ion in an octahedral coordination of six sulphur ions. The observed spectral bands are assigned to the electronic transitions arising from the ligand – Ti⁴⁺ charge transfer for octahedral sites of titanium, which is in agreement with the experimental evidence for the absence of the EPR signal from Ti ions.
- The observed two broad bands of α -ZnAl₂S₄:Ti⁴⁺ crystal's emission spectra, centred at $E_{PL1}=1.41\text{eV}$ and $E_{PL2}=1.19\text{eV}$ have been attributed to the electronic transition from the ${}^1T_{1u}^a$ and ${}^3T_{1u}^a$ excited levels to the ground state ${}^1A_{1g}$ respectively. The vibronic coupling constants for these two levels have been found to be $\nu_1=138\text{meV}$ (1115 cm^{-1}) and $\nu_2=217\text{meV}$ (1753 cm^{-1}) respectively, whereas the energy barrier height – $\delta_{12}=11\text{meV}\approx 130\text{K}$. The estimated barrier height is in good accordance with the experimental temperature value $T\approx 120\text{K}$ at which the intensity of the E_{PL1} -band becomes higher than that of E_{PL2} -band due to the redistribution of the population between the excited states caused by the tunnelling through the barrier.
- It was shown that the fast decay time component τ_1 , located at 1.509eV and accompanied by the 1st (1.470eV) and the 2nd (1.431eV) vibronic replica, manifested in the time-resolved spectrum of the ZnAl₂S₄: Ti is due to the presence of the tetrahedral coordinated Co²⁺ ions traces (uncontrollable impurities).

GENERAL CONCLUSIONS

Based on the results of the conducted research, the following conclusion^s can be made.

- For the first time, the single crystals of the α -ZnAl₂S₄ spinel type wide band gap semiconductor doped by the transition metals Ti, Co and V have been obtained. The crystals, grown by the chemical vapour transport method, with the activator impurities concentrations 0.01 – 0.1% at. and the volume up to 20 mm³, correspond to optically homogeneous octahedrons with (111) - oriented mirror-like faces. The x-ray analyses have confirmed that all samples crystallised into the normal spinel type structure with O_h ⁷ cubic symmetry.
- It has been found that the α -ZnAl₂S₄:Ti single crystals exhibit luminescence in the IR spectral range 0.8–1.4 μ m. The obtained spectroscopic results (steady-state and time resolved photoluminescence, optical absorption and excitation luminescence spectra), have been interpreted in terms of a cluster composed of the central Ti⁴⁺ ion in an octahedral coordination of six sulphur ions. The observed spectral bands are assigned to the electronic transitions arising from the ligand – Ti⁴⁺ charge transfer for octahedral sites of titanium, which is in agreement with the experimental evidence for the absence of the EPR signal from Ti ions.
- The observed two broad bands of α -ZnAl₂S₄:Ti⁴⁺ crystal's emission spectra, centred at $E_{PL1}=1.41\text{eV}$ and $E_{PL2}=1.19\text{eV}$ have been attributed to the electronic transition from the ${}^1T_{1u}^a$ and ${}^3T_{1u}^a$ excited levels to the ground state ${}^1A_{1g}$ respectively. The vibronic coupling constants for these two levels have been found to be $\nu_1=138\text{meV}$ (1115 cm⁻¹) and $\nu_2=217\text{meV}$ (1753 cm⁻¹) respectively, whereas the energy barrier height – $\delta_{12}=11\text{meV}\approx 130\text{K}$. The estimated barrier height is in good accordance with the experimental temperature value $T\approx 120\text{K}$ at which the intensity of the E_{PL1} -band becomes higher than that of E_{PL2} -band due to the redistribution of the population between the excited states caused by the tunnelling through the barrier.
- The structure of α -ZnAl₂S₄:Co crystals absorption spectrum composed of three components located at 0.77eV ($E_{A1}\approx 6450\text{cm}^{-1}$, quadruplet), 1.60eV ($E_{A2}\approx 12990\text{cm}^{-1}$, triplet) and 2.58eV ($E_{A3}\approx 20160\text{cm}^{-1}$, broad band) is determined by the electronic transitions of Co²⁺ ions located in tetrahedral sites. The values of the spin-orbit coupling constants of the first two components found to be 189 and 321cm⁻¹, respectively, indicate a weak crystal field influence and a strong spin-orbit coupling.
- It has been shown that the luminescence of α -ZnAl₂S₄:Co crystals is due to the electronic transitions between the excited levels of the Co²⁺ ions. Four radiative spectral components have been revealed using the time-resolved spectroscopy at different excitation wavelengths. The fastest E_{PL1} narrow lines located in the spectral range 1.42 - 1.51eV are ascribed to the transition from the ${}^2A({}^2G)$ short life-time level to the lower excited triple

degenerated ${}^4T_1({}^4F)$ state; the narrow line at $E_{PL3}=1.122\text{eV}$ is attributed to the transition ${}^4T_1({}^4P) \rightarrow {}^4T_2({}^4F)$; the two broad bands centred at $E_{PL2}=1.32\text{eV}$ and $E_{PL4}=0.96\text{eV}$ with a slow decay, are ascribed to the partially forbidden transitions ${}^2E({}^2G) \rightarrow {}^4T_2({}^4F)$ and ${}^2E({}^2G) \rightarrow {}^4T_1({}^4F)$, respectively.

- The absorption and luminescent properties of $\alpha\text{-ZnAl}_2\text{S}_4\text{:V}$ spinel type crystals are the result of electronic transitions of trivalent vanadium ions located in octahedral sites. It has been found that the rise of temperature leads to the enhancement of the integral luminescence intensity and to the broadening of the spectrum centered at $\lambda = 1.4\mu\text{m}$, due to the ${}^3T_{2g}({}^3F) \rightarrow {}^3T_{1g}({}^3F)$ vibronic transitions which suppress other emission channels.

- The three main spectral components of $\alpha\text{-ZnAl}_2\text{S}_4\text{:V}$ IR luminescence – $E_{PL1} \approx 0.75\text{eV}$, $E_{PL2} \approx 0.9\text{eV}$ and $E_{PL3} \approx 1.05\text{eV}$ revealed at low temperatures are caused, respectively, by the ${}^1E_g({}^1D) \rightarrow {}^3T_{1g}({}^3F)$; ${}^3T_{2g}({}^3F) \rightarrow {}^3T_{1g}({}^3F)$, and ${}^1A_{1g}({}^1G) \rightarrow {}^1E_g({}^1D)$, ${}^1T_{2g}({}^1D)$ electronic transitions of the V^{3+} ions. The coexistence of the E_{PL2} broad band with E_{PL1} narrow lines at low temperatures, when the thermal energy $k_B T$ is much less than the height of the potential barrier between the ${}^3T_{2g}({}^3F)$ and ${}^1E_g({}^1D)$ excited states, is explained assuming that there is a phonon assisted tunnelling between these two states.

Taken together, the results obtained on the base of comparative analysis of the spectroscopic properties of $\alpha\text{-ZnAl}_2\text{S}_4$ spinel type crystals doped with transition metals Ti, Co, and V suggest that $\alpha\text{-ZnAl}_2\text{S}_4\text{:V}^{3+}$ compound is the most appropriate for applications as active media for solid state IR-lasers tunable in the 1.2-1.6 μm wavelength range that corresponds to the spectral region used in the fibre-optics communication systems.

BIBLIOGRAPHY

- 1 Vermaas F. H. S. and Schmidt E. R., The influence of ionic radii of cations and covalent forces on the unit cell dimensions of spinels *Contributions to Mineralogy and Petrology* 1959 vol. **6** p. 219-32
- 2 Von Neida A. R. and Shick L. K., Single-Crystal Growth of Some Chalcogenide Spinels *Journal of Applied Physics* 1969 vol. **40** p. 1013-5
- 3 Von Philipsborn H., Crystal growth and characterization of chromium sulfo- and seleno-spinels *Journal of Crystal Growth* 1971 vol. **9** p. 296-304
- 4 Tretyakov Y. D., Gordeev I. V. and Kesler Y. A., Investigation of some chalcogenides with spinel structure *Journal of Solid State Chemistry* 1977 vol. **20** p. 345-58
- 5 Bonsall S. B. and Hummel F. A., Phase equilibria in the systems ZnS---Al₂S₃ and ZnAl₂S₄---ZnIn₂S₄ *Journal of Solid State Chemistry* 1978 vol. **25** p. 379-86
- 6 Hill R. J., Craig J. R. and Gibbs G. V., Systematics of the spinel structure type *Physics and Chemistry of Minerals* 1979 vol. **4** p. 317-39
- 7 Berthold H. J., Köhler K. and Wartchow R., Kristallstrukturverfeinerung des Zinkaluminiumsulfids ZnAl₂S₄ (normale Spinellstruktur) mit Röntgen-Einkristalldaten *Zeitschrift für anorganische und allgemeine Chemie* 1983 vol. **496** p. 7-20
- 8 Pollert E., Crystal chemistry of magnetic oxides part 1: General problems -- Spinels *Progress in Crystal Growth and Characterization* 1984 vol. **9** p. 263-323
- 9 Hills M. E., Harris D. C. and Lowe-Ma C. K., Zinc aluminum sulfide: Electron paramagnetic resonance spectroscopy and infrared transmittance *Journal of Physics and Chemistry of Solids* 1987 vol. **48** p. 501-7
- 10 Syrbu N. N., Bogdanash M. and Moldovyan N. A., Vibrational modes in ZnAl₂S₄ and CdIn₂S₄ crystals *Infrared Physics & Technology* 1996 vol. **37** p. 763-8
- 11 Moulton P., *Optical Photonics News* 1982 vol. **8** p. 9
- 12 Yamaga M., Yosida T., Hara S., Kodama N. and Henderson B., Optical and electron spin resonance spectroscopy of Ti³⁺ and Ti⁴⁺ in Al₂O₃ *Journal of Applied Physics* 1994 vol. **75** p. 1111-7
- 13 Wong W. C., McClure D. S., Basun S. A. and Kokta M. R., Charge-exchange processes in titanium-doped sapphire crystals. I. Charge-exchange energies and titanium-bound excitons *Physical Review B* 1995 vol. **51** p. 5682
- 14 Wegner T. and Petermann K., Excited state absorption of Ti³⁺:YAlO₃ *Applied Physics B: Lasers and Optics* 1989 vol. **49** p. 275-8

- 15 Boyn R., Dziesiaty J. and Wruck D., Ti^{2+} in CdS: A centre with excited states in resonance with the conduction band? *physica status solidi (b)* 1970 vol. **42** p. K197-K200
- 16 Boyn R. and Ruszczynski G., Jahn-teller structure in ${}^3A_2({}^3F) \rightarrow {}^3T_1({}^3F)$ absorption band of CdS: Ti^{2+} *physica status solidi (b)* 1971 vol. **48** p. 643-55
- 17 Rosenfeld A., Boyn R. and Ruszczynski G., Jahn-Teller Effect on the Optical Absorption Spectra of CdS: Ti^{2+} and CdSe: Ti^{2+} *physica status solidi (b)* 1975 vol. **70** p. 601-10
- 18 Ruszczynski G. and Boyn R., Jahn-Teller Coupling Parameters from Stress-Dichroism Spectra for CdS: Ti^{2+} and CdS: Co^{2+} *physica status solidi (b)* 1976 vol. **76** p. 427-36
- 19 Kocot K. and Baranowski J. M., The Resonant States of the $Ti(d^2)$ Impurity in CdSe *physica status solidi (b)* 1977 vol. **81** p. 629-35
- 20 Langer J. M. and Baranowski J. M., Optical properties of transition metal impurities in CdSe. I. Crystal-field spectra *physica status solidi (b)* 1971 vol. **44** p. 155-66
- 21 Böttcher R. and Dziesiaty J., EPR Spectra of Transition Element Impurities with $3d^2$ Configuration in Hexagonal CdS and CdSe Single Crystals *physica status solidi (b)* 1973 vol. **57** p. 617-26
- 22 Böttcher R. and Dziesiaty J., Ligand Hyperfine Interaction of Ti^{2+} in CdS and CdSe on Sites with Trigonal Symmetry C_{3v} *physica status solidi (b)* 1972 vol. **53** p. 505-18
- 23 Peka P., U.Lehr M., J.Schulz H., J.Dziesiaty and S.Müller, Identification of titanium dopants in CdS, CdSe and Cd(S,Se) crystals by luminescence and EPR methods *Journal of Crystal Growth* 1996 vol. **161** p. 277-81
- 24 Dziesiaty J., Lehr M. U., Peka P., Klimakow A., Müller S. and Schulz H.-J., Optical and paramagnetic properties of titanium centres in ZnS *Eur. Phys. J. B* 1998 vol. **4** p. 269-77
- 25 Schepler K. L. and Kokta M., Spectroscopic properties of GdScAl garnet doped with Ti^{3+} *Journal of Applied Physics* 1988 vol. **63** p. 960
- 26 Kodama N. and Yamaga M., Crystal characterization and optical spectroscopy of Ti^{3+} -doped $CaGdAlO_4$ crystals *Physical Review B* 1998 vol. **57** p. 811
- 27 Bausa L. E., Vergara I., Garcia-Sole J., Strek W. and Deren P. J., Laser-excited luminescence in Ti-doped $MgAl_2O_4$ spinel *Journal of Applied Physics* 1990 vol. **68** p. 736-40
- 28 Jouini A., Sato H., Yoshikawa A., Fukuda T., Boulon G., Kato K. and Hanamura E., Crystal growth and optical absorption of pure and Ti, Mn-doped $MgAl_2O_4$ spinel *Journal of Crystal Growth* 2006 vol. **287** p. 313-7

- 29 Jouini A., Yoshikawa A., Brenier A., Fukuda T. and Boulon G., Optical properties of transition metal ion-doped MgAl_2O_4 spinel for laser application *Physica Status Solidi (c)* 2007 vol. **4** p. 1380 - 3
- 30 Sato T., Shirai M., Tanaka K., Kawabe Y. and Hanamura E., Strong blue emission from Ti-doped MgAl_2O_4 crystals *Journal of Luminescence* 2005 vol. **114** p. 155-61
- 31 Broussell I., Fortin E., Kulyuk L., Popov S., Anedda A. and Corpino R., Optical properties of alpha- ZnAl_2S_4 :Cr single crystals *Journal of Applied Physics* 1998 vol. **84** p. 533-40
- 32 Weakliem H. A., Optical Spectra of Ni^{2+} , Co^{2+} and Cu^{2+} in Tetrahedral Sites in Crystals *The Journal of Chemical Physics* 1962 vol. **36** p. 2117-40
- 33 Ferguson J., Wood D. L. and Van Uitert L. G., Crystal-Field Spectra of $d^{3,7}$ Ions. V. Tetrahedral Co^{2+} in ZnAl_2O_4 Spinel *The Journal of Chemical Physics* 1969 vol. **51** p. 2904-10
- 34 Salomon R. E. and Gillen R. D., Optical spectra of chromium(III), cobalt(II), and nickel(II) ions in mixed spinels *The Journal of Physical Chemistry* 1970 vol. **74** p. 4252-6
- 35 Donegan J. F., Bergin F. J., Imbusch G. F. and Remeika J. P., Luminescence from LiGa_5O_8 :Co *Journal of Luminescence* 1984 vol. **31-32** p. 278-80
- 36 Borghesi A., Guizzetti G., Nosenzo L., Prospero T. and Viticoli S., Optical absorption of Co(II) ion in $\text{Co}_x\text{Zn}_{1-x}\text{In}_2\text{S}_4$ ($0.07 < x < 0.46$) solid solution *Solid State Communications* 1987 vol. **64** p. 1187-9
- 37 Kim H.-G. and Kim W.-T., Optical absorption of ZnGa_2S_4 and ZnGa_2S_4 : Co^{2+} crystals *Physical Review B* 1990 vol. **41** p. 8541
- 38 Abritta T. and Blak F. H., Luminescence study of ZnGa_2O_4 : Co^{2+} *Journal of Luminescence* 1991 vol. **48-49** p. 558-60
- 39 Kuleshov N. V., Mikhailov V. P., Scherbitsky V. G., Prokoshin P. V. and Yumashev K. V., Absorption and luminescence of tetrahedral Co^{2+} ion in MgAl_2O_4 *Journal of Luminescence* 1993 vol. **55** p. 265-9
- 40 Park T.-Y., Jin M.-S., Choe S.-H., Goh J.-M. and Kim W.-T., Optical properties of MnAl_2S_4 and MnAl_2Se_4 single crystals *Journal of Applied Physics* 1999 vol. **86** p. 3478-80
- 41 Oh S. K., Song H. J., Kim W. T., Kim H. G., Lee C. I., Park T. Y., Jin M. S. and Yoon C. S., Impurity optical absorption of Co^{2+} -doped MgAl_2S_4 and CaAl_2S_4 single crystals *Journal of Physics and Chemistry of Solids* 2000 vol. **61** p. 1243-7

- 42 Radovanovic P. V. and Gamelin D. R., Electronic Absorption Spectroscopy of Cobalt Ions in Diluted Magnetic Semiconductor Quantum Dots: Demonstration of an Isocrystalline Core/Shell Synthetic Method *Journal of the American Chemical Society* 2001 vol. **123** p. 12207-14
- 43 Radovanovic P. V., Norberg N. S., McNally K. E. and Gamelin D. R., Colloidal Transition-Metal-Doped ZnO Quantum Dots *Journal of the American Chemical Society* 2002 vol. **124** p. 15192-3
- 44 Yoon C.-S., Park K.-H., Kim D.-T., Park T.-Y., Jin M.-S., Oh S.-K. and Kim W.-T., Optical properties of Ga₂Se₃ and Ga₂Se₃:Co²⁺ single crystals *Journal of Physics and Chemistry of Solids* 2001 vol. **62** p. 1131-7
- 45 Grinberg M., Tsuboi T., Berkowski M. and Kaczmarek S. M., Jahn-Teller effect in Co²⁺-doped SrLaGa₃O₇ *Journal of Alloys and Compounds* 2002 vol. **341** p. 170-3
- 46 Duan X., Yuan D., Cheng X., Sun Z., Sun H., Xu D. and Lv M., Spectroscopic properties of Co²⁺: ZnAl₂O₄ nanocrystals in sol-gel derived glass-ceramics *Journal of Physics and Chemistry of Solids* 2003 vol. **64** p. 1021-5
- 47 Volk Y. V., Denisov I. A., Malyarevich A. M., Yumashev K. V., Dymshits O. S., Shashkin A. V., Zhilin A. A., Kang U. and Lee K.-H., Magnesium- and Zinc-Aluminosilicate Cobalt-Doped Glass Ceramics as Saturable Absorbers for Diode-Pumped 1.3- μ m Laser *Appl. Opt.* 2004 vol. **43** p. 682-7
- 48 Izumi K., Miyazaki S., Yoshida S., Mizokawa T. and Hanamura E., Optical properties of 3d transition-metal-doped MgAl₂O₄ spinels *Physical Review B* 2007 vol. **76** p. 075111
- 49 Volk Y. V., Malyarevich A. M., Yumashev K. V., Matrosov V. N., Matrosova T. A. and Kupchenko M. I., Anisotropy of nonlinear absorption in Co²⁺:MgAl₂O₄ crystal *Applied Physics B: Lasers and Optics* 2007 vol. **88** p. 443-7
- 50 Liehr A. D. and Ballhausen C. J., Complete theory of Ni(II) and V(III) in cubic crystalline fields *Annals of Physics* 1959 vol. **6** p. 134-55
- 51 McClure D. S., Optical Spectra of Transition-Metal Ions in Corundum *The Journal of Chemical Physics* 1962 vol. **36** p. 2757-79
- 52 Rogers D. B., Arnott R. J., Wold A. and Goodenough J. B., The preparation and properties of some vanadium spinels *Journal of Physics and Chemistry of Solids* 1963 vol. **24** p. 347-60
- 53 Sturge M. D., Optical Spectrum of Divalent Vanadium in Octahedral Coordination *Physical Review* 1963 vol. **130** p. 639

- 54 Goldschmidt Z., Low W. and Foguel M., Fluorescence spectrum of trivalent vanadium in corundum *Physics Letters* 1965 vol. **19** p. 17-8
- 55 Robbins M., Menth A., Mikovsky M. A. and Sherwood R. C., Magnetic and crystallographic evidence for localization to delocalization of V d-electron levels in $\text{CuCr}_{2-x}\text{V}_x\text{S}_4$ spinels *Journal of Physics and Chemistry of Solids* 1970 vol. **31** p. 423-30
- 56 Goldstein L., Gibart P., Mejai M. and Perrin M., Magnetic structures of the spinel compounds $\text{MnCr}_{2-x}\text{V}_x\text{S}_4$ *Physica B+C* 1977 vol. **86-88** p. 893-5
- 57 Buhmann D., Schulz H. J. and Thiede M., Photoluminescence of CdS: V, Cu crystals *Physical Review B* 1979 vol. **19** p. 5360
- 58 Aszodi G. and Kaufmann U., Zeeman spectroscopy of the vanadium luminescence in GaP and GaAs *Physical Review B* 1985 vol. **32** p. 7108
- 59 Knierim W., Honold A., Brauch U. and Durr U., Optical and lasing properties of V^{2+} -doped halide crystals *J. Opt. Soc. Am. B* 1986 vol. **3** p. 119-24
- 60 Biernacki S. W., Roussos G. and Schulz H.-J., The luminescence of V^{2+} (d^3) and V^{3+} (d^2) ions in ZnS and an advanced interpretation of their excitation levels *Journal of Physics C: Solid State Physics* 1988 vol. **21** p. 5615-30
- 61 Goetz G. and et al., Optical properties of vanadium ions in ZnSe *Journal of Physics: Condensed Matter* 1992 vol. **4** p. 8253
- 62 Meyn J. P., Danger T., Petermann K. and Huber G., Spectroscopic characterization of V^{4+} -doped Al_2O_3 and YAlO_3 *Journal of Luminescence* 1993 vol. **55** p. 55-62
- 63 Mamiya H. and Onoda M., Electronic states of vanadium spinels MgV_2O_4 and ZnV_2O_4 *Solid State Communications* 1995 vol. **95** p. 217-21
- 64 Kim Y.-G. and Lee C., Optical absorption of vanadium doped ZnGa_2Se_4 single crystals *Journal of Applied Physics* 1998 vol. **83** p. 8068-70
- 65 Kück S. and Jander P., Luminescence from V^{3+} in tetrahedral oxo-coordination *Chemical Physics Letters* 1999 vol. **300** p. 189-94
- 66 Ryba-Romanowski W., Golab S., Dominiak-Dzik G. and Berkowski M., Optical spectra of a LaGaO_3 crystal singly doped with chromium, vanadium and cobalt *Journal of Alloys and Compounds* 1999 vol. **288** p. 262-8
- 67 Motome Y. and Tsunetsugu H., Orbital ordering and one-dimensional magnetic correlation in vanadium spinel oxides *Physica B: Condensed Matter* 2005 vol. **359-361** p. 1222-4

- 68 Hughes M., Rutt H., Hewak D. and Curry R. J., Spectroscopy of vanadium (III) doped gallium lanthanum sulphide chalcogenide glass *Applied Physics Letters* 2007 vol. **90** p. 031108-3
- 69 Fujimoto Y., Tanno H., Izumi K., Yoshida S., Miyazaki S., Shirai M., Tanaka K., Kawabe Y. and Hanamura E., Vanadium-doped MgAl_2O_4 crystals as white light source *Journal of Luminescence* 2008 vol. **128** p. 282-6
- 70 Hughes M. A., Curry R. J. and Hewak D. W., Determination of the oxidation state and coordination of a vanadium doped chalcogenide glass *Optical Materials* 2011 vol. **33** p. 315-22
- 71 Tsukerblat B. S., *Group theory in chemistry and spectroscopy: a simple guide to advanced usage* (London: Academic Press Limited) 1994
- 72 Bersuker I. B., *Electronic structure and properties of transition metal compounds* (New Jersey John Wiley & Sons) 2010
- 73 Kittel C., *Introduction to Solid State Physics* (Berkeley: University of California) 2004
- 74 Tanabe S. and Sugano S., On the absorption spectra of complex ions *Journal of the Physical Society of Japan* 1954 vol. **9** p. 766
- 75 Sugano S., Tanabe Y. and Kamimura H., *Multiplets of Transition Metal Ions in Crystals*. (New York: Academic Press) 1970
- 76 Liehr A. D., The free electron (or hole) cubic ligand field spectrum *The Journal of Physical Chemistry* 1963 vol. **67** p. 1314-28
- 77 Henderson B. and Imbusch G. F., *Optical Spectroscopy of Inorganic Solids* (Oxford: Clarendon Press) 1989
- 78 Schäfer H., *Chemical transport reactions* (London: Academic Press Inc) 1964
- 79 Mandel G., Vapor transport of solids by vapor phase reactions *Journal of Physics and Chemistry of Solids* 1962 vol. **23** p. 587-98
- 80 Berthold H. J. and Köhler K., Preparative und röntgenographische Untersuchungen über das System $\text{Al}_2\text{S}_3\text{-ZnS}$ *Zeitschrift für anorganische und allgemeine Chemie* 1981 vol. **475** p. 45-55
- 81 Steigmann G., The crystal structures of ZnAl_2S_4 *Acta Crystallographica* 1967 vol. **23** p. 142-7
- 82 Garcia-Sole J., Bausa L. E. and Jaque D., *An Introduction to the Optical Spectroscopy of Inorganic Solids* (Chichester, England: John Wiley & Sons Ltd) 2005
- 83 Kulikova O. V., Moldovyan N. A., Popov S. M., Radautsan S. I. and Siminel A. V., Optical Absorption and Raman Scattering of Spinel Type Semiconductor ZnAl_2S_4 *Japanese Journal of Applied Physics* 1993 vol. **Supplement 32-3** p. 586-7

- 84 Anghel S., Absorbption spectra of cobalt doped α -ZnAl₂S₄ spinel type single crystals *Journal of Optoelectronics and Advanced Materials* 2011 vol. p.
- 85 Sardar D. K., Gruber J. B., Zandi B., Ferry M. and Kokta M. R., Spectroscopic properties of Co²⁺ in related spinels *Journal of Applied Physics* 2002 vol. **91** p. 4846-52
- 86 Anghel S., Boulon G., Kulyuk L. and Sushkevich K., Luminescent properties of cobalt-doped α -ZnAl₂S₄ spinel type single crystals *Journal of Luminescence* 2011 vol. **131** p. 2483-6
- 87 Anghel S., Boulon G., Kulyuk L. and Sushkevich K., Radiative properties of α -ZnAl₂S₄:V spinel type single crystals *Physica B: Condensed Matter* 2011 vol. p.
- 88 Shannon R. D., Revised effective ionic radii and systematic studies of interatomic distances in halides and chalcogenides *Acta Crystallographica Section A* 1976 vol. **32** p. 751-67
- 89 Tomita A., Sato T., Tanaka K., Kawabe Y., Shirai M., Tanaka K. and Hanamura E., Luminescence channels of manganese-doped spinel *Journal of Luminescence* 2004 vol. **109** p. 19-24
- 90 Mikenda W. and Preisinger A., N-lines in the luminescence spectra of Cr³⁺ -doped spinels (II) origins of N-lines *Journal of Luminescence* 1981 vol. **26** p. 67-83
- 91 Yamaga M., Henderson B. and O'Donnell K. P., Tunnelling between excited ⁴T₂ and ²E states of Cr³⁺ ions with small energy separation-the case of GSGG *Journal of Physics: Condensed Matter* 1989 vol. **1** p. 9175-82
- 92 Yamaga M., Henderson B., O'Donnell K. P., Cowan C. T. and Marshall A., Temperature dependence of the lifetime of Cr³⁺ luminescence in garnet crystals I *Applied Physics B: Lasers and Optics* 1990 vol. **50** p. 425-31
- 93 Henderson B., Marshall A., Yamaga M., Henderson B., O'Donnell K. P. and Cockayne B., The temperature dependence of Cr³⁺ photoluminescence in some garnet crystals *Journal of Physics C: Solid State Physics* 1988 vol. **21** p. 6187
- 94 Kai T., Kaifuku M., Aksenov I. and Sato K., Green Photoluminescence from α -Phase ZnAl₂S₄ *Japanese Journal of Applied Physics* 1995 vol. **34** p. 3073-4
- 95 Ballhausen C. J. and Gray H. B., *Molecular Orbital Theory* (London:) 1964
- 96 Anghel S., Radiative properties of Ti-doped α -ZnAl₂S₄ spinel type single crystals. In: *3rd edition of the International Conference Telecommunications, Electronics and Informatics ICTEI-2010*, (Chisinau, Moldova) (2010)

- 97 Anghel S., Boulon G., Brenier A., Fortin E., Klokishner S., Koshchug D., Kulyuk L. and Sushkevich K., Spectroscopic characterization of Ti-doped α -ZnAl₂S₄ spinel-type single crystals *Journal of Physics: Condensed Matter* 2010 vol. **22** p. 055903 -9
- 98 Slater J. C., One-Electron Energies of Atoms, Molecules, and Solids *Physical Review* 1955 vol. **98** p. 1039

PUBLICATIONS DURING THE PhD

- 1 **Anghel S.**, Boulon G, Brenier A, Fortin E, Klokishner S, Koshchug D, Kulyuk L and Sushkevich K Spectroscopic characterization of Ti-doped α -ZnAl₂S₄ spinel-type single crystals *Journal of Physics: Condensed Matter* 2010 vol. **22** p. 055903 -9
- 2 **Anghel S.**, Boulon G., Kulyuk L. and Sushkevich K., Luminescent properties of cobalt-doped α -ZnAl₂S₄ spinel type single crystals *Journal of Luminescence* 2011 vol. **131** p. 2483-6
- 3 **Anghel S.**, Boulon G., Kulyuk L. and Sushkevich K., Radiative properties of α -ZnAl₂S₄:V spinel type single crystals *Physica B: Condensed Matter* 2011 vol. **406** p. 4600-3
- 4 **Anghel S.**, Absorbtion spectra of cobalt doped α -ZnAl₂S₄ spinel type single crystals *Journal of Optoelectronics and Advanced Materials - Rapid Communications* 2011 vol. **5** p. 1081-3
- 5 Zhao W., **Anghel S.**, Mancini C., Amans D., Boulon G., Epicier T., Shi Y., Feng X. Q., Pan Y. B., Chani V. and Yoshikawa A., Ce³⁺ dopant segregation in Y₃Al₅O₁₂ optical ceramics *Optical Materials* 2011 vol. **33** p. 684-7

CONFERENCE PARTICIPATIONS DURING THE PhD

- 1 **Anghel S.**, Boulon G, Kulyuk L and Sushkevich K 2011 IR Luminescence of Cobalt and Vanadium doped α -ZnAl₂S₄ spinel type crystals In: *The Int. Conf. on Luminescence & Optical Spectroscopy of Condensed Matter 2011*, (Ann-Arbor, USA)
- 2 **Anghel S.**, Boulon G, Kulyuk L, Klokishner S and Sushkevich K 2010 Luminescence Co-doped α -ZnAl₂S₄ spinel type single crystals. In: *XIV International Feofilov Symposium on spectroscopy of crystals doped with rare earth and transition metal ions*, (St.-Petersburg) p 29
- 3 **Anghel S.**, Boulon G, Kulyuk L and Sushkevich K 2010 Luminescence V-doped α -ZnAl₂S₄ spinel type single crystals. In: *Excited states of transition elements and Workshop on luminescence*, (Wroclaw, Poland) pp P-2
- 4 **Anghel S.**, Boulon G, Brenier A, Klokishner S, Kulyuk L and Sushkevich K 2009 Luminescence of Ti-doped α -ZnAl₂S₄ spinel type single crystals. In: *7th International Conference on Luminescent Detectors and Transformers of Ionizing Radiation*, (Kraków, Poland)
- 5 Kulyuk L, Sushkevich K, **Anghel S.**, Koshchug D, Boulon G and Brenier A 2008 Photoluminescence of Ti-ions in α -ZnAl₂S₄:Ti single crystals In: *The 5th conference on condensed matter physics*, (Timisoara, Romania) p 52

- 6 **Anghel S**, Boulon G, Kulyuk L, Klokishner S and Sushkevich K 2010 Radiative properties of Co and V-doped α -ZnAl₂S₄ spinel type single crystals. In: *7th European-Israeli Workshop on "Materials for and by Optics"*, (Lyon, France:) p 99
- 7 **Anghel S** 2010 Radiative properties of Co²⁺ in tetrahedral coordination in α -ZnAl₂S₄ spinel type single crystals In: *5th International Conference on Materials Science and Condensed Matter Physics*, (Chisinau, Moldova)
- 8 Boulon G, Zhao W, **Anghel S**, Mancini C, Amans D, Epicier T, Chani V and Yoshikawa A 2010 Rare earth dopant degradation in optical ceramics. In: *XIV International Feofilov Symposium on spectroscopy of crystals doped with rare earth and transition metal ions*, (St.-Petersburg) p 43
- 9 Boulon G, Zhao W, **Anghel S**, Mancini C, Amans D, Chani V and Yoshikawa A 2010 Segregation phenomenon of rare earth dopants in ceramics. In: *6th Laser ceramics symposium: International symposium on transparent ceramics for photonic applications* (Munster, Germany) p 12
- 10 Boulon G, Zhao W, **Anghel S**, Mancini C, Amans D, Epicier T, Chani V and Yoshikawa A 2010 Segregation phenomenon of rare earth dopants in transparent oxide optical ceramic. In: *Excited states of transition elements and Workshop on luminescence*, (Wroclaw, Poland) pp Mo-9
- 11 **Anghel S**, Boulon G, Klokishner S, Kulyuk L and Sushkevich K 2010 Site selective spectroscopy of the spinel type α -ZnAl₂S₄ crystals doped with transition metals: Co, V, Ti and Cr. In: *5th International Conference on Materials Science and Condensed Matter Physics*, (Chisinau, Moldova)

CURRICULUM VITAE

PERSONAL DETAILS

Surname	Anghel	
Name	Sergiu	
Date of birth	12 July 1983	
Place of birth	MDA Orhei, Republic of Moldova	
Affiliation and official address:	Institute of Applied Physics of Academy of Sciences of Moldova, Academiei str. 5, Chisinau MD – 2028, Republic of Moldova	
Contact information	mobile : +373 69062637 e-mail : anggell@gmail.com	
Nationality	Moldavian	
Marital status	Married	

EDUCATION

2007 – 2010	Simultaneous PhD student of Institute of Applied Physics of the Academy of Sciences of Moldova, Republic of Moldova and Laboratoire de Physico - Chimie des Matériaux Luminescents, Université Claude Bernard Lyon1, France
2006 – 2007	Master degree at Moldova State University, Department of Physics, Specialization – “ <i>Solid state physics</i> ”, Republic of Moldova
2002 – 2006	Student at Moldova State University, Department of Physics, Specialization - “ <i>Spectroscopy and Physical Methods of Analysis</i> ”, Republic of Moldova

PhD defence of the thesis “**Optical processes in α -ZnAl₂S₄ spinel-type single crystals doped by transition metals ions Ti, Co and V**”– 11/11/2011

WORK EXPERIENCE

- 2004 – 2006 Laboratory assistant at Chair of "Meteorology, Metrology and Experimental Physics", Department of Physics, Moldova State University, A. Mateevici str. 60,
MD - 2009, Chisinau, Republic of Moldova
- 2006 – 2007 Assistant Lecturer at Chair of "Meteorology, Metrology and Experimental Physics", Department of Physics, Moldova State University, A. Mateevici str. 60,
MD - 2009, Chisinau, Republic of Moldova
- 2007 – 2010 Partial-time engaged scientific worker of the Institute of Applied Physics of the Academy of Sciences of Moldova, Academiei str. 5, Chisinau MD – 2028, Republic of Moldova
- 2010 - present Scientific researcher of the Institute of Applied Physics of the Academy of Sciences of Moldova, Academiei str. 5, Chisinau MD – 2028, Republic of Moldova

CURRENT SCIENTIFIC INTERESTS

- Time-resolved luminescence and optical spectroscopy of condensed matter with using UV and Visible radiation
- Synthesis and characterization of new luminescence materials doped with transition metals and rare earth ions.
- Investigation of the dynamics and spectroscopy of processes responsible for radiative relaxation of excited impurity centres, crystal structure defects in wide band gap crystals and optical ceramics.

ACADEMIC PUBLICATIONS AND CONFERENCE PARTICIPATION

Please see list enclosed.

COMPUTING AND ANALYSIS

- Analysis of experimental data (emission, absorption and transmission, excitation, time-resolved luminescence spectra; lifetime decay curves, and X-ray patterns) with using special scientific software
- Numerical analysis with MathCAD
- Programming in Borland C++, Assembler, HTML
- MS Office (Word, Excel, PowerPoint, Outlook) + Adobe Acrobat/Reader

MISCELLANEOUS

Languages:

English (good), French (fluent), Russian (fluent), Romanian (mother tongue)

Hobbies:

Sport, playing football, music, films, technologies, swimming, trips.

HONORS/AWARDS

- 2005, April 20 – 27 Diploma of 2nd degree for active participation and able presentation of the speech as part of Students Scientific Conference, the 10th edition, dedicated to the day of Moldova State University, Chisinau; Republic of Moldova
- 2006, April 17 – 20 Diploma of 1st degree for active participation and able presentation of the speech as part of Students Scientific Conference, the 11th edition, dedicated to the Day of *Moldova State University*, Chisinau, Republic of Moldova
- 2009 -2010 Laureate of the Youth Prize in „Physics and Engineering of Semiconductors” of the Government of the Republic of Moldova
- 2010-2011 Laureate of the World Federation of Scientists (WFS) national scholarship

REFERENCES

Professor Leonid Culiuc

Institute of Applied Physics
Academy of Sciences of Moldova
Academiei str. 5, Chisinau
MD-2028, Republic of Moldova
Tel: + (373 22) 73 10 55
Fax: + (373 22) 73 81 49
e-mail: kulyuk@phys.asm.md

Professor Georges Boulon

Physico Chimie des Matériaux Luminescents
Université Claude Bernard Lyon1
UMR 5620 CNRS,
Bât A. Kastler, 10 rue Ada Byron, La Doua 69622
Villeurbanne cedex France
Tel: + (33) 4 72 44 82 71
Fax: + (33) 4 72 43 11 30
E-mail: georges.boulon@univ-lyon1.fr